EFFECT OF ELECTROSPINING VARIABLES ON FIBER DIAMETER AND MEASURED ELECTRIC CURRENT

L'EFFET DES PARAMETRES D'ELECTROFILAGE SUR LE DIAMETRE DE LA FIBRE ET LE COURANT ELECTRIQUE MESURE

A Thesis Submitted to the Division of Graduate Studies
of the Royal Military College of Canada
by
Siavash Sarabi Mianeji

Supervised by:
Dr. Danny Pagé
Dr. Jennifer Scott

In Partial Fulfillment of the Requirements for the Degree of
Master of Applied Science

April, 2015

Scientific contributions resulting from this thesis

a. Scholarly journal

S.S. Maneji, D.J.Y.S. Pagé, J.L. Scott, *Impact of electrospinning process parameters on the measured current and fiber diameter*, Submitted as a manuscript to *Polymer Science and Engineering*, accepted 6 January 2015.

b. Conference proceedings

S.S. Maneji, J.L. Scott, D.J.Y.S. Pagé, *Process optimization for the electrospinning of poly caprolactone nanofibers using non-halogenated solvents*, Proceedings of the New Trends in Transport Phenomena (NTTP14), Ottawa, Ontario, Canada, May 1-2 2014, Paper No. 82 (30/93 papers were published in the proceedings)

c. Presentations at conferences

S.S. Maneji, D.J.Y.S. Pagé, J.L. Scott, *Electrospinning of cellulose propionate reinforced poly caprolactone fibers*, 64th Annual Canadian Society for Chemical Engineering Conference, (20-22 Oct. 2014), Niagara Falls, ON.

S.S. Maneji, D.J.Y.S. Pagé, J.L. Scott, *Solvent and Process Parameters Selection for the Electrospinning of Polycaprolactone*, 63rd Annual Canadian Society for Chemical Engineering Conference, (23-26 Oct. 2013), Fredericton, NB.

Acknowledgment

Hereby, I would like to express my sincere gratitude to the people who supported me to complete this project successfully.

First I would like to express my deep thankfulness to my advisors Dr. Danny Pagé and Dr. Jennifer Scott for their tremendous support. I would also like to thank them for encouraging and guiding me throughout the project. I would specially like to thank Dr. Jennifer Snelgrove who helped me to provide SEM images which were fundamental for my project. I extend my sincere thanks to Mr. Kommy Farahani and Dr. Neda Bavarian for their technical support. I also want to thank Mr. Clarence McEwen and Mr. Brent Ball for their help to set up the electrospinning device.

TABLE OF CONTENTS

List of Figures

List of Tables

Abbreviations

ANOVA: Analysis of variance

Alpha (α): Significance Level

CAB: Cellulose acetate butyrate

CP: Cellulose propionate

CP-PCL: Cellulose propionate- Poly caprolactone

DS: Degree of substitution

DSC: Differential scanning calorimetry

DIOX: 1,4-Dioxane

DMA: Dynamic mechanical analysis

DMF: Dimethylformamide

EA: Ethyl acetate

ECs: Endothelial Cells

FT-IR: Fourier transform infrared

MeOH: Methanol

NEM: Native Extracellular Matrix

NMR: Nuclear magnetic resonance

PCL: Poly caprolactone

PDLA: Poly (D-L-Lactic acid)

PEO: poly (ethyleneoxide)

PLGA: Poly Lactic-co-Glycolic Acid

P (LLA-CL): Poly (L-lactide-co-ε-caprolactone)

PLLA: Poly (L-lactic acid)

P-Value: Statistical significance

rpm: Rotations per minute

SEM: Scanning electron microscope

TCD: Tip to collector distance

TEAB: Tetraethylammonium bromide

THF: Tetrahydrofuran

V_f: Volume fraction

χ: Local aspect ratio

Abstract

Electrospinning is a technique used to produce continuous nanofibers with diameters in the range of nm-µm. Electrospun nanofibers are potential candidates for applications such as tissue engineering, filters, wound dressings, composite reinforcement, and drug delivery materials, among others. In this study, electrospinning is used to fabricate biodegradable nanocomposite fibers using poly caprolactone (PCL) and cellulose propionate (CP) as a reinforcing agent. Non-halogenated co-solvents have been selected using solubility graphs based on the fractional cohesion parameter of solvents. A single variable optimization method has been used for the optimization of different electrospinning process parameters including solvent ratio, polymer concentration, applied voltage, flow rate and tip to collector distance. Scanning electron microscopy was used to characterize the nanofibers' morphology and diameter, and the resulting diameters were plotted against each process variable in order to determine optimal processing conditions for the production of uniform fibers with the narrowest fiber distribution. The measured diameter of the spun fibers for the studied process variables was modeled using the terminal jet theory. Electric current was measured during electrospinning and the results revealed valuable information about the mechanism at play during the process. Jet motions such as whipping or splitting are shown to directly impact fiber diameter and the measured electric current. The thermal properties and crystallinity of the resulting nanofibers were evaluated using differential scanning calorimetry which showed an increase in crystallinity of the nanofibers when compared to the bulk polymer. Finally, tensile strength and elongation of the resulting nanofibers were studied using dynamic mechanical analysis which revealed an increase of tensile strength for CP-PCL blends.

Résumé

L’électrofilage est une technique utilisée pour produire des nanofibres continues avec des diamètres de l'ordre de nm-µm. Les nanofibres électrofilées sont des candidates potentielles pour des applications telles que le génie tissulaire, les filtres, pansements pour plaies, le renfort composite, et des matériaux de délivrance de médicaments, entre autres. Dans cette étude, l’électrofilage est utilisé pour fabriquer des fibres de nanocomposites biodégradables de poly-caprolactone (PCL) en utilisant le propionate de cellulose (CP) comme agent de renforcement. Des co-solvants non halogénés ont été sélectionnés en utilisant des graphiques de solubilité en fonction du paramètre de cohésion fractionnaire des solvants. Un procédé d'optimisation à variable unique a été utilisé pour l'optimisation des différents paramètres du procédé d'électrofilage. Les paramètres étudiés inclus le taux de solvant, la concentration en polymère, le voltage appliqué, le débit de la solution et la distance de la pointe au collecteur. La microscopie électronique à balayage a été utilisée afin de caractériser la morphologie et le diamètre des nanofibres. Les diamètres obtenus ont été tracé en fonction de chaque variable du procédé afin de déterminer les conditions de traitement optimales pour la production des plus petites fibres possible et le plus uniforme possible. Le diamètre mesuré des fibres filées a été modélisé, en fonction des paramètres de mise en œuvre, en utilisant la théorie du jet terminal. Le courant électrique a été mesuré au cours de l'électrofilage et les résultats ont révélés de précieuses informations sur le mécanisme en jeu lors de l'électrofilage. Les mouvements du jet tels que la flagellation ou le fractionnement ont un impact direct sur le diamètre des fibres et le courant électrique mesurés. Les propriétés thermiques et la cristallinité des nanofibres résultantes ont été évaluées en utilisant la calorimétrie différentielle à balayage qui montre une augmentation de la cristallinité des nanofibres par rapport au polymère en vrac. Enfin, la résistance à la traction et l'allongement des nanofibres résultantes ont été étudiés en utilisant une analyse mécanique dynamique qui a révélé une augmentation considérable de la résistance à la traction pour les mélanges de CP-PCL.

Chapter 1: Introduction

The emergence of nanomaterials over the last few decades has provided enormous potential for the production of increasingly lighter, stronger and smaller system components for high-tech applications. Nanomaterials come in various shapes and compositions and are characterized by a high surface area, often possessing distinctive properties from their macro scale counterparts. Polymeric nanofibers with diameters in the nanoscale support numerous applications, such as scaffolds for tissue engineering, sensoring devices and high strength structures for use in infrastructure or transport platforms [1, 2].

Industrial and technological developments have increased demand for the use of synthetic non-degradable polymers [3] resulting in their presence in up to 25% of municipal solid waste [4]. These materials often become environmental pollutants at the end of their life cycle and can pose a risk to flora, animal life and human health. These latter concerns have caused an increased interest for the use of biodegradable polymers as an alternative to conventional non-degradable polymers for many applications. In particular, the ability to produce nanofibers of poly caprolactone (PCL) is of great interest due to its biodegradability and long standing use in biomedical applications.

Mechanical conventional spinning methods are unable to produce fibers with diameters less than two microns [5]. Polymer nanofibers can be processed by drawing nanofibers [6], template synthesis [7], and electrospinning. Drawing produces single nanofibers using a sharp tip to draw the polymer solution from its deposited droplet. Drawn polymer solidifies due to the fast evaporation of the solvent. Template synthesis is another technique which uses a nanoporous membrane as a template to produce nanoscale fibers. This technique can produce nanoscale fibers from different materials such as conductive materials, metals, and semi-conductive materials.

During the last few decades, electrospinning has attracted the interest of many researchers due to its ability to produce fibers in the nanoscale range with high surface areas. In the electrospinning process, a conductive polymer solution is held by its surface tension at the tip of a capillary tube and introduced to an electric field. Repulsion of the induced charges stretches the polymer solution as it is kept together by surface tension. By increasing the electric field, a conical shape of solution is formed at the tip of the needle, called a Taylor cone [8]. At a critical electric field, the repulsive force overcomes the surface tension and a jet of polymer solution is released from the surface of the Taylor cone. While the charged jet moves toward the collector, the solvent evaporates and the charged polymer is discharged on the surface of the metallic collector and creates a non-woven continuous fiber.

Different variables are involved in producing uniform nanofibers with smaller diameters. These variables can be divided in two separate categories, polymer solution parameters and electrospinning variables.

Solution parameters include the solvent ratio for binary solvents and the concentration of polymer in the solution. The selection of solvent is an important step in the production of nanofibers. Particularly, solvation power and conductivity of solvents are important parameters in the selection of solvents in order to achieve successful electrospinning. In this study, Teas graphs are used as a tool for selecting the appropriate solvent combination and are explained in depth in the later section. In addition, consideration of solvent toxicity can be another factor in the selection of solvents towards decreasing environmental pollution. In this study, the selection of green solvents (low toxicity) has been achieved based on the classification of the American Chemical Society (ACS) for solvents and their toxicity [9]. After the selection of solvents, optimization of the solvent ratio within the binary solvent and the concentration of polymer in the solution are critical steps and explained in this study.

Optimization of electrospinning variables is another important factor to decrease the nanofiber diameter with increased uniformity. These variables include the applied voltage, the flow rate of the polymer solution and the tip to collector distance. In this study, optimization processes and the mechanism of their effect on fiber diameter is discussed in detail.

1.1. Objectives

The main goal of the project was to optimize the electrospinning process in order to provide uniform PCL nanofibers and CP-PCL composite nanofibers with smaller diameters and narrower diameter distributions. The targeted materials can be used for medical and structural applications. The materials were characterized for nanofiber diameter and their physical properties and the optimized process was modeled using terminal jet theory. The sub-objectives are explained in the following sections.

1.1.1. Sustainable solvent and material choice

Poly caprolactone and the cellulosic propionate used in the electrospinning process are both biodegradable. The first sub-objective was to make sustainable processing choices by selecting solvents that are more environmentally-friendly than the common halogenated alternatives, yet are just as effective for the electrospinning of PCL.

1.1.2. Process optimization

The electrospinning parameters were optimized in order to produce uniform nanofibers with narrow fiber distributions. These parameters include polymer concentration, applied voltage, solution flow rate and tip to collector distance. Pure poly caprolactone and poly caprolactone reinforced with cellulose propionate were processed.

1.1.3. Characterization of electrospun nanofibers

In order to evaluate the effect of electrospinning on the physical properties of the final product, the morphology, thermal and mechanical properties of electrospun nanofibers were characterized.

1.1.4. Process modeling

In order to compare the diameter of the resultant fiber with the theoretical diameter, the diameter of the processed fibers was modeled as a function of the processing parameters using the terminal jet theory [10]. In order to model the process, electric current was measured during the optimization process and the resultant data revealed valuable information about the mechanism of electrospinning as a function of different variables such as polymer concentration, applied voltage, flow rate and tip to collector distance.

Chapter 2: Literature Review

2.1. Polymeric nanofibers and their applications

In the development of nanoscience in the last few decades, polymeric nanofibers, such as those produced by electrospinning, have become an attractive product for different applications because of their high surface area, continuous fiber morphology and the functionality of the polymer surface.
Nanofibers can be manufactured using both sustainable and biodegradable polymers for different applications. In general, biodegradable polymers are appropriate for biomedical applications, while long-lasting polymers are desired for their higher thermal and mechanical properties and are suitable for industrial applications such as composite reinforcement [11] and filtration [12,13]. However, in the interest of reducing our environmental footprint, there is a desire to replace long-lasting polymers with biodegradable alternatives. Biodegradable polymers can be produced from both natural sources (agro-polymers like cellulosic polymers) and synthetic polymers, such as PCL as a bio-polyester [14].
In the following section, some examples of applications for biodegradable nanofibers are highlighted.

2.1.1. Composite reinforcement

Fibers with diameters in the sub-micron range often display better mechanical properties than the bulk materials. Materials scientists anticipate that using nanoscale fibers as a reinforcement in composite scaffolds may enhance their mechanical properties [15]. Studies show that the reinforcement is dependent on the orientation of the fibers. The reinforcement for aligned fibers is higher than that of random nanofibers [16, 17]. For example, Saghafi *et al.* used PCL nanofibers for toughening of epoxy-based laminates. Results show that inserting a layer of PCL nanofibers between layers of laminates could decrease the area of damage, under the impacted load of 24 J, by up to 26% [18]. Zoppe and his colleagues used cellulose nanocrystals to reinforce poly (ε-caprolactone). They found that the mechanical properties of PCL nanofibers were significantly improved after reinforcement [19]. In addition, one of the potential applications for nanocomposites is to replace the metals in car manufacturing [20]. Using nanocomposites will reduce the weight of the automobile, give better fuel efficiency and decrease exhaust gas emissions generated from the combustion process in the engine, thereby rendering the life cycle of materials in automobiles more sustainable for the environment.

2.1.2. Tissue engineering

Tissue engineering involves the use of electrospun fibers as a scaffold to allow the growth of native extracellular matrix (NEM) in three dimensions. Figure 1 provides a schematic representation of tissue engineering principles. Fiber diameter and the amount of pores in the material are important parameters in tissue engineering. In addition, the biodegradability of the polymer is important because its degradation rate should match the neo-tissue formation and should not be toxic to the body during the process. As an example, it was found that endothelial cells (ECs) tend to have faster growth on poly L-lactide-co-caprolactone or P (LLA-CL) cast films in comparison to fibers [21]. However, because fiber scaffolds provide better support, a combination of nanofiber scaffolds and cast films of P (LLA-CL) have been used in culturing vascular muscle cells [21]. The effect of fiber diameter on ECs growth has been studied on poly lactic acid [22] and poly caprolactone [23] and results revealed that ECs tend to grow on larger fiber diameters.

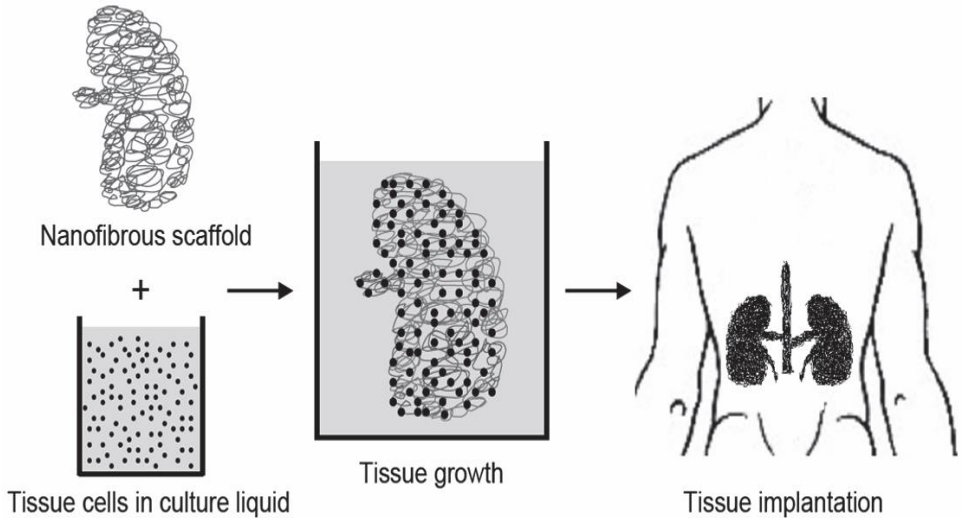

Figure 1: Tissue engineering, basic principle [24].

Many other studies report on the use of degradable nanoparticles for culturing the cells of different organs, such as P (LLA-CL) for smooth muscle cell culturing [25], Collagen-PCL as a core-sheath nanofiber for support and proliferation of skins cell [26], PCL [27] and PCL–gelatin composite nanofibers [28] for bone tissue engineering , and aligned poly lactic-co-glycolic acid nanofibers as replacements for soft and hard tissues [29].

2.1.3. Dressings for wound healing

A wound occurs as a result of any mechanical, chemical or even electrical injury which results in different levels of damage to soft tissue and skin. Thereafter, the body starts the healing process by means of releasing a variety of inflammatory mediators inside the wound. In some case, regeneration of the skin is impossible due to the depth of the injury. Applying nanofibers as the wound heals helps protect it from contamination and modifies the appearance of the wound, while providing a barrier which is permeable to moisture and oxygen. The high surface area of electrospun nanofiber mats and their unique properties also facilitate delivery of medicines and antibiotics. Schneider *et al.* used silk nanofibers with an epidermal growth factor and they revealed that the wound healing rate increased by 90% [30]. Merrell *et al.* used anticancer, antioxidant and anti-inflammatory materials with PCL as a wound healing dressing and their study showed that PCL nanofibers could deliver the drug as a sustained release agent [31]. PCL nanofibers have been used to adsorb chitosan nanoparticles to produce chitosan/PCL nanofibers as a wound dressing and healing complex. Studies showed that after applying the complex to the wound, the healing chitosan particles were released and entered into rats' primary fibroblasts [32]. One year later, Suwantong *et al.* [33] used CA (cellulose acetate) with the above-mentioned substances for wound dressing and the results of both studies showed an increase in wound closing.

2.1.4. Drug delivery

Electrospun nanofibers are suitable for drug delivery. The first step is using nanofibers as a drug carrier. As seen in Figure 2, there are three possible mechanisms for surface modification, including plasma treatment, surface grafting modification and co-electrospinning [34]. The high surface area of electrospun nanofibers provides suitable conditions for the delivery of loaded drugs. The nanofiber scaffold can be used for both the fast- and long-lasting embedded-drug release. For example, PCL/Gelatin blend nanofibers loaded with metronidazole have been used in controlled drug delivery to prevent wounds from infection and to facilitate the wound healing process [35]. In one study, PCL nanofibers loaded with vitamin B2 (riboflavin) were used as the drug delivery agent for the cross-linking of protein fibrous tissues [36]. In another study, PCL nanofibers linked to tetracycline hydrochloride (an antibiotic) have been used as a controlled drug delivery agent, showing that the PCL nanofibers could manage the transition of the drug from hydrophobic to hydrophilic media in a time-frame dependent on the concentration of tetracycline hydrochloride [37]. PLLA nanofibers have been used as a drug carrier in two forms, either as blends or co-sheath fibers. This study demonstrated that blended fibers act as a fast drug releasing agent, while co-sheath fibers play the role of long lasting drug releasing agent [38].

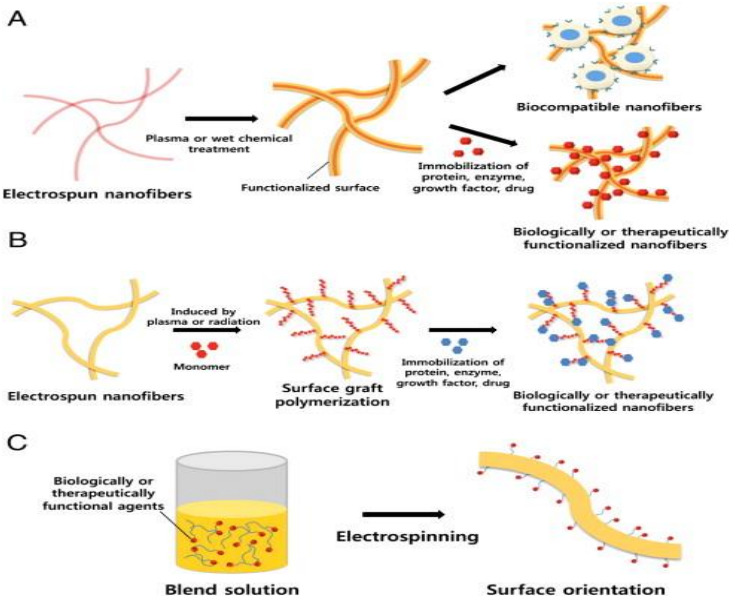

Figure 2: Schematic of electrospun fiber surface modification for drug delivery [34].

2.1.5. Other applications

Filtration is a protective process which is applied in different fields for capturing solid particles from liquid or air. The surface properties of nanofibers have resulted in a higher efficacy in comparison to conventional fiber filters. Chitosan-PCL nanofibers have been used as a filtration membrane and antibacterial agent in water filtration. Results have shown that membranes with diameters of 200-400 nm are able to remove 100% of particles in the size of 300 nm [39].

There are also other applications for nanofibers such as catalyst carriers [40, 41], sensors [42- 45] and in energy storage [46]. A complete discussion of these applications is beyond the scope of this thesis.

2.2. Origin of electrospinning

In 1914, John Zeleny reported the behaviour of conductive liquid droplets at the end of metallic tubes in the presence of electrostatic forces [6]. Later, Anton Formhals contributed to the development of electrospinning and published 22 patents between 1931 and 1941 [47]. Between 1964 and 1969, Sir Geoffrey Ingram Taylor worked on improving the theoretical aspect of electrospinning parameters, specifically in mathematically modeling the changing shape of a conductive liquid droplet (called a Taylor cone) in the presence of a high electromagnetic field.

Electrospinning is a relatively easy and cost effective technique able to produce nanofibers directly from a polymer solution. Fiber parameters such as diameter and structural morphology can be controlled by optimizing the electrospinning parameters and this will be explored in greater detail below.

2.3. Electrospinning process

A typical electrospinning set-up includes four main parts: 1) a syringe pump to control the polymer flow rate, 2) a syringe, which acts as a storage vessel for the polymer solution, and its needle, which acts both as an electrode and an extrusion die, 3) a high voltage power supply producing a potential difference between the needle and the collector, and 4) a counter electrode which acts as the collector (Figure 3).

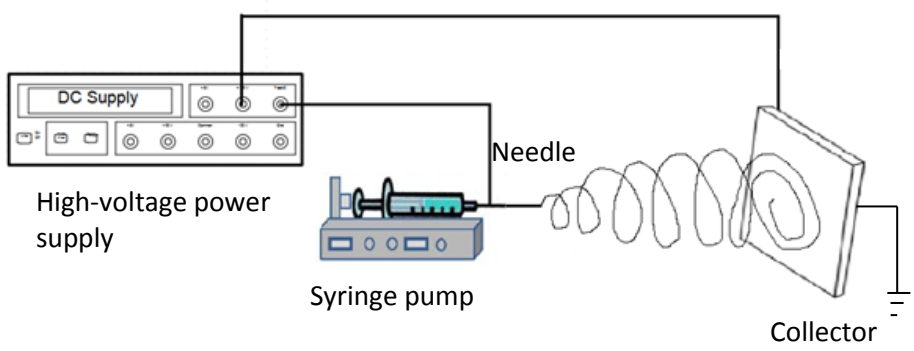

Figure 3: Schematic of electrospinning setup.

As a result of surface tension and flow, a droplet of the polymer solution is created at the tip of the needle. The features of the droplet will change under increasing potential difference to create a Taylor cone due to the repulsion between free charges in the solution. When a critical voltage is applied, depending on the electrical conductivity and surface tension of the solvent, an electrically charged polymeric jet escapes from the cone tip (Figure 4).

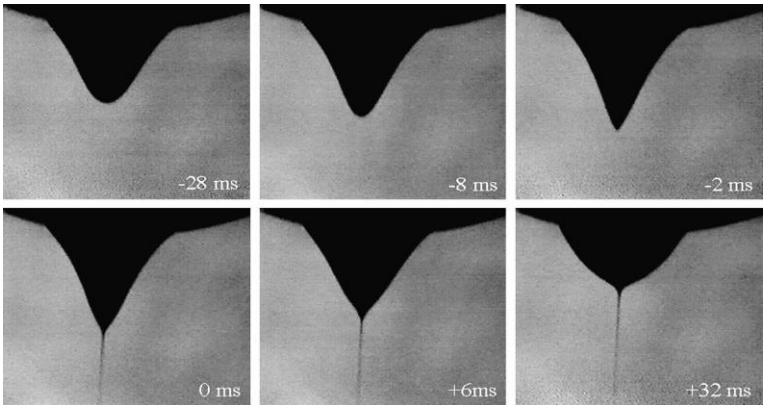

Figure 4: Steps for formation of polymer jet [48].

Initially, the created jet moves toward the collector in a straight line (a regime before the whipping motion and after the Taylor cone). In the presence of a high electric field, repulsion forces between identically-charged ions inside of the jet cause movement of the charges to the surface of the jet while the diameter of the jet decreases with increasing distance from the tip of the Taylor cone.

For a very thin jet, electrostatic repulsion forces at the surface of the jet cause perturbations. The resulting deformation splits the repulsion forces in upward and downward directions with regards to the radial direction. Overall, the jet bends and elongates (Figure 5).

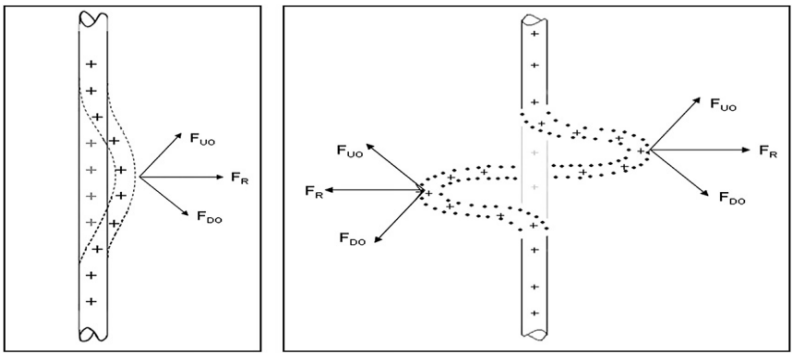

Figure 5: Effect of free charge repulsion forces on formation of whipping (F_{UO} and F_{DO} are forces in upward and downward directions respectively and F_R is resultant force) [49].

The bending of the jet can change the shape of the jet to a three dimensional coil. The dimension of the coil increases while the jet moves in circular passes toward the collector. The jet diameter decreases due to bending and elongation until the

jet becomes unstable again due to charge repulsion and creates another smaller bending deformation to satisfy the Coulombic forces. This process can be repeated several times while the smaller bends follow the trajectory of the main coil, resulting in nano-scale fibers (Figure 6) [49].

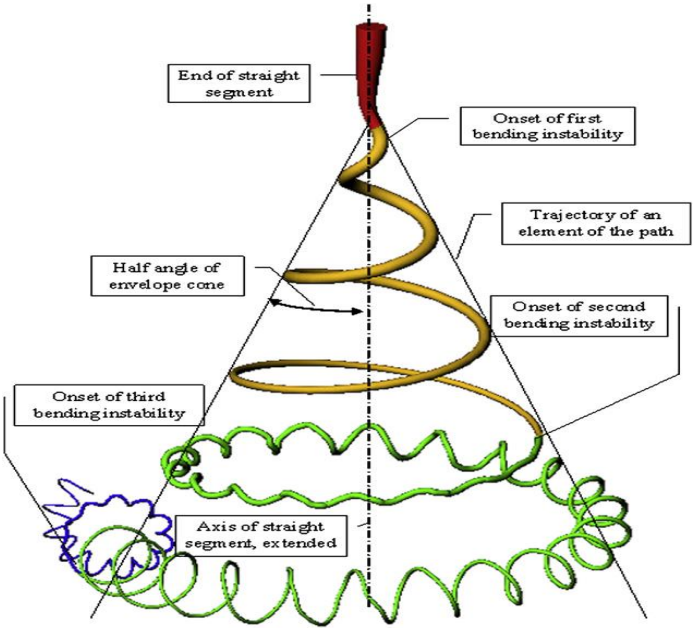

Figure 6: Process of creating bends due to charge repulsion forces [49].

2.3.1. Electrospinning parameters

The electrospinning process can be controlled by varying the process parameters. These can be separated in terms of solution, electrospinning variables and environmental conditions. Solution properties include the concentration (viscosity), surface tension and electrical conductivity of the polymer solution. Changing a single solvent parameter can affect the other solvent properties in turn making it difficult to study the isolated effect of a single variable on the nanofiber morphology. Electrospinning parameters include flow rate, electric field strength, tip to collector distance, tip design and collecting techniques. Environmental parameters are temperature, air velocity and humidity. Optimization of these variables is essential to produce uniform nanofibers by eliminating beads (a small piece of bulk polymer) on the fibers and prohibiting electrospraying (which creates charged droplets of polymeric solution in the strong electric field and results in spherical polymeric deposits). The diameter of resultant nanofibers can be controlled by manipulation of these variables.

2.3.1.1. Concentration and viscosity

The viscosity of the solution can be controlled by the concentration of the polymer. The effect of solution viscosity on the electrospun fiber has been studied in different polymer systems, such as poly L-lactic acid (PLLA) [50], poly caprolactone (PCL) [51], poly ethylene oxide (PEO) [52,55], poly D,L-lactic acid (PDLA) [53], and poly methyl methacrylate (PMMA) [54]. Research revealed that lower viscosity solutions result in increased bead formation and in some cases even electro spraying dominates over electrospinning [16, 17, 21]. By increasing the concentration, the viscosity of the solution increases and the amount of beads decreases, resulting in continuous fibers. However, when the concentration is too high, the viscosity renders electrospinning difficult [50, 55]. Furthermore, increased concentration of the solution also results in an increase in fiber diameter [52, 56]. Therefore, optimization of the solution concentration, in respect to the polymer type, is essential to produce uniform fibers with smaller diameters.

2.3.1.2. Conductivity

The conductivity of the polymer solution can be increased by adding salts [57, 58], alcohols [59], or halogenated methane like chloroform. It has been demonstrated that increasing the solution conductivity decreases the amount of beads in the final product [59]. Also, increasing the solution conductivity results in a decrease in fiber diameter [58,60]. The main reason for the above trends is the increase in charge density of the solution, which raises the mobility of the charges in the presence of an electric field. The higher mobility yields higher stretching of the solution, facilitating the production of fibers with small diameters [53].

2.3.1.3. Surface tension

The effect of surface tension on the fiber morphology has been studied [61- 63]. Surface tension is responsible for holding the solution at the end of the capillary and creates an opposing force against the applied voltage that seeks to release the polymer jet from the surface of the polymer solution. In general, studying the effect of surface tension on fiber diameter is difficult because it is combined with the other solution parameters, such as dielectric constant. However, solutions with higher surface tension can offer fibers with higher diameter.

2.3.1.4. Electric field strength

Investigations have been performed to find a relationship between the electric field strength and the morphology of the fibers [55,64]. Studies showed that by increasing the applied voltage the strength of the electric field between the tip of

the needle and the collector increases. This increase pulls charged polymer from the tip of the needle and changes the Taylor cone feature, resulting in a decreased droplet volume. By further increasing the voltage, the strength of the electric field will move the jet to the edge of the tip and the Taylor cone will not be visible (Figure 7).

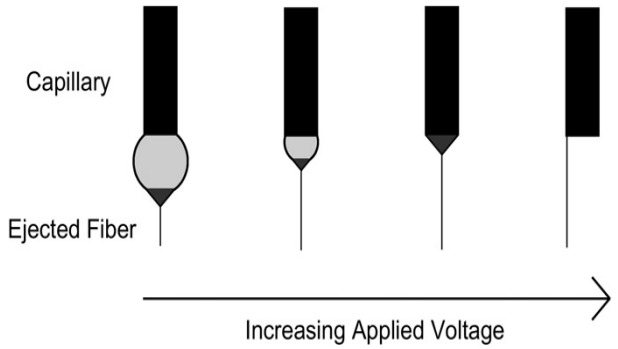

Figure 7: The effect of applied voltage on the Taylor cone formation [65].

There is an optimum voltage required in order to obtain a uniform fiber. If the voltage is lower than this optimum amount the ejection force is not enough to produce a uniform and continuous jet. As the voltage is increased, mass transfer increases and so the diameter of the resulting jet increases, producing fiber with larger diameters [55,66].

2.3.1.5. Flow rate

There is an optimum value for the flow rate in order to generate a uniform fiber. Taylor realized that sufficient flow rate is required to have a continuous fiber jet [8]. Increasing the flow rate further than the optimum value will cause the fiber diameter to increase [67]. It was attributed to the inability of the polymer to be dried and stretched before reaching the collector. In the case of a lower flow rate the uniformity of the resultant nanofiber decreases due to lack of laminar flow rate.

2.3.1.6. Tip to collector distance (TCD)

The tip to collector distance is another electrospinning parameter that can affect the diameter of the electrospun fiber. Studies involving PEO [68], polystyrene [67], poly (vinyl alcohol) (PVA) [62], gelatin [69], chitosan [70], and poly (L-lactic acid) (PLLA) [50] have concluded that an increase in the travelling distance leads to sufficient stretching of the polymeric jet and reduced diameter of the fiber. However, very long travelling distances can decrease the electric field and have an adverse effect on uniformity of fiber diameter. On the other hand, a shortened

distance results in non-uniform fibers, attributed to insufficient stretching of the polymeric jet.

2.3.1.7. Tip design

The size of the capillary tube or needle is another effective parameter to help control the fiber diameter. When a needle with a smaller inner diameter is used, the resulting fiber has a smaller diameter. This behaviour can be explained by the initial size of the droplet at the end of the tip, limiting the mass of polymer drawn from the tip and therefore the diameter [71]. In addition, different kinds of needles with various designs have been used in electrospinning processes to improve the polymer properties and features based on the desired applications. For example, Keng-Liang *et al*. designed a coaxial electrospinning set-up to produce PLLA/PEG core–shell fibrous membranes (Figure 8A) [72].

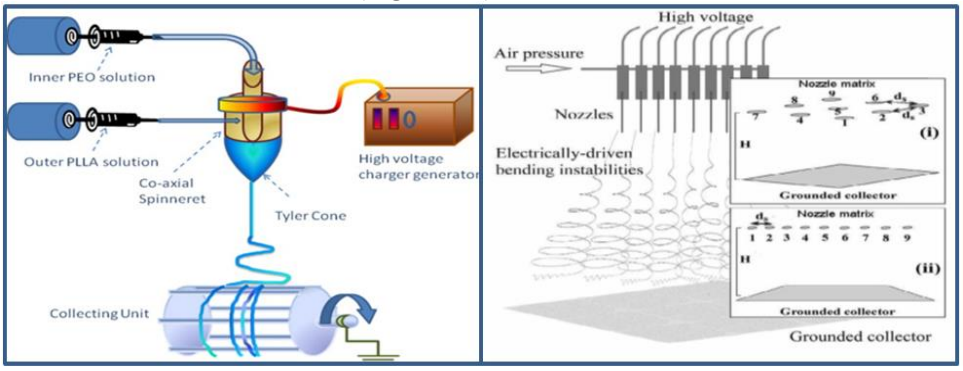

A B

Figure 8: A) Schematic of the co-axial electrospinning setup [72] ; and B) A schematic of the multiple jet injectors [73].

Multiple jet injectors have also been used to increase the production rate of electrospinning [73] as well as for the fabrication of blend polymers using different polymers in various ratios (Figure 8B) [74].

2.3.1.8. Collection techniques

Different techniques are used to produce non-woven fibers with either high alignment or random alignment. One method of producing aligned fibers is by using a rotating disc collector (Figure 9). Due to the sharp edge of the disc continuous aligned fibers will be collected.

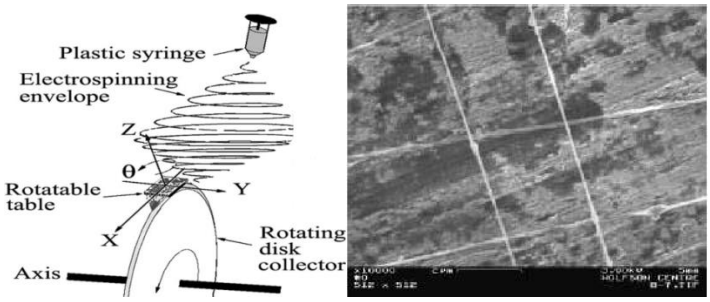

A B

Figure 9: A) Rotating disc collector; and. B) Aligned scaffold of PEO [75].

Another method for producing aligned fibers involves the use of two parallel plates (Figure 10) to control the collection of fibers between the two plates in an aligned orientation. Since there is no chance of connection between the fibers and the ground, the possibility of contamination is low. This method is ideal for producing scaffolds for tissue engineering purposes.

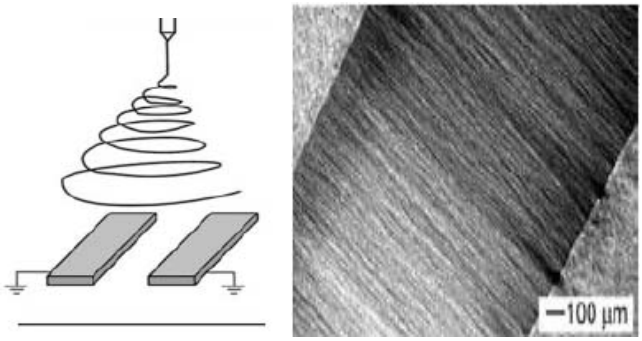

A B

Figure 10: A) Parallel grounded collector; and B) Resulting fiber image [76].

A rotating drum has also been used to produce oriented fibers (Figure 11). In this technique a grounded rotating drum is used as a collector. Variation in the rotation speed can change the morphology of the resulting fibers. Thomas and his colleagues discovered that increasing the rotation speed up to 6000 rpm can increase the alignment of fibers as well as their tensile strength [77].

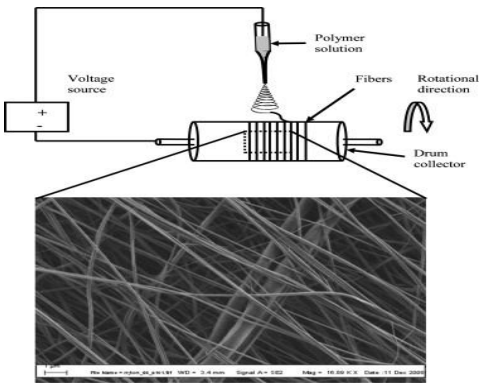

Figure 11: Schematic of rotating drum and resulting fiber [78].

There are other collecting methods to process non-woven uniform fibers with random orientation. In these methods a flat grounded surface is used as a collector. The orientation of the flat electrode can be vertical or horizontal (Figure 12).

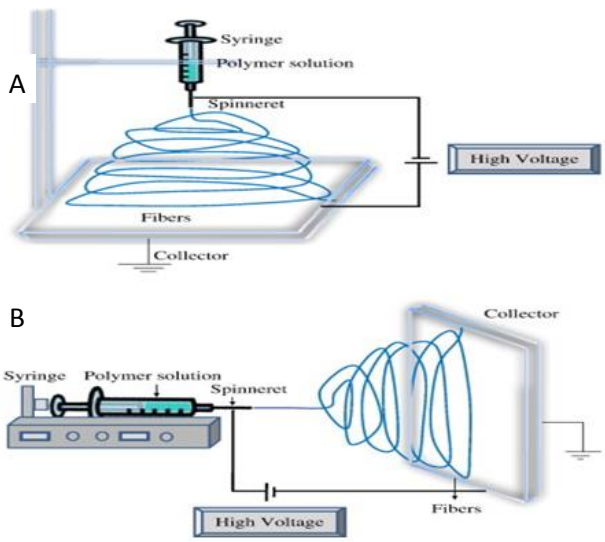

Figure 12: A) Vertical; and B) Horizontal flat collector for producing non-woven fiber [79].

2.3.1.9. Ambient parameters

Several studies have investigated the effect of ambient conditions on the morphology of nanofibers. Electrospinning of Polyamide 6 at different temperatures revealed that increases in the temperature produced fibers with

smaller diameters. This behaviour was attributed to the decrease in viscosity of the polymer at higher temperature [80]. The effect of humidity on fiber morphology has been studied by Casper and his colleagues by changing the humidity during the electrospinning of polystyrene. They realized that increasing humidity causes the appearance of circular pores [81].

The effects of electrospinning parameters on the morphology of resulting nanofibers are summarized in Table 1.

Table 1: Summary of the effect of electrospinning parameters on nanofibers' morphology.

Process parameter	**Effect on fiber morphology**
Viscosity	Low viscosity → more beads formed Increased viscosity → decreased beads, → but increased fiber diameter
Conductivity	High conductivity → uniform fibers of decreasing diameter
Surface tension	Higher surface tension → increased fiber diameter
Electric field strength	Lower applied voltage→ more bead formation Optimum voltage → uniform fiber Higher applied voltage→ increased fiber diameter
Flow rate	Higher flow rate→ increased fiber diameter Lower flow rate→ decreased fiber diameter
Tip to collector distance	An optimum distance required Long distance→decreased fiber diameter Short distance→more bead formation observed
Tip design	Smaller diameter→ fibers with smaller diameters Co-axial tip → core–shell fibers Multiple tip →increases out-put
Collector	Non-woven aligned fibers: Rotating disc collector Parallel grounded collector Rotating drum Non-woven random fibers: Horizontal and vertical flat collector
Ambient conditions	Higher temperature→decreased fiber diameter Higher humidity → appearance of circular pores

2.4. Modeling of the electrospinning process

In order to properly model the electrospinning process and predict the morphology of the resulting fibers, some researchers have tried to develop the mechanism of the electrospinning process mathematically. Yarin *et al*. studied the shape of the Taylor cone and the ejected fiber jet under a strong electric field [82]. In another study Hohman *et al.* mathematically studied the jet instability after ejection from the surface of the Taylor cone and its bending motion (called whipping motion) [83]. Using the concept of jet instability and a combination of previous studies, Fridrikh *et al*. modelled the whipping motion to predict the final jet diameter. They considered the polymeric jet as a cylindrical Newtonian fluid. The prediction of final diameter of the jet is based on the competition between the surface tension and electrostatic repulsion forces on the surface of the jet. The model implies that whipping instability is the main factor towards decreasing the jet diameter [10]. The equation for jet motion (Equation1) shows the relationship between the forces involved. This equation covers both the early, stable stage and the late, non-stable (whipping) stage:

$$\rho\pi h^2\ddot{X} = 2\pi\sigma_0 E_\infty.\hat{\xi} + (\pi\gamma + \frac{h\bar{\varepsilon}}{2}\beta(E_\infty.\hat{t})^2 + \frac{2\pi^2 h\sigma_0^2}{\bar{\varepsilon}}(3 - 2lnx))\frac{h}{R} \quad (1)$$

where, $\hat{t}$ is the tangent vector to the center line of the jet;
$\hat{\xi}$ is the vector normal to the center line (Figure 13);
h is the diameter of the jet;
R is the radius of whipping curvature;
E_∞ is the electric field;
$\sigma_0$is the surface charge density;
ε is the fluid dielectric constant;
$\bar{\varepsilon}$ is the dielectric constant of air;
γ is the surface tension of the solution;
ρ is liquid density; and
$\ddot{X}$ is second derivative of X with respect to time.

The remaining parameters are defined as $\beta = (\varepsilon/\bar{\varepsilon}$ -1) and $\chi \approx R/h$.

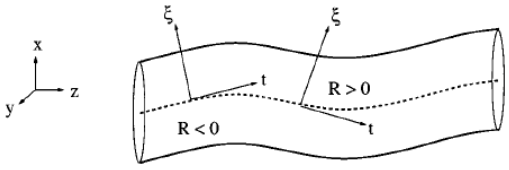

Figure 13: Vector directions from center-line in different stages of jet motion.

The first term on the right-hand side of Equation 1 shows the effect of the applied electric field on the surface free charges of the jet. The second term results from the surface tension of the polymeric jet and the third term originates from the whipping motion, which causes stretching of the jet. The last term indicates the repulsion force resulting from the jet surface charges. The first and second terms are stabilizing forces which resist against the bending of the jet while the last term is a destabilizing force. For a jet with a very small diameter, the effect of surface tension is the dominant stabilizing force and the main competition in the whipping zone is between surface charge repulsion and fluid surface tension. When surface tension and repulsion forces come to equilibrium, the fiber diameter reaches a steady state and is defined as the terminal jet diameter. Equation (2) mathematically describes the equilibrium state between the forces at play.

$$\pi\gamma \geq 2\pi^2 h(z)\sigma_0(z)^2(2lnx - 3)/\bar{\varepsilon} \qquad (2)$$

When surface tension is dominant, the jet is stable and linear, while when charge repulsion is dominant whipping occurs.

The current carried by the jet is a combination of polymer bulk conduction and surface charge advection (Equation 3) [83]:

$$I = 2\pi\sigma_0 hv + \pi EKh^2 \qquad (3)$$

where, I is the electrical current;
v is the jet velocity; and
K is the electrical conductivity.

In the region near the needle, the bulk conduction current (resulting from the polymer jet conductivity) is dominant. After thinning of the jet and migration of the free charges to the surface of the jet, the advection current is of more significance (Equation 4):

$$I = 2\pi\sigma_0\, hv \qquad (4)$$

For thin fibers, bulk conduction can be neglected and the main electric current results from surface charge convection. By considering the jet volume in the whipping zone as $Q = \pi h^2 v$ and combining this equation with Equation (4) a new equation for the electrical current is created as $I = 2\sigma_0 Q/h$. By solving this equation for σ_0 and replacing it in Equation (2), the relationship between terminal jet diameter and electrospinning variables is obtained (Equation 5):

$$h_t = (\gamma\bar{\varepsilon}\frac{Q^2.2}{I^2\pi(2lnx-3)})^{\frac{1}{3}} \qquad (5)$$

where: h_t is the fiber diameter in nm;
γ is the surface tension of the solution in g/s^2;
ε is the dielectric constant of the surrounding media;
Q is the flow rate in cm^3/s;
I is the electric current carried by the jet in $cm^{3/2} \cdot g^{1/2} \cdot s^{-2}$; and
χ = L/h; (where L is the length of the jet and h is jet diameter in the straight segment). χ has also sometimes been considered as L/d (d is a fair assumption of the nozzle diameter)[1].

Charge density on the surface of the jet is an important factor affecting the fiber morphology and diameter [84]. The main outcome of the jet charge density is the amount of electrical current carried in the whipping zone due to surface charge advection. Measurement of electrical current during electrospinning is a useful tool to predict and control the final fiber diameter. Rutledge *et al.* suggested measurement of the current during electrospinning to study the mechanism of the process [83]. Samatham *et al.* used electrical current measurements to control the efficiency of electrospinning [85]. They observed different electric current regimes: fluctuating, stable, and multiple jet regimes. The fluctuating regime represents variations in the polymer flow rate; lower flow rate could not provide laminar current of the jet toward the collector and caused some fluctuations in the carried electric current. In the stable regime, the flow rate and applied voltage are optimal, providing a continuous flow of jet toward the collector. Finally, multiple jet regimes were observed at higher voltage. They concluded that by measuring current, the uniformity of the resulting fiber is predictable. Cengiz *et al*. found that during the electrospinning of polyurethane with tetraethylammonium bromide (TEAB) the current increased with increasing concentration. They also realized that there is a strong relationship between the electric current and the spinnability of the polymer [86]. Bhattacharjee *et al*. declared that the total measured current during electrospinning includes the electric current resulting from the electrospraying of the solvent separating from the surface of the jet [87]. Fallahi *et al*. measured the electric current during the electrospinning of poly acrylonitrile at different voltages and based on this, they divided the jet motion into stable and fluctuating regimes (Figure14).

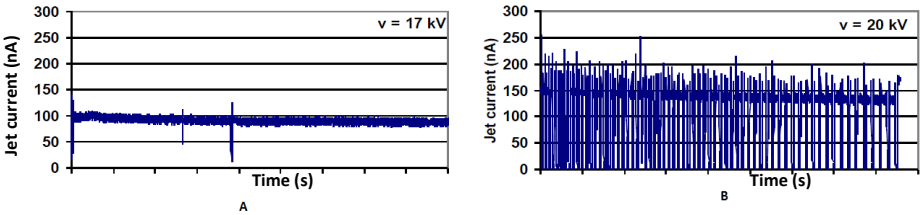

Figure 14: A) Stable regime; and B) Fluctuating regime [88].

The fluctuating regime was observed at higher voltage due to non-continuous polymer flow. At higher voltage, the speed of the jet toward the collector is higher than the feed rate, causing fluctuations of the carried electric current [88].

Chapter 3: Experimental

3.1. Materials

3.1.1. Biodegradable polymers

Capa ™ 6500 is a biodegradable polyester purchased from Perstorp and used as the poly caprolactone source (Figure 15) with an average M_W = 50000, a melting point of approximately 60 ^oC and a T_g of -60°C.

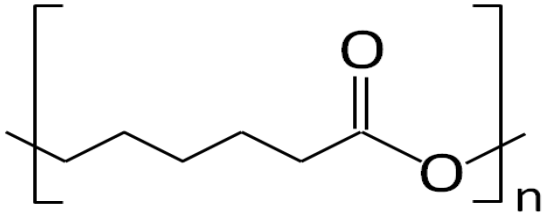

Figure 15: The chemical formula of poly caprolactone.

Cellulose propionate is a modified agro-polymer (Figure 16) with an average M_w ~130,000 and was purchased from Aldrich.

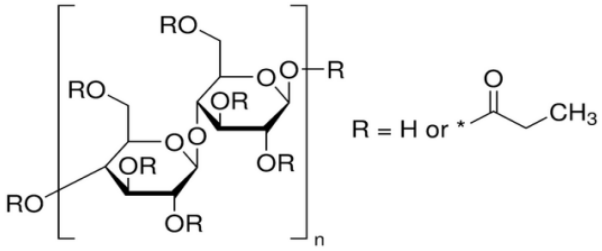

Figure 16: The chemical formula for cellulose propionate.

3.1.2. Solvents

The solvents listed in Table 2 were used to find the proper solvent system for electrospinning. All solvents were used without extra purification and safety precautions were taken based on the material safety data sheets for each solvent. Table 2 shows the suppliers and the solvent purity.

Table 2: The list of solvents and their purity, used for the solvent selection.

Solvent	**Company**
Acetone	Caledon Lab (99.5%)
$CHCl_3$	Sigma Aldrich (99.8%)
CH_2Cl_2	Fisher Scientific (99.9%)
DMF	Caledon Lab (99.8%)
MeOH	Caledon Lab (99.8%)
THF	Caledon Lab (99%)
Ethyl acetate	Caledon Lab (99.5%)
1,4 –Dioxane	Caledon Lab (99%)

3.2. Preparation of polymer solutions

PCL was dissolved in different solvent systems at various concentrations. In general, the unit of concentration was w/v %. First, the polymer was weighed according to the desired concentration and the solvents were added individually. The resulting solution was mixed using a magnetic stir bar and plate at room temperature for 24 hours and then used for electrospinning. In the case of CP/PCL blends, the mixing time was 48 hours.

3.3. Calculation of the dielectric constant for mixed solvents

The dielectric constant for mixed solvents was calculated using the formulas for polarization per unit volume, Equations (6) and (7), [89,90]. The calculation of the dielectric constant for binary solvents was obtained by first calculating the polarization of the mixed solvents using Equation 6 and then using Equation 7 in order to find the dielectric constant of the mixed solvents

$$P_m = \frac{\sum_{i=1}^{n} x_i v_i p_i}{\sum_{i=1}^{n} x_i \, v_i} \qquad (6)$$

$$P_m = \frac{(\varepsilon - 1)(2\varepsilon + 1)}{9\varepsilon} \qquad (7)$$

where, χ_i is the mole fraction;
υ_i is the molar volume;
p_i is the polarization of a pure solvent;
P_m is the polarization of mixed solvents; and
ε is the dielectric constant.

3.4. Measurement of the polymer solution properties

Viscosity and surface tension of prepared solutions were measured using a Brookfield Viscometer and a Surface Tensiometer, respectively.

3.4.1. Brookfield Viscometer

Viscosity can be defined as the fluid's resistance to deformation. The Brookfield viscometer measures viscosity by applying a torque to a rotating spindle inside of the liquid and calculating the ratio of shearing stress to the rate of shear [91]:

$$Viscosity = \frac{Shear\ stress}{Rate\ of\ shear}$$

A Brookfield Model DV-I+ viscometer with spindle 21 was used to measure the shearing viscosity. First, the spindle was connected to the instrument and the sample container filled with the polymer solution. In the next step, the spindle was immersed into the sample solution up to the filling index on the spindle, and the speed of the spindle rotation was set using a key pad. The motor was started and the amount of viscosity was read when the number was stable.

3.4.2. Tensiometer

Surface tension of polymeric solutions is an important parameter due to the fact that its competition with the charge repulsion forces during electrospinning determines the diameter of the resulting nanofibers at the collection point. Surface tension was measured using a DuNouy Tensiometer. In this method a platinum ring is submerged in the liquid and when it is raised the liquid is drawn up in a meniscus. The amount of force needed to release the ring from the liquid was measured which is correlated to surface tension.

The instrument was calibrated, based on the instrument manual, before any measurement. A 10 mL beaker was used as the sample container and the platinum

ring was immersed in the solution. After stabilizing the ring inside the solution, and while the instrument index showed zero, the ring was gradually pulled up until its separation from the surface of the solution. The amount of force needed to overcome the surface tension of the solution was measured in dyne/cm. Each solution was measured three times.

3.5. Mapping the solubility of PCL on a Teas graph

A Teas diagram is a scaled representation to evaluate the types of chemical interactions between solvents and materials as a function of polar force, dispersion force and hydrogen bonding [89]. In this study, a Teas graph was used to evaluate the strength of solvent combinations for the dissolution of PCL, and the results of this study are explained in depth in the results section.

The solubility of PCL with a concentration of 12% (w/v) in 22 solvent systems (including pure and mixed solvents) was determined. Each solvent was positioned on a Teas graph using fractional cohesion parameters. The solubility of each sample was checked visually after 24 hours at room temperature. The locations of pure and mixed solvent systems with higher solvation power in the Teas graph were highlighted with a frame.

3.6. Electrospinning

A high voltage power supply (PS375/+20KV, Stanford Research System) was used to create a DC voltage from 5 to 18 kV. A 5 mL glass syringe with an 18 G flat-tip needle was used as a sample container/feeder. A syringe pump (Fisher Scientific) was used to maintain the desired flow rate. The positive electrode from the power supply was attached to the needle and the negative electrode was attached to the grounded collector. A rotating drum with a speed of 100 rpm covered with aluminum foil was used as the collector (Figure 17).

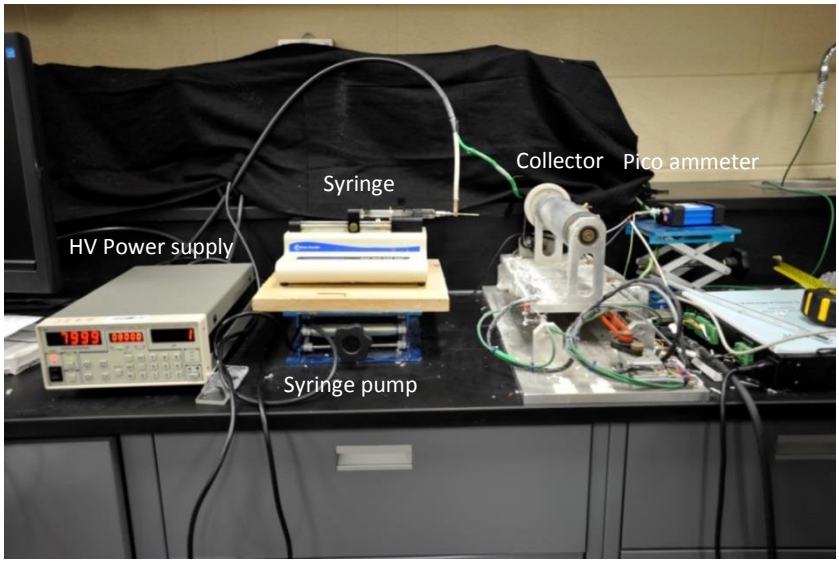

Figure 17: Electrospinning device used in the experiments.

3.7. Characterization of the resulting nanofibers

Different techniques were used to study and analyze the properties of the resulting nanofibers. They included an Imaging System (Scanning Electron Microscopy), an optical microscope, a differential scanning calorimeter (DSC), a dynamic mechanical analyzer (DMA), a Fourier-Transform infrared (FT-IR) spectrophotometer and a Proton Nuclear Magnetic Resonance (^{1}H NMR) spectrometer.

3.7.1. Optical microscope

A Leco500 light microscope was used to visually analyze the morphology of the resulting nanofibers at different magnifications. For this analysis, samples were collected on the surface of microscope slides at the collection point. The collected samples were visually studied using the optical microscope as a quick tool to evaluate the resulting nanofibers before submitting the sample for SEM.

3.7.2. Scanning electron microscopy (SEM)

The nanofiber diameter and fiber morphology was studied using a Philips VP-30XL scanning electron microscope at an accelerating voltage of 15 kV. Aluminum foil was used for collecting the spun fibers. Collected samples were cut in a rectangular shape and fixed to carbon tape. SEM images with magnification of

5000x were used for fiber diameter measurements. The Image J software was used to measure the fiber diameter. In total, 35 fibers from each image were analyzed randomly. For images with fiber counts of less than 35, all fibers were analyzed. Three images over three different samples were analyzed for each studied condition.

3.7.3. Calculation of χ

χ is a dimensionless aspect ratio, or the ratio of jet length before whipping over the whipping radius [83]. Hohman *et al*. state that near the nozzle, l/d (where l is the length of jet before whipping and d is the diameter of the nozzle) can be an acceptable estimate for χ. In this study, χ is calculated using the ratio of the jet diameter at a distance of 3 mm from the surface of the Taylor cone (h) over the length of the polymeric jet prior to whipping (l) (Equation 8 and Figure 18):

$$\chi = \frac{l}{h} \qquad (8)$$

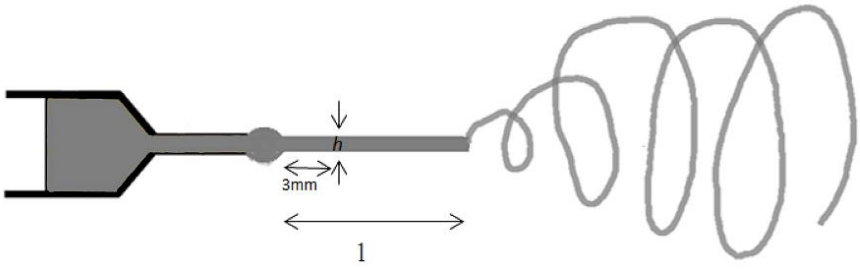

Figure 18: Diagram illustrating *h* (the diameter of the jet at 3 mm from the surface of the Taylor cone) and *l* (the length of the jet) for the calculation of χ.

3.7.4. Differential scanning calorimetry (DSC)

DSC is an analytical technique for thermal analysis which measures the heat difference between the sample and a reference. The principle of DSC is to heat the sample and reference at the same rate and compare the heat change by any thermal event in the sample. The temperature changes in the sample or reference chamber will be compensated by the power supply. The amount of heat supplied is recorded as a signal related to the sample's specific heat. In case of an exothermic event, the temperature of the sample chamber will be raised and the reference chamber needs

more heat to maintain the same temperature (there should be no difference in temperature between the sample and the reference), while an endothermic event will require more heat from the power supply for the sample chamber. A DSC curve is the result of temperature changes during the thermal events (Figure 19). The area under the peak shows the enthalpy change in the sample and the direction of the peak identifies the type of thermal event, exo for exothermic and endo for endothermic event [92]. For example in the Figure 19 exothermic peaks are in the upward direction and endothermic peaks are in the downward direction.

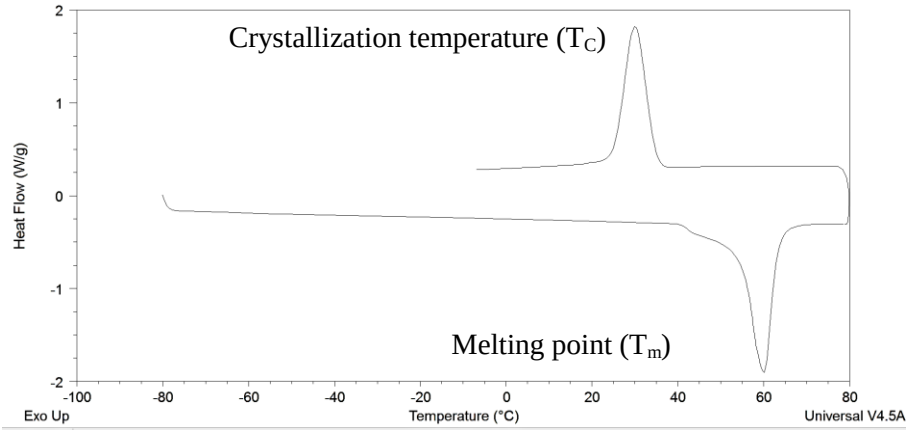

Figure 19: An example of a typical DSC graph (PCL bulk polymer).

DSC analysis was performed using a Q100 Analyzer. Samples between 5 and 8 mg were weighed and placed in a DSC chamber and heated from -80 to 80 °C for PCL samples, while the temperature range for CP-PCL blends was -80 to 250°C. The melting point was measured during the heating cycle at a rate of 10 °C /min, and after holding the temperature at the highest applied temperature for 5 minute (to complete melting), the crystalline temperature was measured during the cooling cycle at a rate of 10 °C/min. The measurement was performed three times for each sample.

3.7.5. Dynamic mechanical analysis (DMA)

DMA is a technique which is used for characterization of a material's physical properties as a function of stress, strain, time, temperature, and a combination of these factors. In this study, a tensile test was applied using a thermal analyzer (TA) instrument Q800 in a controlled force mode (in static mode) with a ramping of 3 N/min up to 18 N. Samples were processed in rectangular shapes with dimensions of L = 20 mm, W = 10 mm and thickness = 0.02 - 0.033 mm with a fiber volume fraction of 20-25%. Analysis was applied in triplet or more for each sample.

3.7.6. Fourier transform infrared spectroscopy (FT-IR)

A PerkinElmer Spectrum 65 FT-IR spectrophotometer was used to obtain FT-IR spectra from samples in KBr pellets. In order to produce KBr pellets, the samples were crushed and mixed with KBr in a ratio of 0.5-1% and pressed to produce the pellet.

3.7.7. ^{1}H NMR

The ^{1}H NMR spectrum for 50 mg/mL PCL or CP in $CDCl_3$ was acquired using a Varian 300 MHz NMR.

3.8. Statistical analysis

A single variable optimization method was selected for statistical analysis, a strategy in which only one factor was changed in different levels, while others were kept constant. In order to perform a statistical study of the results, statistical tools such as single factor ANOVA and the Tukey test were utilized. Single factor ANOVA (analysis of variance) at the 95% confidence level was applied to evaluate the uniformity of fibers collected under each electrospinning condition. Another single factor ANOVA at a 95% confidence level followed by a Tukey test was applied to evaluate the similarity between the electrospinning variables. ANOVA is a combination of statistical analysis to evaluate the difference between means of some groups of data (more than two groups). The outcome of this analysis is the P-Value at a specific confidence level. The difference between the mean of data groups can be evaluated by comparing the P-Value at a significance level. In our case, significance level is 0.05 (95% confidence level), if the P-Value is larger than 0.05 there is no significant difference between groups of data while if this value is smaller than 0.05 there are some differences between these data groups. ANOVA is unable to show which group of data is different from others, while some other tests, such as the Tukey test, can provide more information regarding the similarity and difference between various data groups. In other words, the Tukey test is a technique which can determine which group of data is significantly different among other groups of data [93].

3.9. Determination of the degree of substitution (DS) for CP

Degree of substitution can be defined as the number of substituted hydroxyl group on cellulose. ^{1}H NMR spectroscopy was used to determine the DS of purchased cellulose propionate. A solution of cellulose propionate in deuterated chloroform ($CDCl_3$) with a concentration of 50 mg/mL was prepared for NMR analysis (Figure

20). The protons of anhydroglucose (AGU) or cellulose backbone protons (7H) appear between the chemical shifts of 2.5-5.5 ppm and the methyl hydrogens of the propyl group appear in the range of 0.5-1.5 ppm. The area of these peaks was integrated to calculate the degree of substitution for cellulose propionate [94].

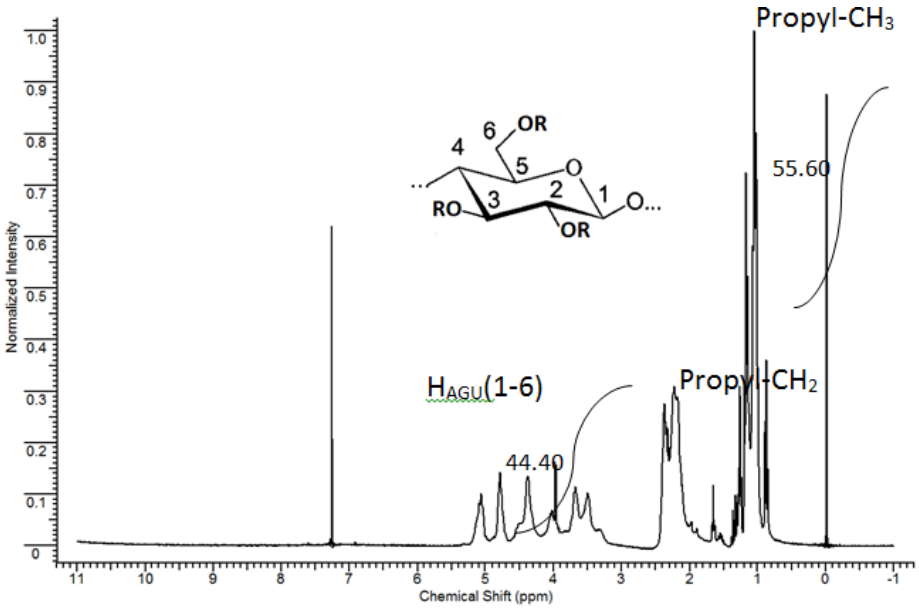

Figure 20: [1] HNMR spectrum of cellulose propionate.

$$DS = \frac{7 * I_{CH3}}{3 * I_{AGU}} \qquad (9)$$

where, I_{CH3} is the integration of the methyl protons; and
I_{AGU} is the integration of the cellulose backbone protons (7H).

The calculated DS, using this method, was 2.92 for CP (maximum is 3). It means that the majority of OH groups on cellulose are replaced by propionate groups.

Chapter 4: Electrospinning Results and Discussion

This chapter is divided into three sections. In the first section, the rationale for the selection of solvents for the electrospinning of PCL is explained using Teas graphs. In the second section, the results of the optimization process for producing PCL neat fibers and CP-PCL composite fibers are reviewed. The optimization process for neat PCL is modeled based on the terminal jet theory. The results of DSC and DMA tests on PCL and CP-PCL nanofibers are discussed in Chapter 5.

4.1. Selection of the solvent system

Intermolecular forces, including Van der Waals, ion-dipole, dipole-dipole, induced-dipole forces and hydrogen bonding, in addition to the physical properties, such as the density and the dielectric constant, can explain the solvent behaviour in a solution. The solvation process is dependent on the solvent and solute molecular interactions, which are governed by intermolecular forces. The Hildebrand solubility parameter can be used to predict solubility. It is related to non-ionic interactions and generally covers the Van der Waals interactions. Charles M. Hansen added two polar interaction parameters and divided the Hildebrand value into three components: the dispersion force, hydrogen bonding and the polar force. These components are called Hansen parameters and are related to the total Hildebrand value through the following relationship:

$$\sigma_t^2 = \sigma_d^2 + \sigma_p^2 + \sigma_h^2 \qquad (10)$$

where, σ_t = total Hildebrand value;
σ_p = polar force parameter;
σ_d = dispersion force parameter; and
σ_h = hydrogen bonding parameter.

These parameters can accurately explain and predict molecular interactions (with the exception of ionic interactions) in solution. A graphical demonstration using these parameters is a tool which helps to evaluate the intermolecular interactions between solvents and solutes. A Teas graph is a triangular 2D graph representing the fractional values derived from the Hansen parameters which locates solvents within the triangle based on their interactions.

A Teas graph was created to provide a map of the solvents used for the dissolution of PCL in order to explain the solubility of PCL in different solutions and to establish a relationship between solubility and the electrospinnability of PCL.

4.2. Calculation of fractional Hansen parameters for pure and binary solvents

The Hansen parameters were extracted from the CRC Handbook [95], calculations were performed according to Luo *et al*. [89,90] and the values are listed in Table 3.

Table 3: Hansen parameters for the pure solvents used to dissolve PCL

Solvent	$б_d$	$б_p$	$б_h$	Sum
Acetone	15.5	10.4	7	32.9
$CHCl_3$	17.8	3.1	5.7	26.6
CH_2Cl_2	18.2	6.3	6.1	30.6
DMF	17.4	13.7	11.3	42.4
MeOH	15.1	12.3	22.3	49.7
THF	16.8	5.7	8	30.5
Ethyl acetate	15.8	5.3	7.2	28.3
1,4-Dioxane	19	1.8	7.4	28.2

The fractional parameters, f_d, f_p and f_h, are calculated using the relationships described below (Equation 11) and the results are collected in Appendix A.

$$f_d=б_d/(б_d+б_p+б_h),\ f_p=б_p/(б_d+б_p+б_h),\ f_h=б_h/(б_d+б_p+б_h) \qquad (11)$$

The percentage of the desired fractional parameter among the total value for all fractional parameters is 100f. The values were plotted on a Teas graph (Figure 21).

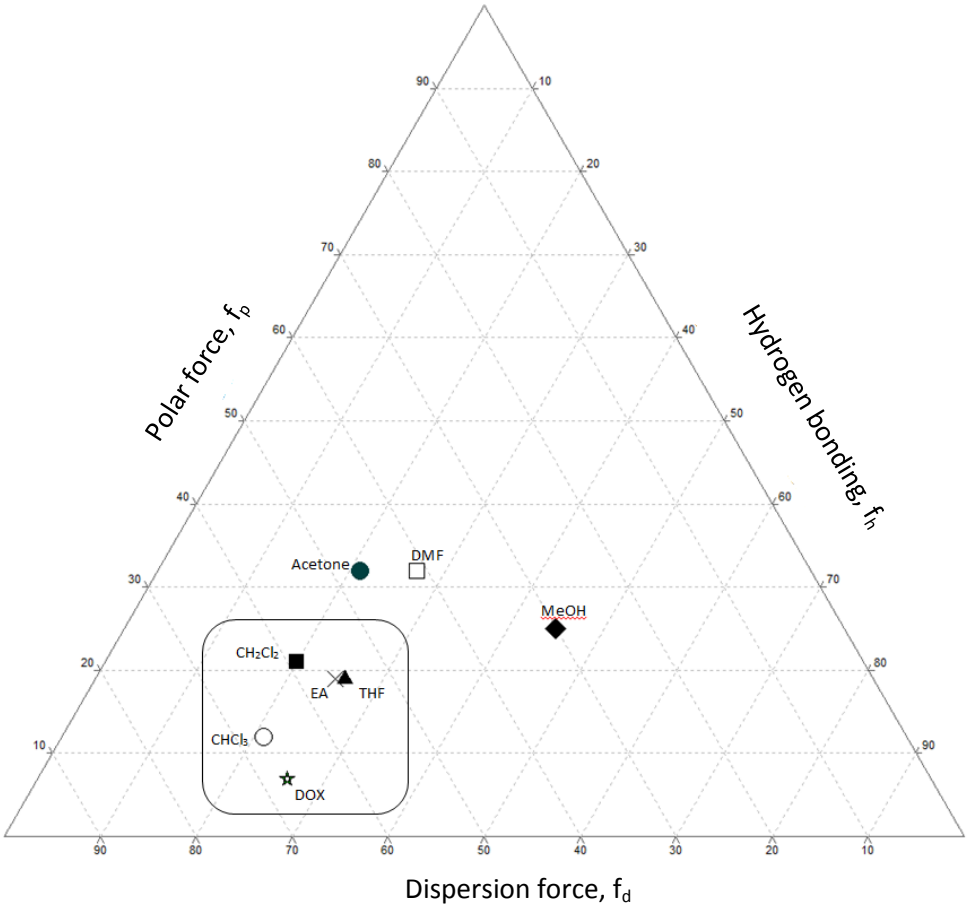

Figure 21: Teas graph for selected solvents. Solvents located in the frame show increased solubility of PCL.

PCL is highly soluble in the solvents located in the frame ($CHCl_3$, CH_2Cl_2, THF, dioxane and ethyl acetate), while PCL is partially soluble in acetone and insoluble in DMF and MeOH. The limited polarity and lack of protic hydrogens in the structural formula of PCL helps to explain the results from the Teas graph (Figure 21), indicating that the dispersion force is the main parameter that can explain the solubility of PCL in the boxed solvents.

The PCL solution in pure solvents could not produce nanofibers, so in order to increase the electrospinnability of PCL, binary solvent systems have been explored. The fractional parameters were calculated according to Appendix B, and summarized in Figure 22.

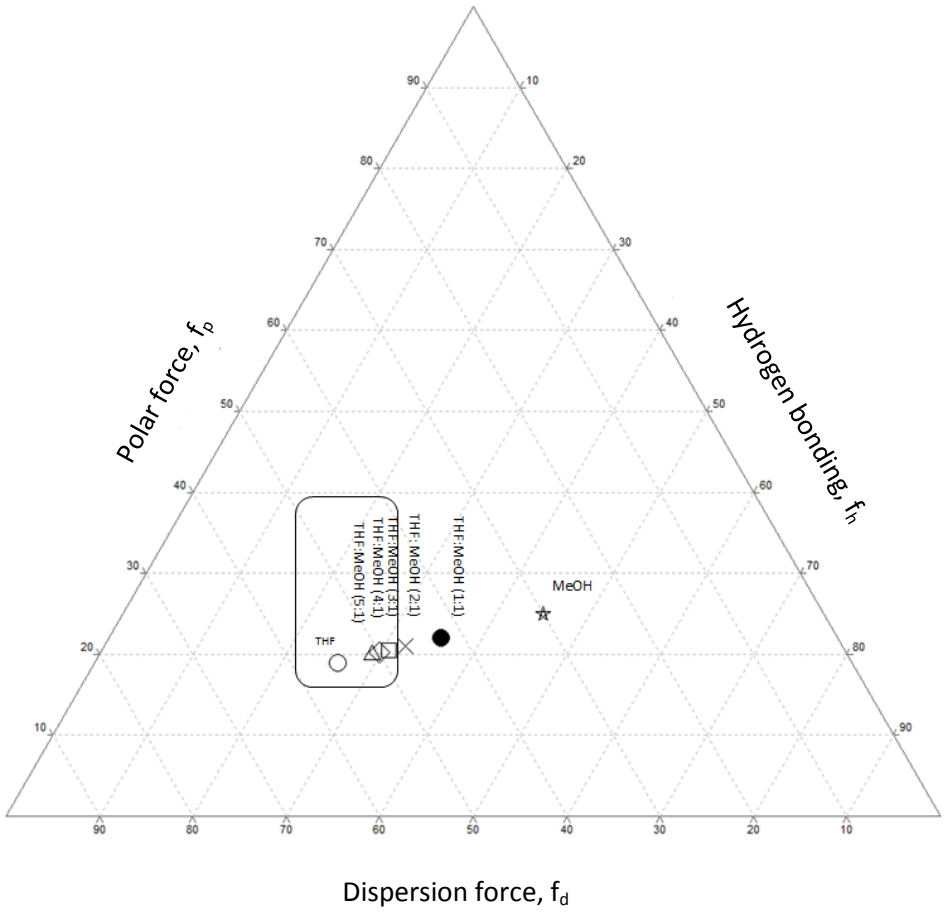

Figure 22: Teas graph for THF:MeOH in different combinations.

PCL was soluble in the THF:MeOH mixtures with ratios of 5:1, 4:1 and 3:1, shown in the frame, while the dissolution of PCL in THF:MeOH mixtures with ratios of 1:1 and 2:1 was temperature dependent. The mixture of 2:1 THF:MeOH needed a solution temperature of 25-30°C in order to dissolve PCL in approximately 4 hours and the resulting solution had to be maintained above 25 °C to remain dissolved. On the other hand, a 1:1 ratio THF:MeOH needed a higher temperature and longer contact time (more than 24 h) to dissolve the PCL. The Teas graph shows that by increasing the percentage of MeOH, the polarity and hydrogen bonding of the solvent system increased while the dispersion force decreased. By combining the results for the solubility of PCL with the Teas graph, it can be concluded that the solvents with higher dispersion forces are suitable for the dissolution of PCL.

Using various combinations of solvents suggested by the Teas graph and other studies, solutions of 12% PCL were electrospun under similar conditions. The resulting nanofibers from only those solutions that generated nanofibers are shown in Figure 23. In each case, fibers are not uniform and contain beads, indicating that the particular conditions for electrospinning were not ideal and would need to be optimized in order to attain uniform nanofibers. The intention from the outset of the project was to avoid halogenated solvents because of their toxicity [9]. Also, ethyl acetate was avoided because of the chance of transesterification during the process. As such, a THF:MeOH blend was selected.

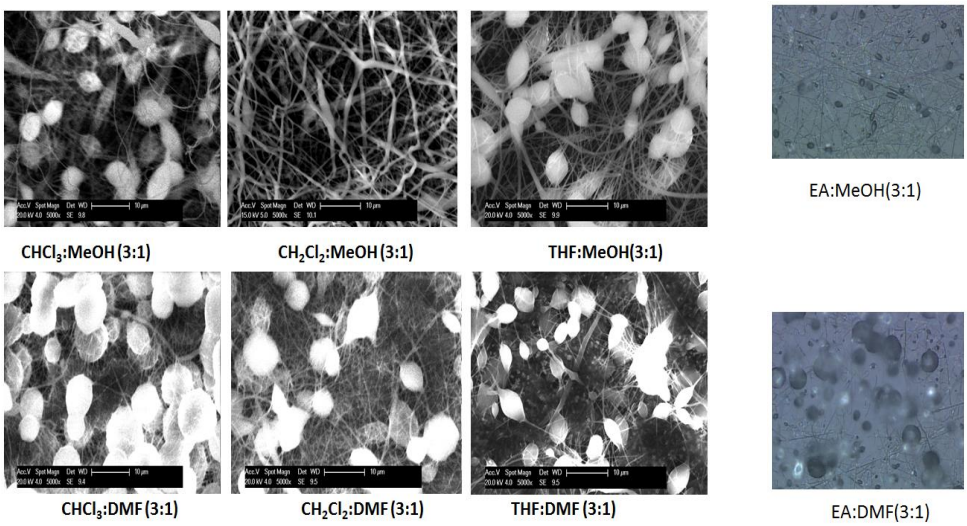

Figure 23: A) Top: SEM images of fibers from solutions of 12% PCL in 3:1 $CHCl_3$, CH2Cl2, and THF with MeOH, respectively. Bottom: SEM images of fibers from solutions of 12% PCL in 3:1$CHCl_3$, CH_2Cl_2, and THF with DMF, respectively. B) Top: light microscope image of fibers from solutions of 12% PCL in 3:1 EA:MeOH. Bottom: light microscope image of fibers from solutions of12% PCL in 3:1 EA: DMF. Electrospinning conditions were constant: 10 kV, tip to collector distance of 10 cm, feed rate of 1 mL/h, and drum speed of 100 rpm.

4.3. Optimization of electrospinning parameters

As mentioned in the introduction, the electrospinning process parameters can influence the diameter and morphology of the resulting fibers. Optimization of these variables is important to obtain uniform fibers with smaller diameters. Each

of these parameters is explored and discussed in greater detail in the following sections.

4.3.1. Optimization of solvent ratio

Solutions of 20% PCL in THF:MeOH mixtures with ratios ranging from 5:1 to 2:1 were prepared. All solutions were used for electrospinning under constant conditions (10 kV, tip to collector distance of 10 cm, feed rate of 1 mL/h and drum speed of 100 rpm).

Generally, by increasing the MeOH ratio in the solvent combination, the dielectric constant of the binary solvent was increased (Figure 24A), while surface tension of the mixed solvent was decreased (Figure 24B). The resulting fiber diameter was decreased using a solvent with a higher dipole moment. The reason can be related to the increase of the repulsion force of ions inside the solvent in the presence of the electric field (Appendix C). The distribution of fiber diameter was studied by providing the histogram for the resulting fiber (Figure 25).

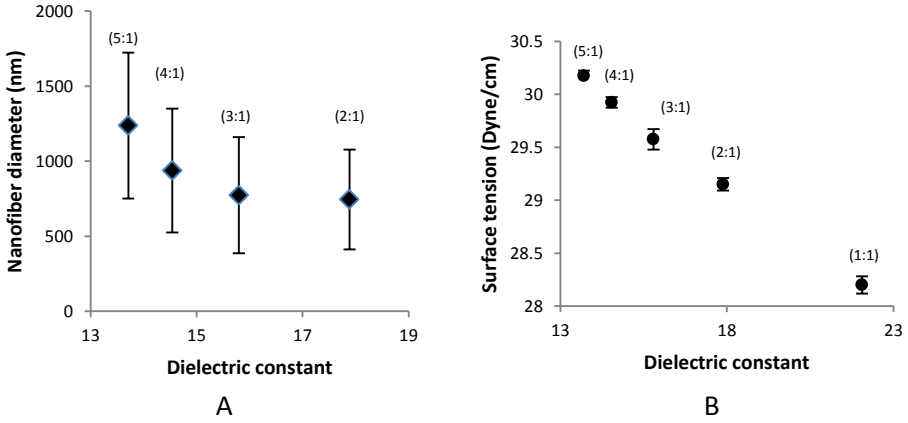

Figure 24: A) Fiber diameter as a function of the dielectric constant of the solvent in ratios of THF:MeOH. B) Surface tension of the solvent as a function of dielectric constant for solvent systems with different ratios of THF:MeOH.

A

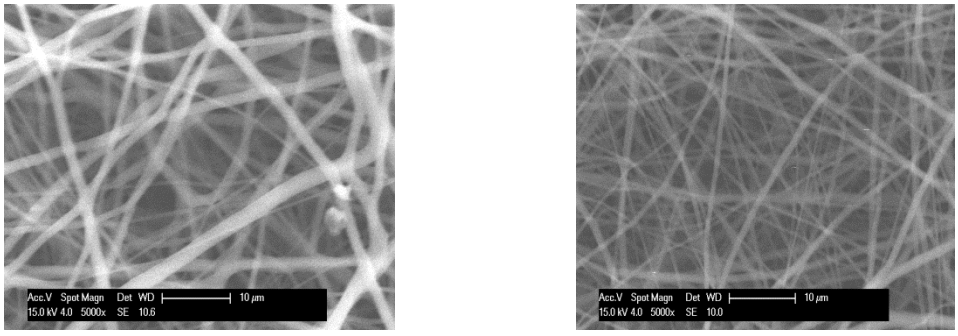

THF: MeOH (5:1)

THF: MeOH (3:1)

B

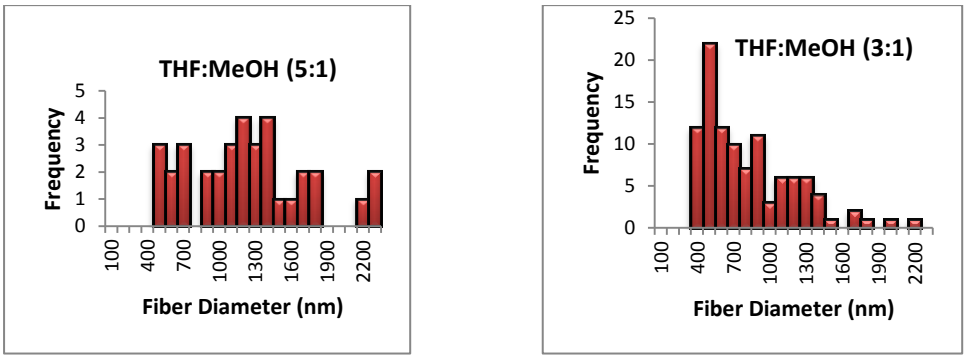

Figure 25: A) SEM images; and B) Diameter distribution for PCL nanofibers resulting from THF:MeOH with different solvent ratios.

Single factor ANOVA was applied to the data to see whether there was any difference between the SEM images resulting from samples under the same conditions. The P-value was compared to the α-value and the results are collected in Appendix C. Results show that there was no statistically significant difference between the fiber diameters of the studied samples in the same conditions (samples from same solvent ratio) at the 95% confidence level which showing that samples belong to one group. In addition, in order to analyze the statistical difference between the resulting fiber diameters from the different solvent systems, single factor ANOVA and the Tukey test were applied and the results are summarized in Appendices C and D. The results of the Tukey test revealed that there was no significant difference between the average fiber diameter resulting from the solvent systems (THF:MeOH) with ratios of 2:1 and 3:1,while these samples were different from the others at the 95% confidence level. Although the solvent system able to produce smaller diameter fibers with smaller variation is the 2:1 THF:MeOH, the dissolution of PCL in that system was temperature dependent and it was insoluble at temperatures lower than 25^{o}C. In order to eliminate

potential solution instability due to temperature fluctuations, the 3:1 THF:MeOH mixture was selected for electrospinning.

4.3.2. Optimization of the PCL concentration

PCL concentrations (w/v%) of 5% to 35% in THF:MeOH (3:1) were prepared for electrospinning (Conditions: applied voltage of 10 kV, tip to collector distance of 10 cm, feed rate of 1 mL/h and drum speed of 100 rpm). The morphology of the resulting fibers was studied using an optical microscope and a SEM. Fiber diameters were measured using the Image J software. For each concentration and conditions yielding only fibers (with minimal beads), SEM images were prepared and fiber diameters were measured (Appendix E).

Lower concentrations starting from PCL 5% to 18% resulted in nanofibers with the presence of beads. The amount of beads decreased with increasing PCL concentration. The 20% PCL solution provided beadless fibers with a higher uniformity. By increasing the PCL concentration above 20%, the average fiber diameter increased, which could be attributed to higher entanglements of the polymer chain resulting in a higher viscosity (Figures 26 and, 27).

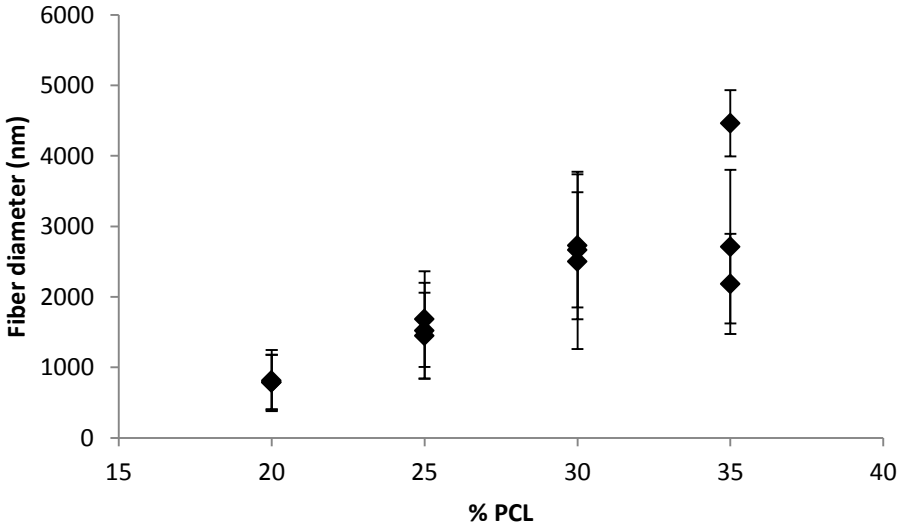

Figure 26: Fiber diameter as a function of PCL concentration (%).

A

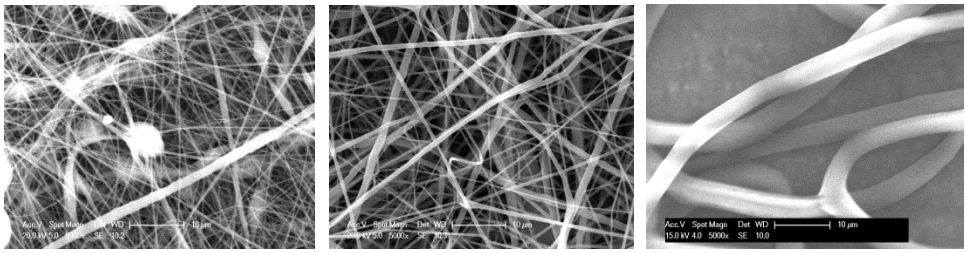

15% PCL 20% PCL 35% PCL

B

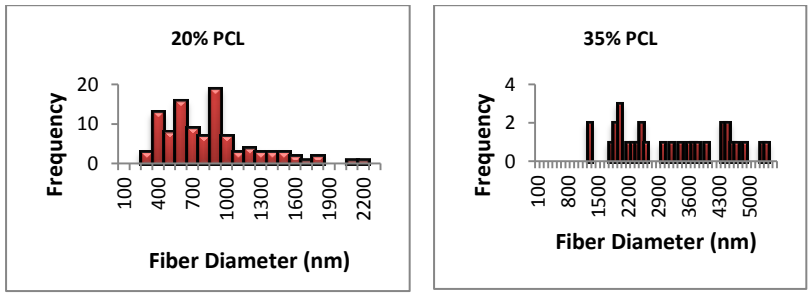

Figure 27 :A) SEM Images for PCL fibers resulting from PCL solutions with different concentrations at 5000x and B) Diameter distributions for spunfibers with 20% and 35% PCL concentrations.

In Appendix E, single factor ANOVA was applied to the spun fiber diameter distribution for each PCL concentration used and the results showed that the fibers for 20%, 25%, and 30% PCL were uniform (p-value > 0.05) while for the 35% PCL solution, the fibers were not uniform (p-value < 0.05). Also, another single factor ANOVA followed by the Tukey test was applied to evaluate the statistical difference between the resulting fibers' diameters from different PCL concentrations and the results are summarized in Appendices E and D. Based on the results of the Tukey test, there was no significant difference at the 95% confidence level between the diameter of the fibers obtained from 30% and 35% PCL solutions, while the diameter of the fibers from 20% and 25% PCL solutions were statistically and significantly different. The 20% solution was selected as the optimized concentration due to the production of uniform fibers with smaller diameters.

In order to study the effect of process parameters on the electric current and its relationship with fiber morphology, the electric current generated during processing was measured using a Pico ammeter connected in series with a 1 kΩ resistor. This configuration allowed the measurement of current in the nA range at high voltage. A diagram of the circuitry of the device is shown in Appendix F. Figure 28 shows the measured current as a function of processing time for

solutions with PCL concentrations of 20%, 22% and 25%, from bottom to top, respectively. Visually, the three different concentrations displayed vastly different measured currents, suggesting different mechanisms by which the current travels to the collector through the PCL solution. At a 25% PCL concentration, the measured current fluctuated considerably between 60 and 500 nA. At a 22% PCL concentration, the current was fairly stable at 60 nA, except for the occasional spikes up to 300 nA. At a 20% PCL concentration, the current was very stable at 38-40 nA.

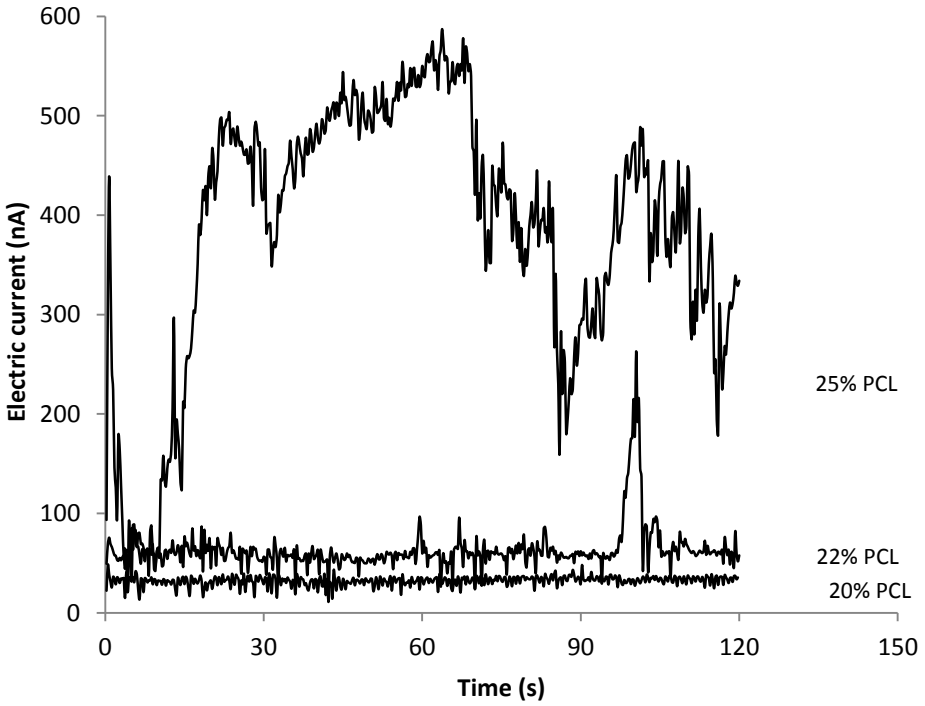

Figure 28: Electric current as a function of processing time for PCL concentrations of 20%, 22% and 25% in THF:MeOH (3:1) (from bottom to top).

The measured current displayed considerable fluctuations when spinning with PCL concentrations higher than 20%. In general, two different current regions were identified: an upper plateau and a lower plateau, as demonstrated in Figure 28. Pictures taken during electrospinning point towards two different mass transfer mechanisms, as shown in Figure 29. The upper current plateau was associated with splitting of the polymer jet, as shown in the bottom portion of Figure 29. The lower current plateau was associated with the whipping motion of one single jet, as shown in the top portion of Figure 29.

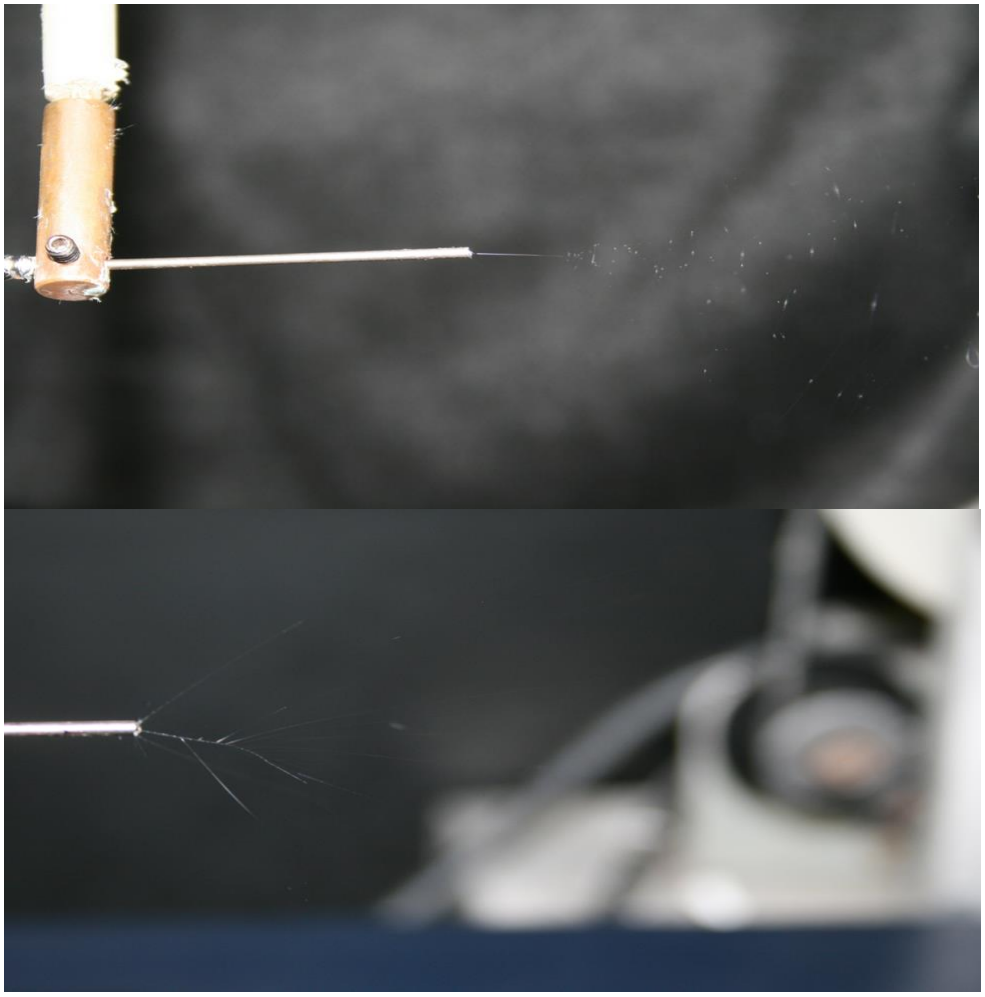

Figure 29: Images showing the dominant whipping action observed for a 20% PCL solution (Top) and the dominant splitting action observed for a 25% PCL solution (Bottom).

The observed splitting action of the polymer jet increases the amount of electric current carried by the polymer solution. The carried electric current can be explained by Equation (12). In the case of splitting, the right hand side of the equation is the sum of the carried electric current by each branch of the split jet:

$$I = (2\pi б hv + \pi EKh^2)_1 + (2\pi б hv + \pi EKh^2)_2 + (2\pi б hv + \pi EKh^2)_3 + \cdots \quad (12)$$

In order to model the optimization process based on the terminal jet theory, only the electric current resulting from the whipping motion (lower plateau for 22% and 25% PCL) has been considered (Appendix G and Figure 30).

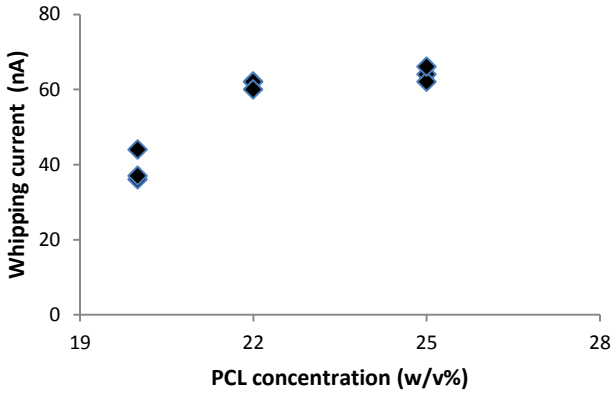

Figure 30: Whipping current as a function of PCL concentration

The slightly higher whipping current observed at higher PCL concentrations could be related to viscosity. The higher viscosity would translate to whipping with a smaller circular radius, which can decrease the total resistance and path length. Evidence of whipping diameter relationship with the PCL concentration was indirectly observed by measuring the diameter of the spot size on the collector (Appendix G and Figure 31). The results confirm the reduced whipping diameter for solutions with higher PCL concentration.

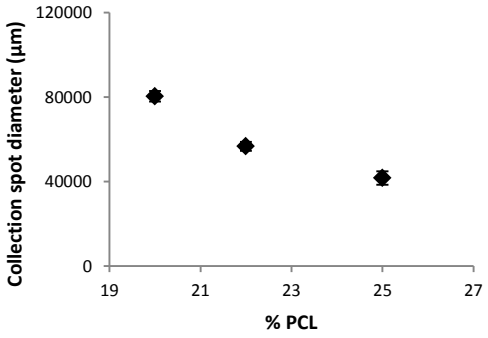

Figure 31: Effect of polymer concentration on collection spot diameter (TCD is 10 cm, voltage is 10 kV flow and rate is 1 mL/h).

The needle tip to the collector distance can be divided into two sub regions. The first region is the straight jet and the second one is the whipping region (see Figure 18). These two regions can be considered as series resistors against the electric

current between two electrodes. Length and thickness of the jet is an important factor which can affect the amount of carried current. The length of the whipping region is more important due to the longer length of the polymer jet bent during whipping and the circular movement. Given this fact, an increase in the length of the straight jet can decrease the length of the whipping zone. As a result, total resistance involving both regions is decreased and the outcome is a higher electric current. Figure 32 shows how jet diameter and jet length were changed as a function of polymer concentration [96].

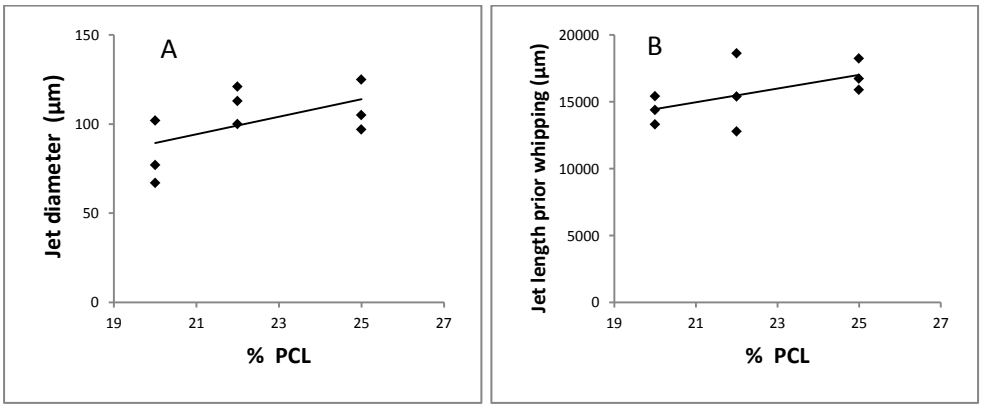

Figure 32: Effect of polymer concentration on A) jet diameter and B) jet length prior to the onset of whipping (TCD is 10 cm, voltage is 10 kV and flow rate is 1 mL/h).

The terminal jet theory, Equation (5), was applied to the experimental results. In order to apply this model, the parameter χ, also called the local aspect ratio (relationship between a polymer jet width and its length before the whipping zone), must be determined. χ was calculated using the ratio of L/h, where L is the length of the jet prior to whipping and h is the diameter of the jet (Appendix G).

The fiber diameters predicted with Equation (5) for PCL solutions of 20, 22 and 25% are shown in Figure 33. Some assumptions were considered in order to apply the model. First, it was assumed that most of the solvent evaporates during electrospinning, before the fibers reach the collector. The solvents used are very volatile and whipping results in a high surface area. Q_c was used in the model. Q is the flow rate generated by the syringe pump and C is the concentration of the polymer in percentage. Q_c is the flow rate at the collecting point and was defined as $Q_c = Q \times C$. The second assumption was to consider $\chi = 160 \pm 17$, which was the average calculated for the concentrations in Figure 32. Supporting data and calculations are provided in Appendix H.

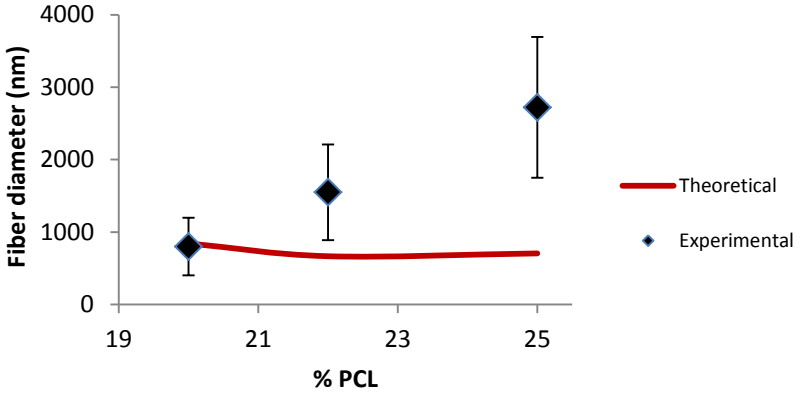

Figure 33: The effect of polymer concentration on experimental and theoretical fiber diameter (error bars show standard deviation of fiber diameter).

The results show that the model predictions are only in agreement for the spinning performed at a 20% PCL concentration. The experimental fiber diameter for PCL with concentrations higher than 20% results from both the whipping and splitting actions. The model only applies when there is whipping, which leads to smaller diameters due to extensive deformation and stretching of the polymer jet.

4.3.3. Optimization of the applied voltage

The electrospinning process was optimized as a function of the applied voltage using a 20% PCL in THF:MeOH (3:1) solution. Other process parameters such as the tip to collector distance, the feed rate and the collecting drum speed were kept constant at10 cm, 1 mL/h and 100 rpm, respectively.

The applied voltage generates the field between the tip and the collector responsible for creating the Taylor cone from which the polymer jet originates. At a lower potential difference of 5 kV, the volume of the Taylor cone was larger and some transfer of the polymer into droplets was observed. By increasing the potential difference, the volume of the Taylor cone decreased and at 18 kV it almost disappeared. In Figure 34, the fiber diameter is reported as a function of the applied voltage and SEM images of the resulting fibers, along with histograms of the diameter distributions, are shown in Figure 35.

The results of Figures 34 and 35 indicate an optimum voltage between 8 and 10 kV was required to produce more uniform fibers with a smaller diameter. The application of a higher voltage produced fibers with larger diameters which can be attributed to charges at the surface of the jet traveling faster at higher voltages, thereby increasing the mass flow rate.

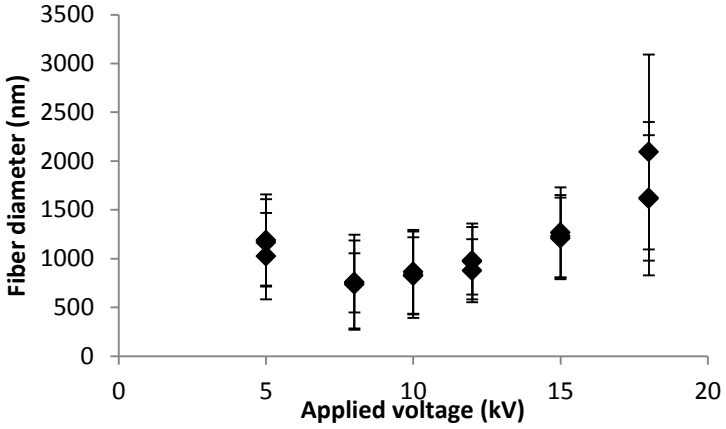

Figure 34: Fiber diameter as a function of applied voltage (TCD is 10cm and flow rate is 1 mL/h).

The p-Value for single factor ANOVA at the 95% confidence level shows that there is no statistically significant difference between the studied three samples collected under the same applies voltage.

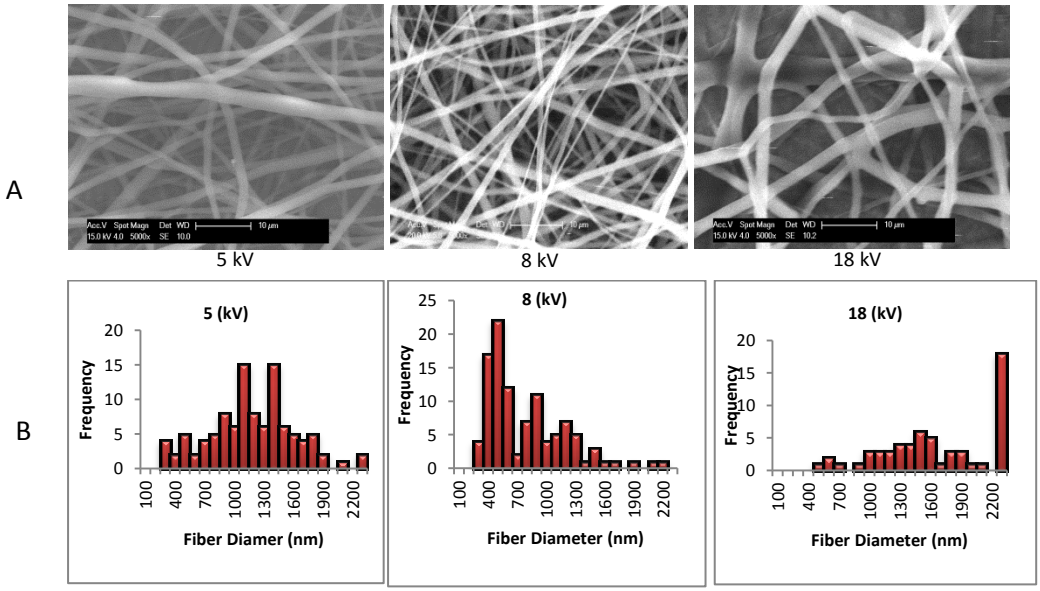

Figure 35: A) SEM images, and B) Diameter distribution for fibers resulting from 20% PCL in THF:MeOH (3:1) solutions at different applied voltages.

Another single factor ANOVA at a 95% confidence level was applied to evaluate the differences between fibers resulting from different electric field strengths and

the resulting P-value was less than 0.0001, indicating that there was a statistically significant difference between the mean values of fiber diameters in different electric field strengths.

The Tukey test was applied to see which data set was different from the others, as shown in Appendices I and D. Based on the mean value for the diameter of the resulting fibers at 8 kV and 10 kV, they produced fibers with smaller diameters and the result of the Tukey test showed that they were not significantly different from each other at a 95% confidence level. Based on the above analysis, 8 kV was selected as the optimized applied potential because it could produce fibers with smaller diameters at lower standard deviation.

Electric current measurements at the applied voltages during the electrospinning process provided valuable information about the mass transfer mechanism. The electrospinning current was measured for 120 seconds at quarter-second intervals. Figure 36 shows the measured electric current for a 20% PCL solution in THF: MeOH (3:1) at a flow rate of 1 mL/h and applied voltages of 8 kV (A) and 15 kV (B). The higher voltage current instabilities seen for 15 kV started at 12 kV.

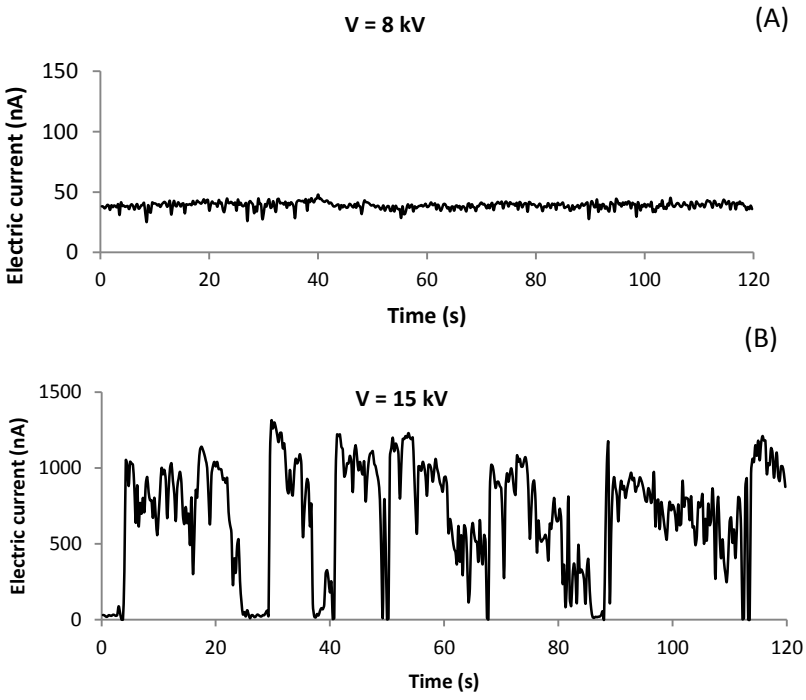

Figure 36: Measured current as a function of processing time at 8 kV (A) and 15 kV (B).

The measured electric current includes the current carried due to the surface charge density and the conductive solvent at the surface of the polymer jet that evaporated during electrospinning. In this context, the higher rate of solvent evaporation would yield a lower electric current. As shown in Figure 36, the current fluctuates between higher and lower current values associated respectively with the splitting action, illustrated in the bottom portion of Figure 37, and the whipping action, illustrated in the top portion of Figure 37. Whipping is observed as a single polymer jet stretching and spiraling towards the collector. Splitting is seen as a polymer jet split in many branches following a more direct path towards the collector.

The outcome of the splitting action is a higher electric current due to the summation of the electric current carried by the many split jets (Equation 12). Based on observations that were made during electrospinning and the measured electric current, splitting occurred 30% of the processing time at 12 kV and increased up to 80% of the time at 15 kV. At voltages higher than 10 kV (12, 15 and 18 kV), the whipping current was identified as the lower current plateau of Figure 36 and in Appendix J.

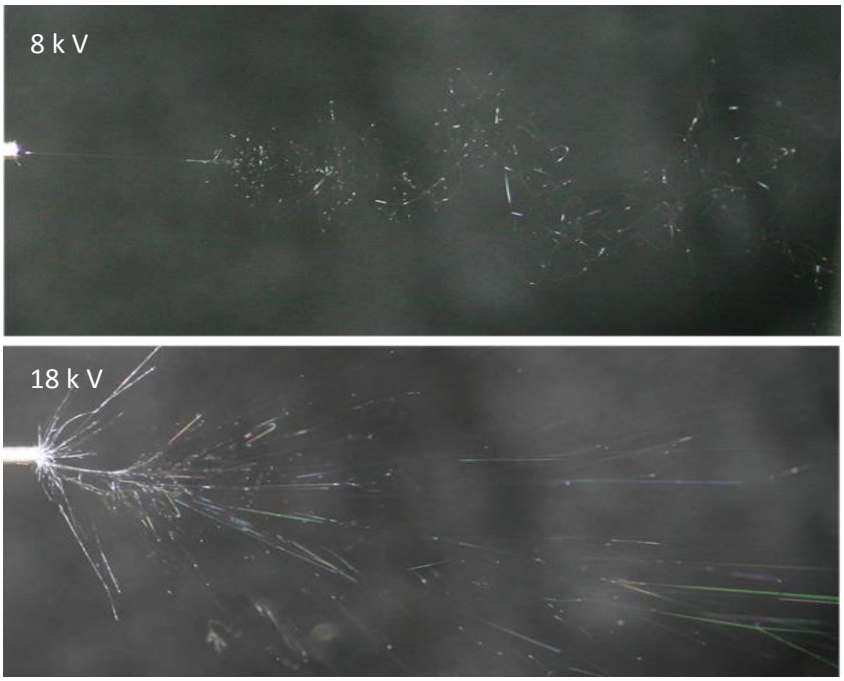

Figure 37: Pictures illustrating the whipping (at 8 kV, top) and splitting (at 18 kV, bottom) actions.

When modelling the electrospinning process using the terminal jet theory, only the electric current resulting from the whipping action was used (Appendix K). Figure 38 shows the relationship between the applied voltage and the measured electric current for the whipping action (the line is the average amount of measured whipping current for different applied voltage). The downward trend of the whipping current at higher voltages is consistent with the dominance of the splitting action observed at those voltages, as shown in Figure 36.

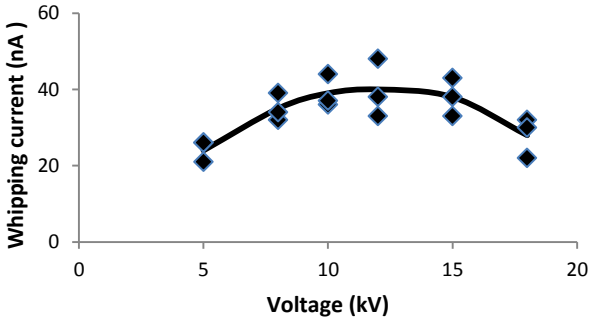

Figure 38: Relationship between measured electric current and applied voltage.

Figure 39 shows the diameter (h) and the length (L) of the polymer jet, prior to the onset of whipping, as a function of the applied voltage. The higher voltage created a higher electric field which could draw a larger amount of polymer into the field. As a result, the diameter of the jet increased. Larger jet diameters would delay the migration of charges to the surface of the jet and result is an increase in the length of the jet before the whipping instability occurred due to the accumulation of a high concentration of charges at the surface of the jet (Figure 39).

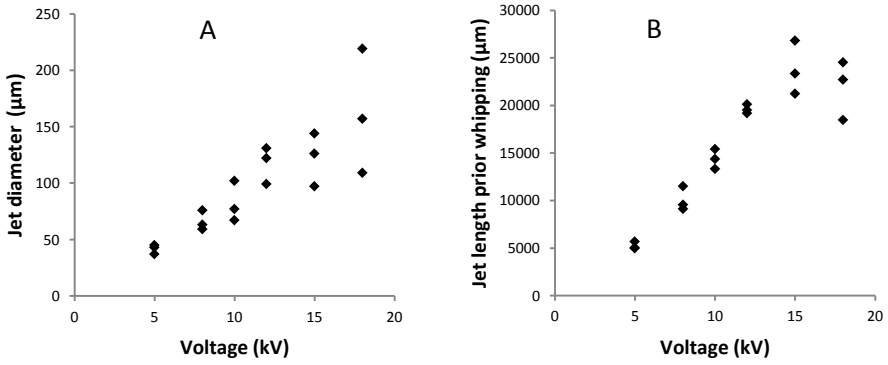

Figure 39: Effect of applied voltage on A) jet diameter; and B) jet length prior to the onset of whipping (TCD is 10cm and flow rate is 1 mL/h).

In Figure 40, the terminal jet theory (expressed as Equation 5) was used to predict the diameter of the spun fibers as a function of process parameters. The whipping current values reported in Figure 38 were used along with $\chi = 150$, which was calculated as L/h as reported in Figure 39, and Q_c ($Q_c = Q \times C$) as previously explained in Section 4.3.2. The model prediction agrees well with the measured fiber diameters except at higher voltages where the observed splitting action becomes more dominant and deviates from the conditions for which the model applies. As seen in Figure 37, the splitting action generated less stretching of the polymer jet due to the absence of whipping and resulted in fibers with larger diameters. Detailed calculations for χ are found in Appendix K.

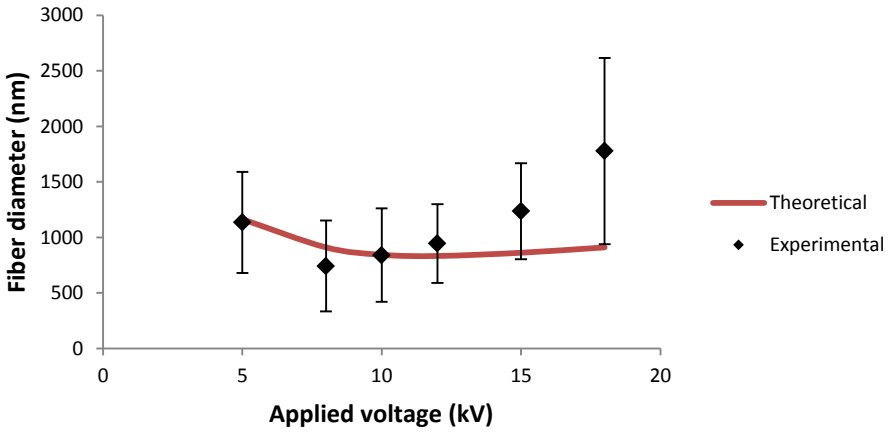

Figure 40: Fiber diameter, predicted by the terminal jet theory, as a function of the applied voltage.

4.3.4. Flow rate optimization

The electrospinning process was optimized as a function of the flow rate using a 20% PCL in THF:MeOH(3:1) solution. The morphology of the fibers was studied using SEM imagery and the fiber diameter was measured using the Image J software shown in Figure 41. Detailed results have been tabulated in Appendix M. In Figure 42, the fiber diameter is reported as a function of the flow rate. Results show that there was an optimum flow rate at 0.5 mL/h that produced more uniform fibers with a smaller diameter. At 0.2 mL/h, surface tension effects dominated producing an inconsistent flow that generated fibers with a broad range of fiber diameter. At flow rates higher than 0.5mL/h, nanofibers with larger diameters were produced, most likely due to a lower stretching of the polymer jet.

.

A

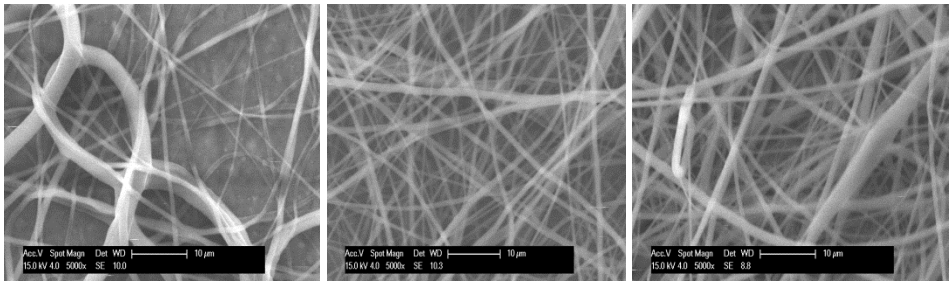

Flow rate= 0.2 mL/h | Flow rate= 0.5 mL/h | Flow rate= 1.5 mL/h

B

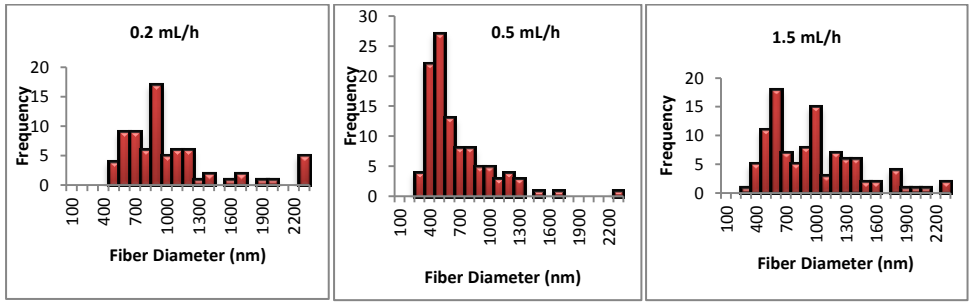

Figure 41: A) SEM images; and B) Fiber diameter distribution for the resulting fibers at different flow rates.

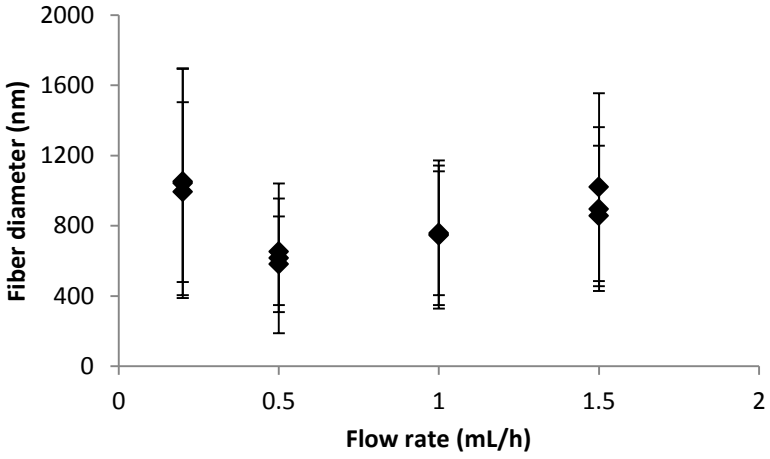

Figure 42: Fiber diameter as a function of flow rate (TCD is 10 cm and voltage is 8 kV).

The uniformity of the samples was evaluated using the single factor ANOVA. P-Values in Appendix M displaying resulting fiber diameters for all flow rates were distributed uniformly at the 95% confidence level (P-Value > 0.05). In addition, the results from the Tukey test revealed that there was no statistically significant difference between the average value for the fiber diameters resulting from 0.5 mL/h and 1 mL/h at the 95% confidence level. Based on this analysis, 0.5 mL/h was confirmed as the optimized flow rate, as explained previously using Figure 41, but also because the fiber diameters obtained at that flow rate were lower than those obtained at other flow rates.

In Figure 43, a sample of the electrical current as a function of processing time is shown for a solution flow rate of 0.5 mL/h. Under these conditions, the whipping action dominated and there was no splitting action observed. The current was very steady around 20 nA, fluctuating mostly between 10 and 30 nA. The steady observed whipping action explains why the fiber diameter distribution was narrower under the processing conditions reported for Figure 43.

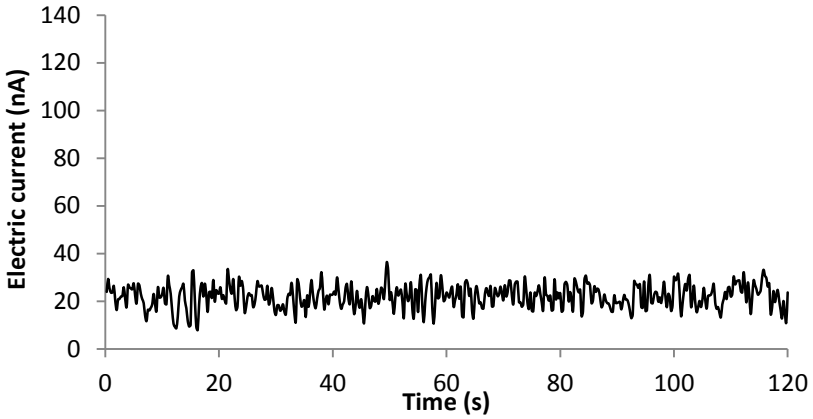

Figure 43: Electric current vs time for a flow rate of 0.5 mL/h (TCD was 10cm and voltage was 8 kV).

In Figure 44, the whipping current is shown to increase with the flow rate. The trend in increased whipping current cannot be related strictly to the increase in flow rate. The diameter of the processed fibers changed from one condition to the next as reported in Figures 41 and 42, also indicating corresponding changes in the surface area of the polymer jet during processing. Smaller polymer jets have a larger surface area per volume and, in accordance with the terminal jet theory, that would make them more conductive. This is particularly apparent in Figure 44 at higher flow rates where the whipping current is almost the same at 1 mL/h and 1.5 mL/h while the resulting fiber diameter is larger at 1.5 mL/h.

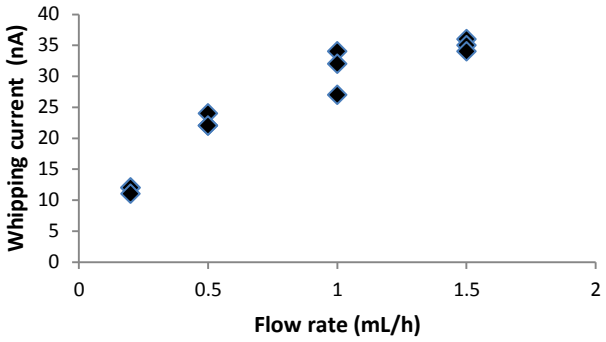

Figure 44: Whipping current as a function of flowrates used during electrospinning (TCD is 10cm and voltage is 8 kV).

In Figure 45, the terminal jet theory, expressed as Equation 5, was used to predict the diameter of the spun fibers as a function of process parameters. The whipping current values reported in Figure 44 were used along with $\chi = 125$, which was calculated as L/h as reported in Appendix N, and Q_c ($Q_c = Q \times C$). The model shows a rising trend in fiber diameter with increased flow rate from 0.2 to 1.5 mL/h. The experimental data comply with this trend, except for at a flow rate of 0.2 mL/h. Based on observations made at 0.2 mL/h, the flow exiting the tip of the syringe and used in the whipping process was not steady and led to large variations in fiber diameter, as seen on the right side of Figure 45.

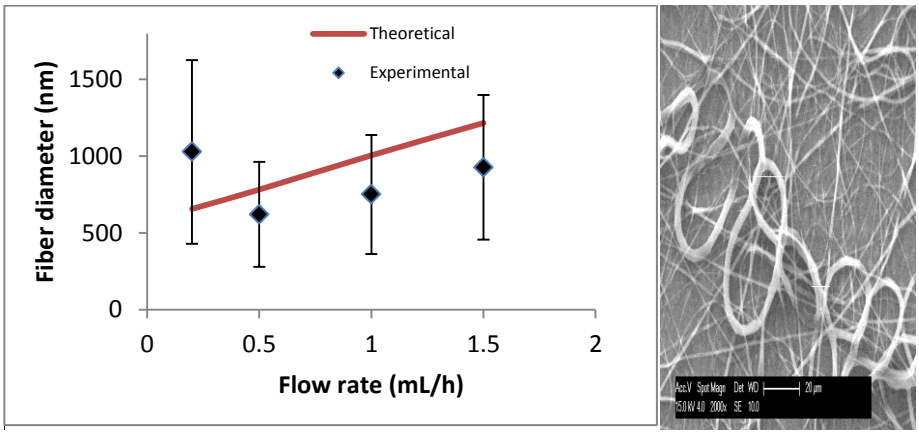

Figure 45: Spun fiber diameter as a function of flow rate used during processing (Left)(error bars are the standard deviation for fiber diameter) and SEM image showing an inconsistent fiber diameter for a flow rate of 0.2 mL/h (Right).

4.3.5. The optimization of tip to collector distance (TCD)

The electrospinning process was optimized as a function of tip to collector distance (TCD) using a 20% PCL in THF:MeOH (3:1) solution. Other processing parameters were V = 8 kV and Q = 0.5 mL/h. The morphology of the fibers was studied using SEM imagery and the fiber diameter was measured using the Image J software. Detailed results are tabulated in Appendix O.

In Figure 46, the spun fiber diameter is reported as a function of the tip to collector distance (TCD). Results show that by increasing the TCD, fiber diameters decrease. For longer TCDs, there was enough flight time to have the solvent evaporate and the fiber stretch. By increasing the TCD at a constant voltage, the volume of the Taylor cone was increased due to a resulting lower electrical field. At a TCD of 20 cm, gravity effects were noticeable as fibers increasingly missed the target.

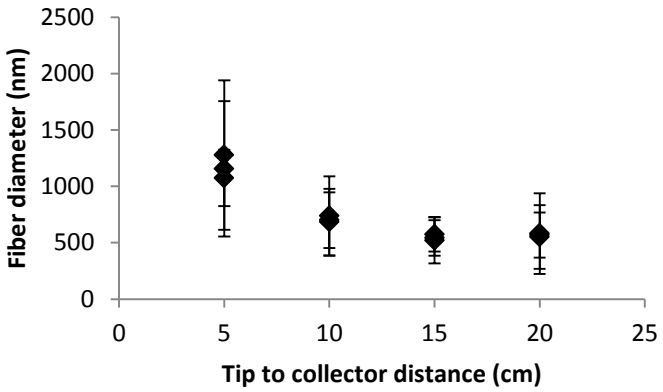

Figure 46: Flow rate versus the fiber diameter (Applied voltage is 8 kV and flow rate is 0.5 mL/h).

A

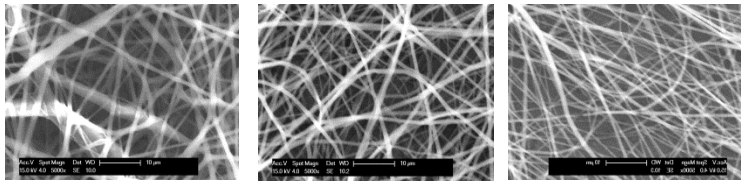

TCD = 5 cm TCD = 10 cm TCD = 15 cm

B

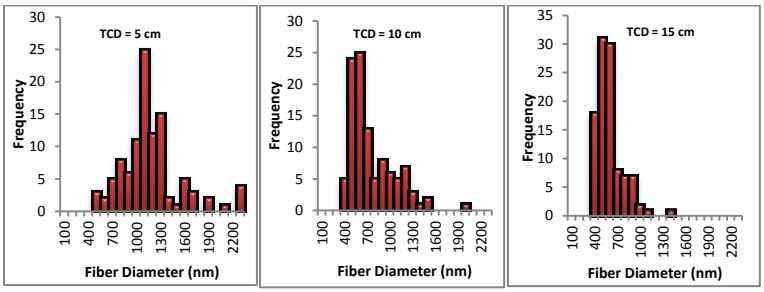

Figure 47: A) SEM images and B) diameter distribution for the fibers spun from a 20% PCL in THF:MeOH (3:1) solution for different TCDs.

In Figure 47, sample SEM micrographs with corresponding fiber diameter distribution bar graphs are presented. Based on the resulting P-values, fibers are uniformly distributed in the sample area for each distance at the 95% confidence level (P-Value > 0.05). An ANOVA test followed by a Tukey test was applied to evaluate the similarity between the data set of different TCDs. The P-value > 0.0001 showed that there was a statistically significant difference between the mean values of the data sets at a 95% confidence level. In addition, based on the results from the Tukey test, there was no statistically significant difference between the average value for fiber diameters resulting from a TCD of 15 cm and 20 cm at the 95% confidence level. Further details are provided in Appendices O and D. At a TCD of 20 cm, gravity caused adverse effects; therefore, a TCD of 15 cm was selected as the optimum distance.

In Figure 48, TCDs of 5, 10 and 15 cm produced steady whipping with no major current fluctuations in the range of 16 to 24 nA. At a TCD of 20 cm there were periods of time when no current was carried, corresponding to interruptions in the electrospinning process, or in another words, there was no flow of jet toward the collector. This observation was attributed to a weak electric field at that distance that was unable to produce a continuous jet flow towards the collector.

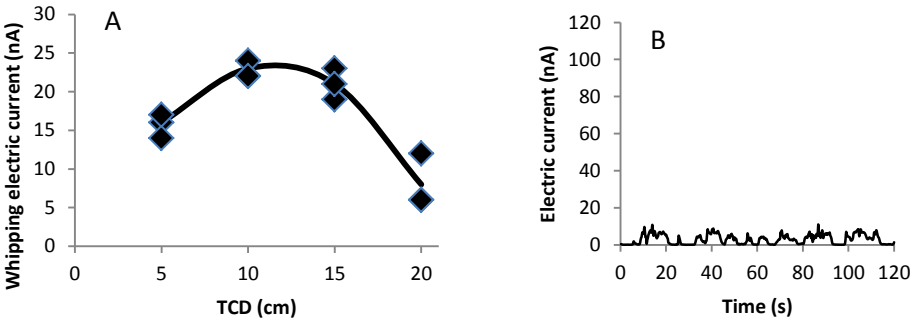

Figure 48: A) Whipping current as a function of TCD (line is the average amount for measured whipping current); and B) Measured electric current as a function of processing time for a TCD of 20 cm.

In Figure 49, the terminal jet theory, expressed as Equation 5, was used to predict the diameter of the spun fibers as a function of process parameters. The whipping current values reported in Figure 48 were used along with χ = 130, which was calculated as L/h as reported in Appendix P, and Q_c ($Q_c = Q \times C$).

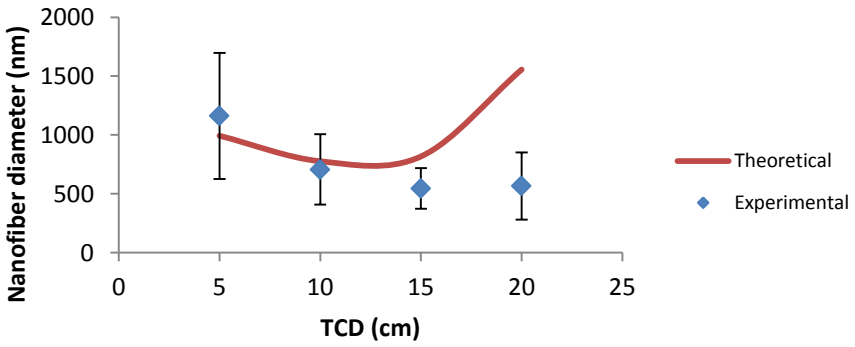

Figure 49: Spun fiber diameter predicted by the terminal jet theory as a function of TCD.

As shown in Figure 49, the experimental and modelled spun fiber diameter do not agree, especially at a TCD of 20 cm. This was attributed to the observed non-continuous flow of the polymer jet due to the lower electric field strength at a TCD of 20 cm.

4.4. Optimization of electrospinning process for PCL and cellulose propionate blends

In order to enhance the thermal and mechanical properties of PCL nanofibers, poly-caprolactone and cellulose propionate blends (CP-PCL) were prepared. The optimization of the electrospinning process for PCL was used as a starting point for the polymer blend. A 50/50 CP-PCL blend at a 20% w/v concentration in THF:MeOH (3:1) was used as the polymer solution for the process optimization. As for PCL, applied voltage, flow rate and tip to collector distance were optimized toward smaller spun fiber diameters and a narrow fiber diameter distribution.

4.4.1. Optimization of applied voltage for CP-PCL blends

A 20% CP-PCL (50/50) in THF:MeOH (3:1) solution was electrospun for applied voltages between 5 and 15 kV and constant conditions with a flow rate of 0.5 mL/h and a TCD of 12 cm. The morphology of the resulting nanofibers was studied using SEM images and the fiber diameter was measured using the Image J software. Detailed results are collected in Appendix Q.

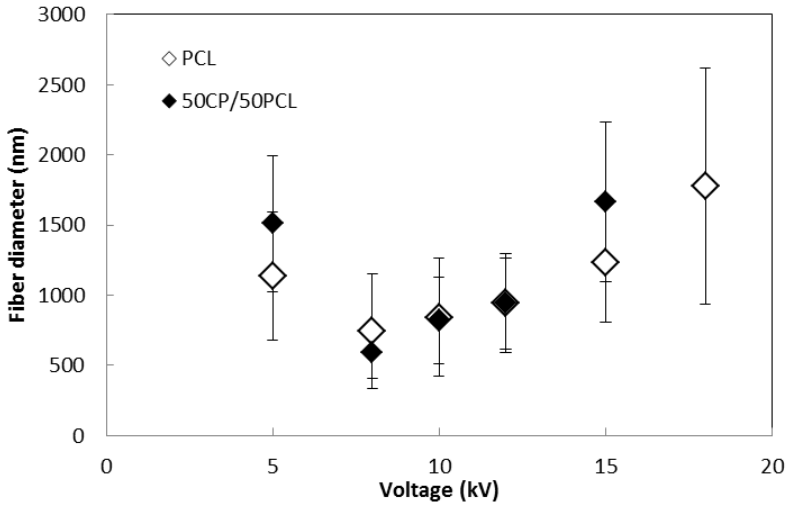

Figure 50: Spun fiber diameter for CP-PCL as a function of applied voltage. Other processing conditions were TCD = 12 cm and Q = 0.5 mL/h (conditions for PCL: 20% PCL, 10 cm and 1 mL/h).

Figure 50 reports the spun fiber diameter for CP-PCL as a function of applied voltage. Results indicate an optimal voltage at 8 kV to obtain smaller fibers with a narrow fiber diameter distribution. The CP-PCL results follow a similar trend as those for PCL although the other processing conditions differ. This suggests that

the flow rate and the TCD have less of an impact on the spun fibers than the applied voltage.

In Figure 51, sample SEM micrographs with corresponding fiber diameter distribution bar graphs are presented. At 5 kV, the larger fiber diameter and the SEM micrographs of Figure 51, suggest that the lower electrical field was not strong enough to generate a steady state electrospinning process. At voltages higher that 8 kV, the splitting action became increasingly dominant at the expense of the whipping action, resulting in increasingly larger fibers.

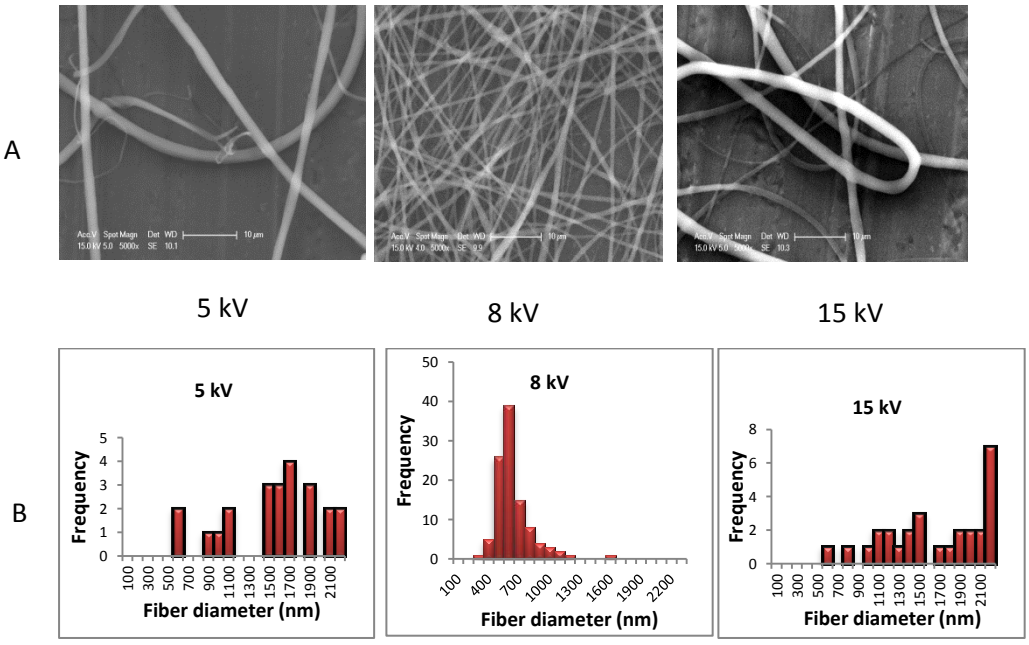

Figure 51: A) SEM images and B) histograms to show the fiber diameter distribution resulting from the electrospinning of CP- PCL (50/50) under different applied voltages.

The P-value (p-value > 0.05) resulting from applying single factor ANOVA shows that there was no significant difference in the nanofiber diameters among the three samples for each applied voltage.

4.4.2. Optimization of the flow rate for the CP-PCL blends

The electrospinning process was optimized as a function of the flow rate using a 20% CP-PCL in THF:MeOH (3:1) solution. Other process parameters such as the tip to collector distance and the applied voltage were 12 cm and 8 kV, respectively.

In Figure 52, the spun fiber diameter is presented as a function of flow rates between 0.2 and 1.5 mL/h. Results indicate an optimal flow rate at 0.5 mL/h to obtain smaller fibers with a narrow fiber diameter distribution. The CP-PCL results follow a similar trend as those for PCL. The results also confirm that the flow rate has less of an impact on the spun fibers than the applied voltage. Detailed results have been tabulated in Appendix R.

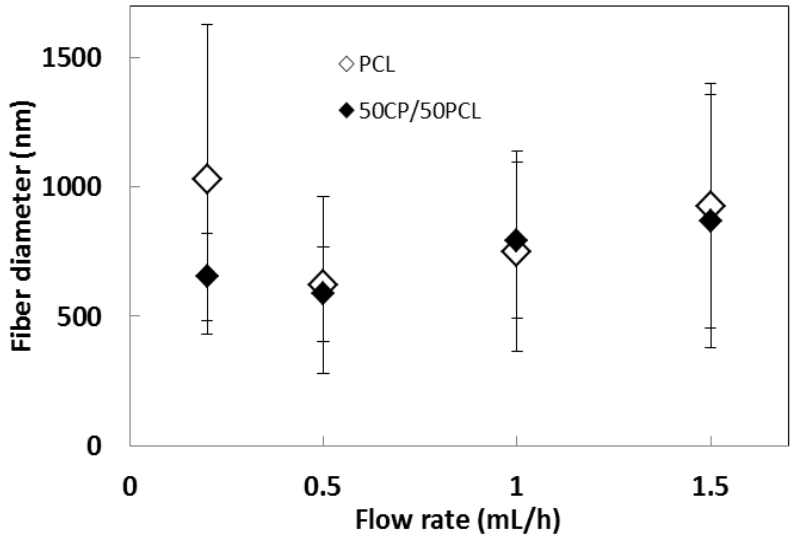

Figure 52: Spun fiber diameter as a function of flow rate for CP-PCL solutions. Other processing conditions were TCD = 12 cm and v = 8 kV (Conditions for PCL: 20% PCL, 10 cm)

As for PCL, flow rates larger than 0.5 mL/h produced nanofibers with larger diameters, as shown in Figure 53. Size distribution was studied, producing histograms that show narrower distributions for 0.5 mL/h. In general, results show that there is no major difference in the resulting fiber diameter for 20% PCL (conditions for PCL: 20% PCL, 12 cm and 8 kV) and CP-PCL blend (conditions: 8 kV and 12 cm) under different flow rates. Based on the resulting fiber diameter and uniformity, 0.5 mL/h was selected as the optimized flow rate.

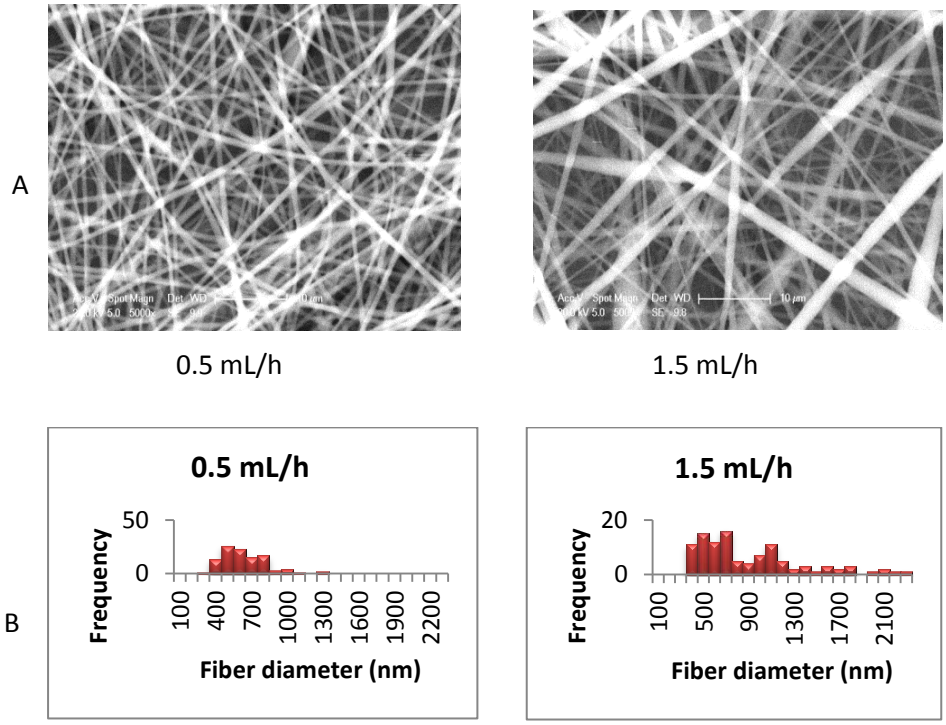

Figure 53: A) SEM images for fibers spun at different flow rates of a CP-PCL solution and B) histograms showing the fiber size distribution.

4.4.3. Optimization of the TCD for the CP-PCL blend

The electrospinning process was optimized as a function of tip to collector distance (TCD) using a 20% CP-PCL in THF:MeOH (3:1) solution. Other process parameters were V = 8 kV and Q = 0.5 mL/h. The morphology of the fibers was studied using SEM imagery and the fiber diameter was measured using Image J software (shown in 54). Figure 55 presents the spun fiber diameter as a function of TCD from 5 cm to 20 cm. Results of Figures 54 and 55 indicate that an optimal TCD range between 12 and 15 cm produced the smallest fibers with the narrowest fiber diameter distribution. Comparison of the SEM images of Figure 54 showed larger fibers for the shorter TCD which was attributed to the limited stretching of the polymer jet due to the short flight time to the collector. The detailed results are tabulated in Appendix S.

A

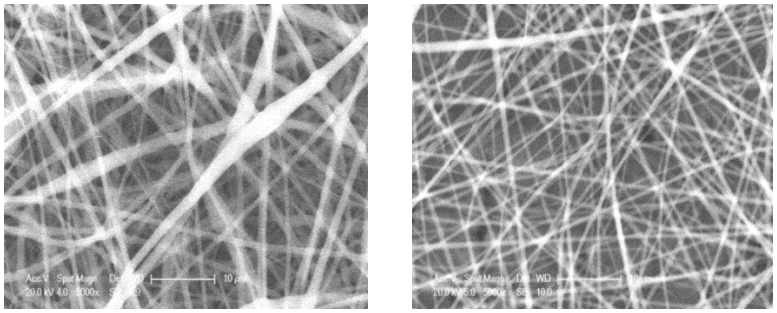

TCD = 5 cm TCD = 15 cm

B

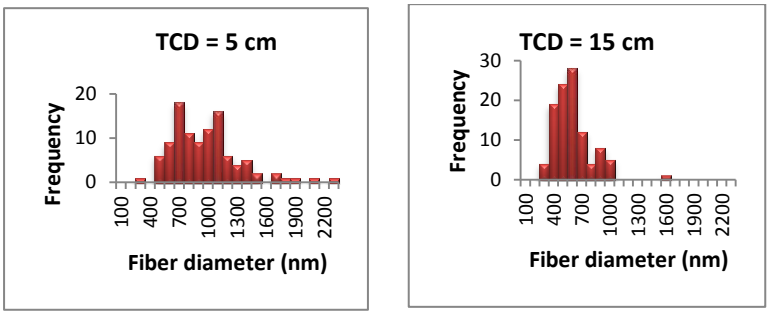

Figure 54: A) SEM images for spun fibers from CP-PCL blends at different TCDs and B) histograms showing fiber size distribution.

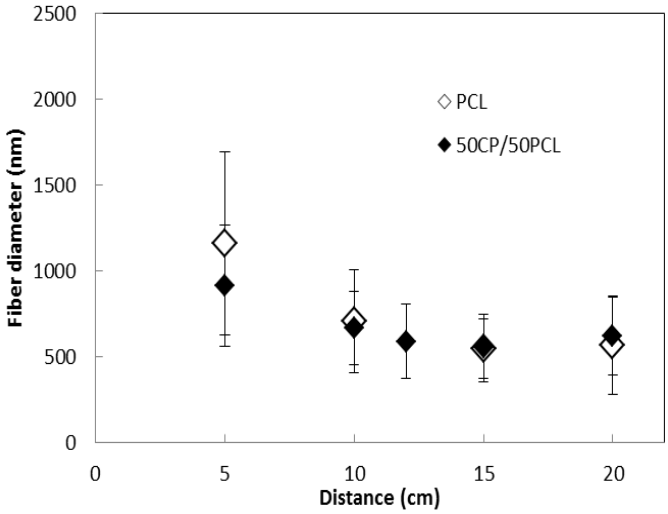

Figure 55: Fiber diameter as a function of TCD for both PCL and CP-PCL blends (conditions for PCL: 20% PCL, 0.5 mL/h and 8 kV).

Process variables were optimized for a 20% CP-PCL (50/50) blend in THF:MeOH (3:1) solution at a flow rate of 0.5 mL/h with a TCD of 15 cm and applied voltage of 8 kV. These conditions produced spun nanofibers with the smallest diameter and the narrowest distribution at 551±197 nm.

Chapter 5: Characterization of the resulting nanofiber

This chapter is divided into three sections. In the first section, FT-IR was used to compare the chemical structure of the processed PCL nanofibers with the Capa™ 6500 to evaluate if any chemical changes occurred during sample preparation and electrospinning. In section two, DSC results for PCL and CP-PCL nanofibers are presented and discussed. Finally, in section three, DMA results for PCL and CP-PCL nanofibers are presented and discussed.

5.1. FT-IR Spectroscopy

Capa™ 6500 was frozen using liquid nitrogen and ground to prepare a KBr pellet. The IR spectra for both the bulk PCL and the PCL nanofibers are presented in Figure 56.

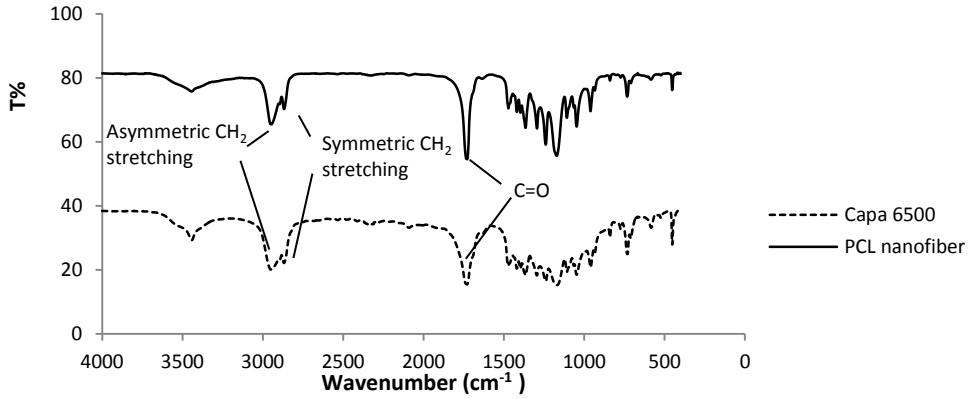

Figure 56: FT-IR spectra for both the PCL nanofibers and the bulk polymer.

In addition to the strong peaks at 2900 cm^{-1} and 1700 $cm^{-1}$for the methyl and carbonyl groups, respectively, the asymmetric C-O-C stretching peak around 1250 cm^{-1}, the C–O stretching around 1200 $cm^{-1}$and the remaining peaks in the finger print region indicated that there was no major chemical change in the PCL structure following the sample's dissolution and processing by electrospinning.

5.2. Differential scanning calorimetry (DSC)

In this section, the thermal properties of the resulting nanofibers, including neat PCL and CP-PCL blends are studied using DSC results and discussed.

5.2.1. Differential scanning calorimetry (DSC) of PCL spun fibers

In order to evaluate the effect of electrospinning on some thermal properties of PCL, DSC tests were conducted. The melting point (T_m), crystallization temperature (T_C) and degree of crystallinity for the bulk PCL and resulting PCL spun fibers are summarized in Appendix T.

The degree of crystallinity, X_c, was calculated using Equation (13), where ΔH is enthalpy of melting and ΔH^* is the theoretical heat of fusion for crystalline PCL (considered to be 142 J/g [97]).

$$X_c\,(\%) = \frac{\Delta H}{\Delta H^*} * 100 \qquad (13)$$

The DSC thermographs of Figure 57 suggest an increase in the degree of crystallinity for the spun nanofiber. Also, T_m and T_C are slightly increased for the resulting PCL nanofibers in comparison to the bulk polymer which is consistent with a higher crystallinity. Based on the results, it seems that the electrospinning restrained and rearranged polymer chains in a more orderly manner and increased the crystallinity of the polymer [19].

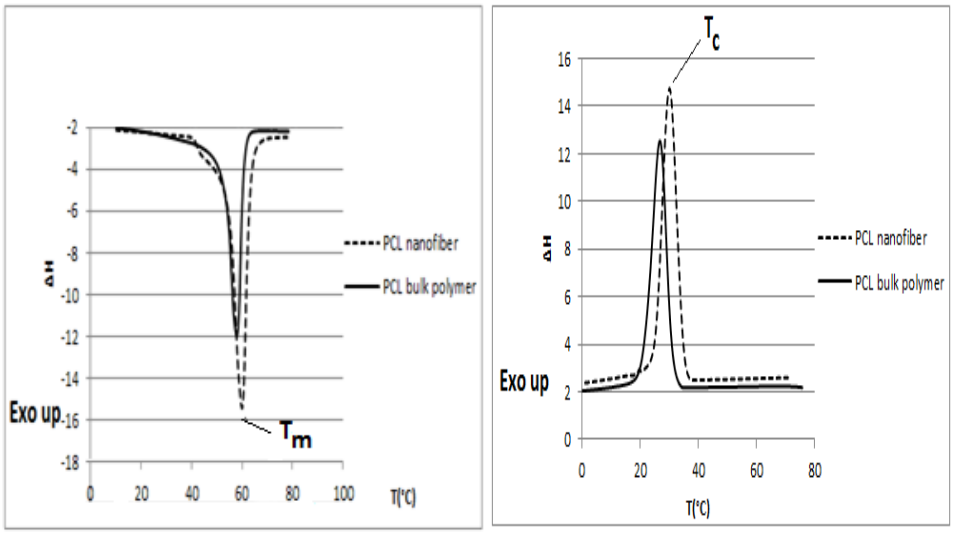

A B

Figure 57: DSC thermograms of PCL nanofibers and the bulk polymer for A) the melting cycle and B) the cooling at rates of 10 °C/min.

The DSC thermograms showing the glass transition temperature (T_g) for the electrospun nanofibers and the bulk polymer are shown in Figure 58. The T_g was slightly lower for the spun fibers which is consistent with other work [98,99].

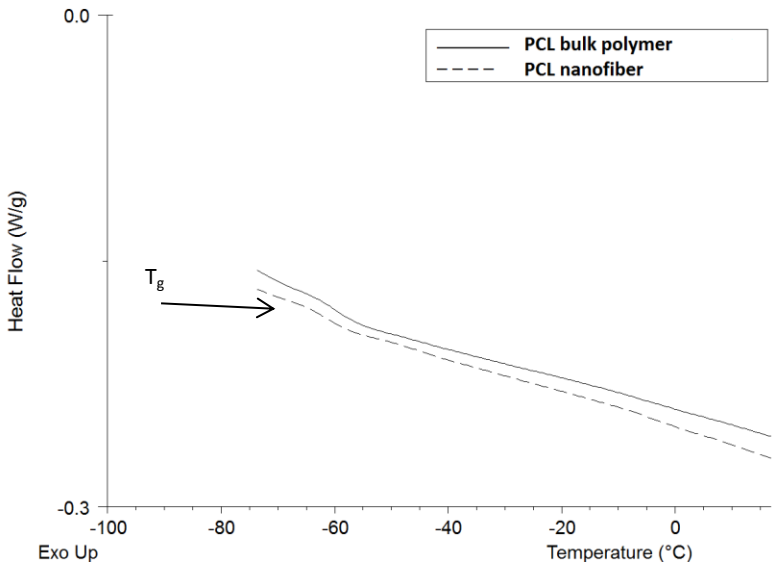

Figure 58: DSC thermograms showing T_g for both the spun PCL and the bulk polymer T_g.

The lower T_g of the spun nanofiber was attributed to an inner stress within the spun nanofibers which keeps more energy inside the PCL and leads to a lower T_g [98]. Other work suggested that the higher surface to volume ratio of electrospun membranes could accommodate air inside the membrane acting as a plasticizer [99].

5.2.2. Differential scanning calorimetry (DSC) of CP-PCL spun fibers

Figure 59 shows the thermograms for the spun fibers of CP-PCL blends. Detailed results are tabulated and reported in Appendix T.

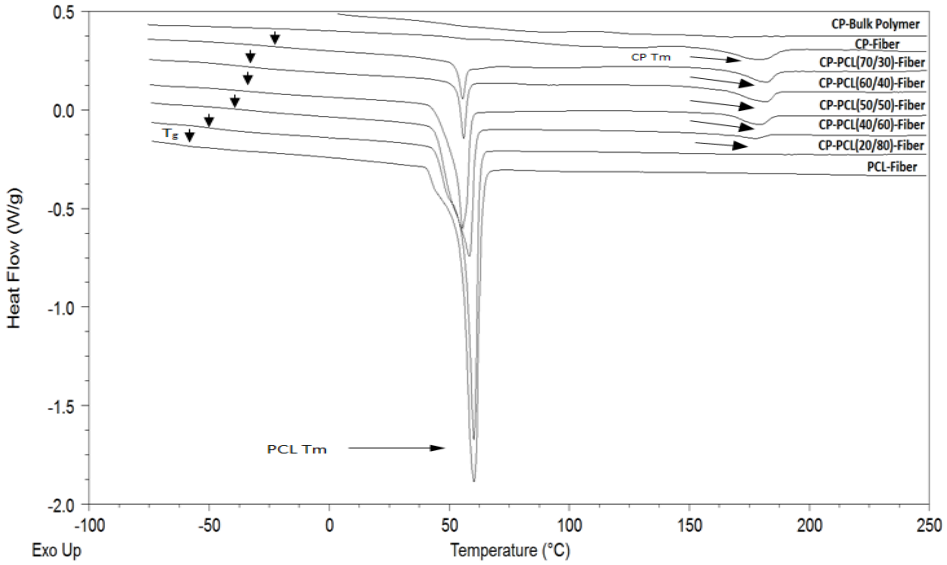

Figure 59: DSC thermograms for the bulk CP polymer, PCL spun fiber and the CP-PCL blended spun fiber.

The results show that the PCL spun fiber has a distinctive melting point around 60 °C and a T_g around - 60°C. By blending some cellulosic propionate (CP) to the PCL, some changes in the thermal properties of the individual polymers occurred.

By increasing the percentage of CP in the CP-PCL blends, the crystallinity of PCL dramatically decreased, as presented in Figure 60. In addition, the T_g of PCL increased from -60 °C to around -25 °C for the CP-PCL (70/30). The change in T_g can be attributed to some degree of miscibility between the PCL and the CP [100]. The crystallinity within the blends was measured using the following equation:

$$X_c\,(\%) = \frac{\Delta H}{\Delta H^* * w} * 100 \qquad (14)$$

where *w* is the weight fraction of PCL in CP-PCL blends.

Figure 59 shows that there is no distinctive melting point for the bulk CP polymer while electrospinning of the polymer generated a distinctive melting point for CP around 180 °C. This melting behaviour for the spun CP could be attributed to an increased orientation of polymer chains during electrospinning.

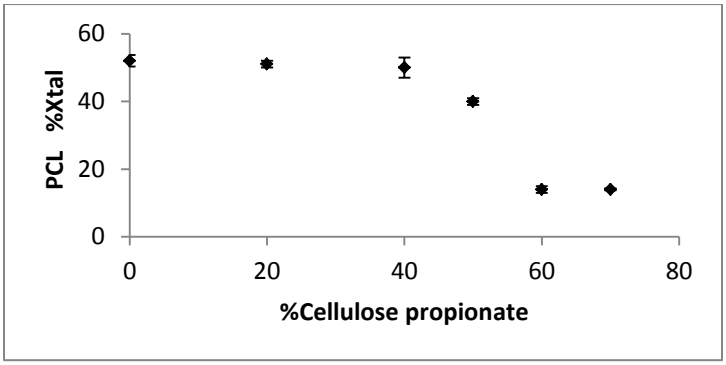

Figure 60: Normalized PCL crystallinity as a function of the percentage of CP in the blends.

5.2.3. Tensile strength using DMA

Tensile strength of the PCL spun fiber and the CP-PCL spun fiber was measured using DMA and summarized in Appendix U. Figures 61 and 62 show that the tensile strength of the spun PCL is lower than that for spun CP-PCL blends. The tensile strength of the CP-PCL blends increased with CP content, reaching a maximum for a 50/50 blend.

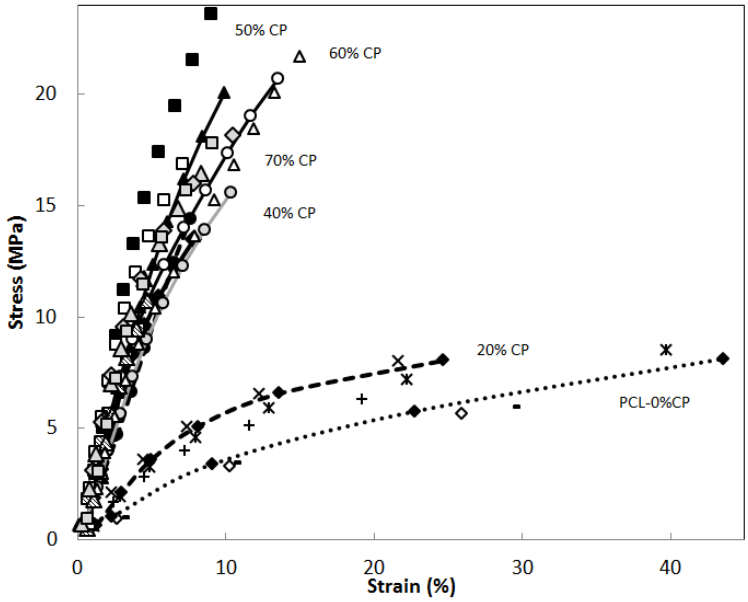

Figure 61: Stress strain behaviour of spun PCL and spun CP-PCL blend fibers (Lines represent the average amount of stress for each blend combination as a function of strain).

Spun PCL displayed higher strain at break than the spun CP-PCL blends. Strain reduced with increased CP content as reported in Figures 61 and 62. CP clearly reinforced PCL.

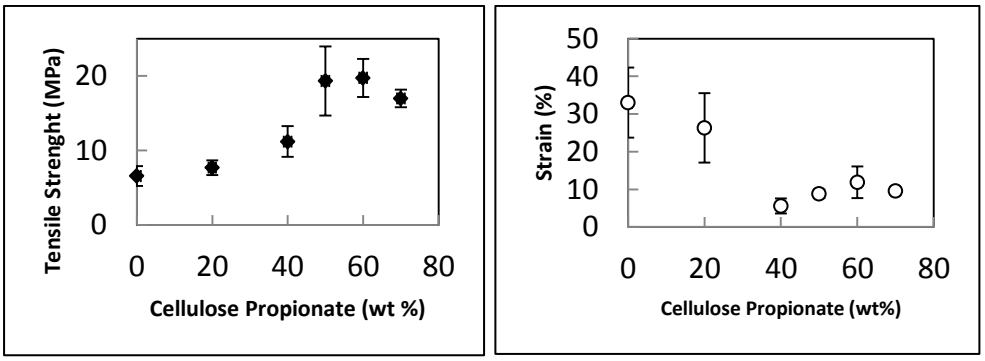

Figure 62: Tensile strength (left) and strain (right) as a function of CP content in CP-PCL blends.

Chapter 6: Conclusions

The solubility of PCL in various solvents, for electrospinning, was studied and mapped using Teas graphs. The location of solvents in the Teas graph shows that dispersion forces are important for the dissolution of PCL. In order to use a solvent with a lower toxicity, a mixture of THF and methanol was selected as the main solvent system for electrospinning, as opposed to often-used halogenated solvents. Teas graphs revealed that a binary solvent system, including one with a higher dielectric constant, enhanced the spinnability of PCL. In this regard, MeOH as a conductive solvent with a higher dielectric constant was added to THF in order to make a binary solvent system for the effective electrospinning of PCL. SEM results revealed that the selection of the solvent system was important for processing uniform fibers. The use of the selected solvent system for the electrospinning of PCL permitted more control of the morphology of the resulting fibers as a function of variables such as applied voltage, polymer flow rate and tip to collector distance.

The electrospinning parameters were optimized for neat PCL and CP-PCL blends towards smaller fiber diameters with the narrowest fiber diameter distribution. The obtained spun PCL fiber diameter was effectively modeled as a function of process variables and measured current during the electrospinning process using the terminal jet theory. Observations made during processing and experimental results revealed that the type of jet action (whipping or splitting), jet length, jet diameter and whipping diameter are important factors influencing the observed electrical current during the electrospinning process. Whenever the jet motion is whipping, experimental fiber diameters fits closely with the model, while there is a big gap between theoretical and experimental fiber diameter when the splitting motion is dominant. The splitting motion was observed for PCL concentrations higher than 20% and applied voltages higher than 10 kV. Overall, the parameters most influential on processing the spun fibers were the polymer concentration and the applied voltage.

The 20% PCL in THF:MeOH (3:1) was determined to be the optimized solution for processing nanofibers with a flow rate of 0.5 mL/h at an applied voltage of 8 kV and a tip to collector distance of 15 cm. Nanofibers with a diameter of 546±173 nm were processed using these optimized conditions. The optimized conditions were also used to process fibers from a 20% CP-PCL (50/50) blend solution yielding fibers with a diameter of 551±197 nm.

DSC of the processed fibers revealed that the crystallinity of PCL increased when compared to the bulk polymer. For spun CP-PCL fibers, the crystallinity of the PCL decreased with increased CP content in the blend. DSC results also suggested

that electrospinning increased the orientation in CP to the extent that the polymer displayed a melting behaviour.

DMA results conducted on membranes made of spun fibers displayed optimal tensile strength for spun fibers made from a 50/50 CP-PCL blend as compared to other blends.

Chapter 7: Recommendations

Part of this study was to focus on the modelling of the optimization process to produce PCL nanofibers, as a non-conductive polymer. Future work could be to model the optimization process for a conductive polymer, using terminal jet theory, to see if the experimental and theoretical diameters follow a similar pattern.

In this study, cellulose propionate, with a degree of substitution of 2.92, was used to produce cellulose propionate-poly caprolactone (CP-PCL) blends. The effect of blend percentage on physical properties of the resulting nanofibers was investigated. Future work could be to investigate the effect of cellulose propionate with different degrees of substitution on the physical properties of the resulting CP-PCL nanofibers.

8. References:

[1] Baji A., Mai Y.-W. , Wong S.-C. , Abtahi M. ,Chen P. *Electrospinning of polymer nanofibers: Effects on oriented morphology,structures and tensile properties*. Composites Science and Technology; 70, 703–718 (2010).

[2] Subbiah T., Bhat G.S., Tock R.W., Parameswaran S., Ramkumar S. S. *Electrospinning of nanofibers*. Journal of Applied Polymer Science; 96, 557-569 (2005).

[3] Shimao M. *Biodegradation of plastics*. Current Opinion in Biotechnology; 12, 242 (2001).

[4] Jayasekara R., Harding I., Bowater I., Lonergan G. *Biodegradability of selected range of polymers and polymer blends and standard methods for assessment of biodegradation*. Journal of Polymers and the Environment; 13, 231 (2005).

[5] Dzenis Y. *Spinning continuous fibers for nanotechnology*. Science; 304, 1918 (2004).

[6] Nain A.S., Wong J.C., Amon C.H., Sitti M. *Drawing suspended polymer micro/nanofibers using glass micropipettes*. Applied Physics Letters; 89, 183105-7 (2006).

[7] Huczko A. *Template-based synthesis of nanomaterials*. Journal of Applied Physics A; 70, 365–376 (2000).

[8] Taylor G. *Electrically driven jets*. Proceedings of the National Academy of Science; A313 453-475 (1969).

[9] http://molsync.com/demo/greensolvents.php

[10] Fridrikh S.V., Yu J.H., Brenner M.P., Rutledge G.C. *Controlling the fiber diameter during electrospinning*. Physical Review Letters; 90, 144502-1 to 144502-4 (2003).

[11] Zhang, J., Lin T., Wang X. *Electrospun nanofibre toughened carbon/epoxy composites: Effects of poly etherketone cardo (PEK-C) nanofibre diameter and interlayer thickness*. Composites Science and Technology; 70, 11, 1660-1666 (2010).

[12] Barhate R.S., Ramakrishna S. *Nanofibrous filtering media: Filtration problems and solutions from tiny materials*. Journal of Membrane Science; 296, 1-8 (2007).

[13] Ramazan A., Harish M., Zeinab V., Waseem S.K., Abu A., Nurxat N. *Study of hydrophilic electrospun nanofiber membranes for filtration of micro and nanosize suspended particles*. Membranes; 3, 375-388 (2013).

[14] Avérous L., Pollet E. *Environmental silicate nano-biocomposites*. (London, Springer-Verlag, 2012).

[15] Yuris D. *Structural Nanocomposites*. Science; 319, 419–420 (2008).

[16] Erik T.T., Chunyu L., Tsu-Wei C. *Nanocomposites in context*. Composites Science and Technology; 65, 491 (2005).

[17] Coleman J.N., Khan U., Gun'ko Y.K. *Mechanical reinforcement of polymers using carbon nanotubes*. Advanced Materials; 18, 689-706 (2006).

[18] Hamed S., Tommaso B., Giangiacomo M., Anderea Z. *Improvement the impact damage resistance of composite materials by interleaving Poly caprolactone nanofibers*. Engineering Solid Mechanics; 3, 21-26 (2015).

[19] Justin O.Z., Maria S.P., Youssef H., Richard A.V., Orlando J.R. *Reinforcing poly caprolactone nanofibers with cellulose nanocrystals*. Applied Materials & Interfaces; 1, 1996-2004 (2009).

[20] Sridhar K. *Nanocomposites*. Journal of Materials Chemistry; 2, 1219-1230 (1992).

[21] Xu C., Yang F., Wang S., Ramakrishna S. *In vitro study of human vascular endothelial cell function on materials with various surface roughnesses*. Journal of Biomedical Materials Research, Part A; 71, 154-161 (2004).

[22] Rubenstein D., Han D., Goldgraben S., El-Gendi H., Gouma, P.-I. , Frame M.D. *Bioassay chamber for angiogenesis with perfused explanted arteries and electrospun scaffolding*. Microcirculation; 14, 723-737 (2007).

[23] Balguid A., Mol A., Van M.M.H., Bank R.A., Bouten C.V.C., Baaijens F.P.T. *Tailoring fiber diameter in electrospun poly (epsiln.-Caprolactone) scaffolds for optimal cellular infiltration in cardiovascular tissue engineering*. Tissue Engineering, Part A; 15, 437-444 (2009).

[24] Fang J., Niu H., Lin T., Wang X. *Applications of electrospun nanofibers*. Chinese Science Bulletin; 53, 2265-2286 (2008).

[25] Dong Y., Yong T., Liao S., Chan C.K., Stevens M.M., Ramakrishna S. *Distinctive degradation behaviors of electrospun poly glycolide, poly(L-lactide-coglycolide),and poly(L-lactide-co-ε-caprolactone) nanofibers cultured with/without porcine smooth muscle cells*. Tissue Engineering, Part A; 16, 283-298 (2010).

[26] Zhao P., Jiang H., Pan H., Zhu K., Chen W. *Biodegradable fibrous scaffolds composed of gelatin coated poly caprolactone prepared by coaxial electrospinning*. Journal of Biomedical Materials Research, Part A; 83, 372-382 (2007).

[27] Yoshimoto H., Shin Y.M., Terai H., Vacanti J.P. *A biodegradable nanofiber scaffold by electrospinning and its potential for bone tissue engineering*. Biomaterials; 24, 2077 (2003).

[28] Nelson S.B., Amrita N., Deepthy M., Bhaskaran V.K., Ullas M., Shantikumar V. N. *PCL–gelatin composite nanofibers electrospun using diluted acetic acid–ethyl acetate solvent system for stem cell-based bone tissue engineering*. Journal of Biomaterials Science, Polymer Edition; 25, 325-340 (2014).

[29] Fouad H., Elsarnagawy T., Fahad N.A., Khalil A.K. *Preparation and in vitro thermo-mechanical characterization of electrospun PLGA nanofibers for soft and hard tissue replacement*. International Journal of Electrochemical Science; 8, 2293 – 2304 (2013).

[30] Schneide A., Wang X.Y., Kaplan D.L., Garlick J.A., Egles C. *Biofunctionalized electrospun silk mats as a topical bioactive dressing for accelerated wound healing*. Acta Biomaterialia; 5, 2570-2578 (2009a).

[31] Merrell J. G., McLaughlin S. W., Tie L., Laurencin C. T., Chen A. F., Nair L.S. *Curcumin-loaded poly caprolactone nanofibres: diabetic wound dressing with anti-oxidant and anti-inflammatory properties*. Clinical and Experimental Pharmacology and Physiology; 36, 1149-1156 (2009).

[32] Jung S.M., Yoon G.H., Lee H.C., Shin H.S. *Chitosan nanoparticle/PCL nanofiber composite for wound dressing and drug delivery*. Journal of Biomaterials Science, Polymer Edition; 26, 252-263 (2015).

[33] Suwantong O., Ruktanonchai U., Supaphol P. *In vitro biological evaluation of electrospun cellulose acetate fiber mats containing asiaticoside or curcumin*. Journal of Biomedical Materials Research, Part A; 94, 1216-1225 (2010).

[34] Hyuk S.Y., Taek G.K., Tae G.P. *Surface-functionalized electrospun nanofibers for tissue engineering and drug delivery*. Advanced Drug Delivery Reviews; 61, 1033-1042 (2009).

[35] Xue, J., He M., Liu H., Niu Y., Crawford A., Coates P.D., Zhang L. *Drug loaded homogeneous electrospun PCL/gelatin hybrid nanofiber structures for anti-infective tissue regeneration membranes*. Biomaterials; 35, 9395-9405 (2014).

[36] Sridhar R., Madhaiyan K., Sundarrajan S., Góra A., Venugopal J.R., Ramakrishna S. *Cross-linking of protein scaffolds for therapeutic applications: PCL nanofibers delivering riboflavin for protein cross-linking*. Journal of Materials Chemistry; 2, 1626-1633 (2014).

[37] Karuppuswamy P., Venugopal J.R., Navaneethan B., Laiva A.L., Ramakrishna S. *Poly caprolactone nanofibers for the controlled release of tetracycline hydrochloride*. Materials Letters; 141, 180-186 (2015).

[38] He C.L., Huang Z.M., Han X.J. *Fabrication of drug-loaded electrospun aligned fibrous threads for suture applications*. Journal of Biomedical Materials Research, Part A; 89, 80-95 (2009).

[39] Cooper A., Oldinski R., Ma H., Bryers J.D., Zhang M. *Chitosan-based nanofibrous membranes for antibacterial filter applications*. Carbohydrate Polymers; 92, 254-259 (2013).

[40] Sugunan A., Guduru V.K., Uheida A., Toprak M.S., Muhammed M. *Radially oriented ZnO nanowires on flexible poly-L-lactide nanofibers for continuous-flow photocatalytic water purification*. Journal of the American Ceramic Society; 93, 3740-3744 (2010).

[41] Yu J., Liu T. *Preparation of nano-fiber supported palladium catalysts and their use for the catalytic hydrogenation of olefins*. Acta Polymerica Sinica; 6, 514-518 (2007).

[42] Deng C., Gong P., He Q., Cheng J., He C., Shi L., Zhu D., Lin T. *Highly fluorescent TPA-PBPV nanofibers with amplified sensory response to TNT*. Chemical Physics Letters; 483, 219-223 (2009).

[43] Yoon J., Chae S.K., Kim J.M. *Colorimetric sensors for volatile organic compounds (VOCs) based on conjugated polymer-embedded electrospun fibers*. Journal of the American Chemical Society; 129, 3038-3039 (2007).

[44] Wu H., Hu L., Rowell M.W., Kong D., Cha J.J., McDonough J.R., Zhu J., Yang Y., McGehee M.D., Cui Y. *Electrospun metal nanofiber webs as highperformance transparent electrode*. Nano Letters; 10, 4242-4248 (2010a).

[45] Liu Z.H., Pana C.T., Lin L.W., Lai H.W. *Piezoelectric properties of PVDF/MWCNT nanofiber using near-field electrospinning*. Sensors and Actuators A; 193, 13- 24 (2013).

[46] Joshi P., Zhang L., Chen Q., Galipeau D., Fong H., Qiao Q. *Electrospun carbon nanofibers as low-cost counter electrode for dye-sensitized solar cells*. ACS Applied Materials & Interfaces; 2, 3572-3577 (2010).

[47] Tucker N., Stanger J.J., Staiger M.P., Razzaq H., Hofman K. *The history of the science and technology of electrospinning from 1600 to 1995*. Journal of Engineered Fibers and Fabrics; 7, 63-73 (2012).

[48] Salem D.R. *Structure formation in polymeric fibers* (Cincinnati, Ohio: Hanser Publishing; 225-46, 2001).

[49] Reneker D.H., Yarin A.L. *Electrospinning jet and polymer nanofiber*. Polymer; 49, 2387-2425 (2008).

[50] Olubayode E.-P., Mike J., Artemis S. *Tailoring crystallinity of electrospun PLLA Fibers by Control of electrospinning parameters*. Polymers; 4, 1331-1348 (2012).

[51] Wadgymar G.J.A., Rodríguez G.C.A., Elías Z.A., Ortega L.W.L., Siller C.H. R., Da Silva B.P.J. *Effect of selected process and solution parameters in electrospun microfibers*. Memorias del XVII Congreso Internacional Anual de la Somim 21 al 23 de septiembre, 2011 San Luis, Potosí, México.

[52] Valencia J., Rajesh D.A., Malik M., *The influence of electrospinning parameters on the structural morphology and diameter of electrospun nanofibers*. Journal of Applied Polymer Science; 115, 3130–3136 (2010).

[53] Zong X.H., Kim K., Fang D.F., Ran S.F., Hsiao B.S., Chu B. *Structure and process relationship of electrospun bioabsorbable nanofiber membranes.* Polymer; 43, 4403 (2002).

[54] Gupta P., Elkins C., Long T.E., Wilkes G.L. *Electrospinning of linear homo polymers of poly (methyl methacrylate): exploring relationships between fiber formation, viscosity, molecular weight and concentration in a good solvent*. Polymer; 46, 4799 (2005).

[55] Deitzel J.M., Kleinmeyer J., Harris D., Tan N.C.B. *The effect of processing variables on the morphology of electrospun nanofibers and textiles*. Polymer; 42, 261-72 (2001).

[56] Marwa A.O., Ahmed I.W., Ahmed I.E., Ebtesam A.S., Bothaina M.A.E. *Electrospun gelatin nanofibers: effect of gelatin concentration on morphology and fiber diameters*. Journal of Applied Sciences Research; 9, 534-540 (2013).

[57] Matabola K.P., Moutloali R.M. *The influence of electrospinning parameters on the morphology and diameter of poly(vinyledene fluoride) nanofibers- effect of sodium chloride*. Journal of Materials Science; 48, 5475-5482 (2013).

[58] Zhang C.X., Yuan X.Y., Wu L.L., Han Y., Sheng J. *Study on morphology of electrospun poly(vinyl alcohol) mats*. European Polymer Journal; 41, 423-432 (2005).

[59] Zuo W.W., Zhu M.F., Yang W., Yu H., Chen Y.M., Zhang Y. *Experimental study on relationship between jet instability and formation of beaded fibers during electrospinning*. Polymer Engineering & Science; 45, 704 (2005).

[60] Jiang H., Fang D., Hsiao B.S., Chu B., Chen W. *Optimization and characterization of dextran membranes prepared by electrospinning*. Biomacromolecules; 5, 326–333 (2004).

[61] Fong H., Chun I., Reneker D.H. *Beaded nanofibers formed during electrospinning.* Polymer; 40, 4585 (1999).

[62] Zhang C.X., Yuan X.Y., Wu L.L., Han Y., Sheng J. *Study on morphology of electrospun poly(vinyl alcohol) mats*. European Polymer Journal; 41, 423, (2005).

[63] Demir M.M., Yilgor I., Yilgor E., Erman B. *Electrospinning of polyurethane fibers*. Polymer; 43, 3303 (2002).

[64] Meechaisue C., Dubin R., Supaphol P., Hoven V.P., Kohn J. *Electrospun mat of tyrosine-derived polycarbonate fibers for potential use as tissue scaffolding material*. Journal of Biomaterials Science, Polymer Edition; 17, 1039-56 (2006).

[65] Travis J.S., Horst A.R. *Electrospinning: Applications in drug delivery and tissue engineering*. Biomaterials; 29, 1989-2006 (2008).

[66] Pham Q.P., Sharma U., Mikos A.G. *Electrospinning of polymeric nanofibers for tissue engineering applications: A review*. Tissue Engineering; 12, 1197-1211 (2006).

[67] Megelski S., Stephens J.S., Chase D.B., Rabolt J.F. *Micro- and nanostructured surface morphology on electrospun polymer fibers*. Macromolecules; 35, 8456-8466 (2002).

[68] Jaeger R., Bergshoef M.M., Batlle C.M.I., Schonherr H., Vancso G.J. *Electrospinning of ultra-thin polymer fibers*. Macromolecular Symposia; 127, 141-150 (1998).

[69] Chang S.K., Doo H.B., Kyung D.G., Ki H.L., In C.U., Young H.P. *Characterization of gelatin nanofiber prepared from gelatin-formic acid solution*. Polymer; 46, 5094 (2005).

[70] Geng X.Y., Kwon O.H., Jang J.H. *Electrospinning of chitosan dissolved in concentrated acetic acid solution*. Biomaterials; 26, 5427 (2005).

[71] Mo X.M., Xu C.Y., Kotaki M., Ramakrishna S. *Electrospun P(LLA-CL) nanofiber:a biomimetic extracellular matrix for smooth muscle cell and endothelial cell proliferation*. Biomaterials; 25, 1883-1890 (2004).

[72] Keng-Liang O., Chin-Sung C., Li-Hsiang L., Jen-Chieh L., Yao-Chi S., Wen-Chin T., Jen-Chang Y., Sheng-Yang L., Chien-Chung C. *Membranes of epitaxial-like packed, super aligned electrospun micron hollow poly(l-lactic acid) (PLLA) fibers*. European Polymer Journal; 47, 882–892 (2011).

[73] Theron S.A., Yarin A.L., Zussman E., Kroll E. *Multiple jets in electrospinning: Experiment and modeling*. Polymer; 46, 2889 (2005).

[74] Ding B., Kimura E., Sato T., Fujita S., Shiratori S. *Fabrication of blend biodegradable nanofibrous nonwoven mats via multi-jet electrospinning*. Polymer; 45, 1895 (2004).

[75] Zussman E., Theron A., Yarin A.L. *Formation of nanofiber crossbars in electrospinning*. Applied Physics Letters; 82, 973 (2003).

[76] Li D., Xia Y. *Electrospinning of nanofibers: Reinventing the wheel?* Advanced Materials; 16, 1151-1170 (2004).

[77] Thomas V., Jose M.V., Chowdhury S., Sullivan J.F., Dean D.R., Vohra Y.K. *Mechano-morphological studies of aligned nanofibrous scaffolds of poly caprolactone fabricated by electrospinning*. Journal of Biomaterials Science, Polymer Edition; 17, 969-84 (2006).

[78] Baji A., Mai Y.W, Wong S.C., Abtahi M., Che P. *Electrospinning of polymer nanofibers: Effects on oriented morphology, structures and tensile properties*. Composites Science and Technology; 70, 703–718 (2010).

[79] Nandana B., Subhas C.K. *Electrospinning: A fascinating fiber fabrication technique*. Biotechnology Advances; 28, 325–347 (2010).

[80] Mit-Uppatham C., Nithitanakul M., Supaphol P. *Ultrafine electrospun polyamide-6 fibers: effect of solution conditions on morphology and average fiber diameter*. Macromolecular Chemistry and Physics; 205, 2327 (2004).

[81] Casper C.L., Stephens J.S., Tassi N.G., Chase D.B., Rabolt J.F. *Controlling surface morphology of electrospun polystyrene fibers: effect of humidity and molecular weight in the electrospinning process*. Macromolecules; 37, 573 (2004).

[82] Yarin A.L., Koombhongse S., Reneker D.H. *Taylor cone and jetting from liquid droplets in electrospinning of nanofibers*. Journal of Applied Physics; 90, 4836 (2001).

[83] Hohman M.M., Shin M., Rutledge G.C., Brenner M.P. *Electrospinning and electrically forced jet. I. Stability theory*. Physics of Fluids; 13, 2201 (2001).

[84] Thompson C.J., Chase G.G., Yarin A.L., Reneker D.H. *Effects of parameters on nanofiber diameter determined from electrospinning model*. Polymer; 48, 6913-6922 (2007).

[85] Samatham R., Kim K.J. *Electric current as a control variable in the electrospinning process*. Polymer Engineering & Science; 46, 954-959 (2006).

[86] Cengiz-Callıoglu F., Jirsak O., Dayık M. *Electric current in polymer solution jet and spinnability in the needleless electrospinning process*. Fiber Polymer; 13, 1266-1271 (2012).

[87] Bhattacharjee P.K., Schneider T.M., Brenner M.P., McKinley G.H., Rutledge G.C. *On the measured current in electrospinning*. Journal of Applied Physics; 107, 044306-1 to 044306-7 (2010).

[88] Fallahi D., Rafizadeh M., Mohammadi N., Vahidi B. *Effect of applied voltage on surface and volume charge density of the jet in electrospinning of polyacrylonitrile solutions*. Polymer Engineering & Science; 50, 1372–1376 (2010).

[89] Leo C.J., Nangrejo M., Edirisinghe M. *A novel method of selecting solvents for polymer electrospinning*. Polymer; 51, 1654-1662 (2010).

[90] Leo C.J.E., Stride M., Edirisinghe M. *Mapping the influence of solubility and dielectric constant on electrospinning poly caprolactone solutions*. Macromolecules; 45, 4669-4680 (2012).

[91] http://www.brookfieldengineering.com/education/what-is-viscosity.asp

[92] Höhne G.W.H., Hemminger W.F., Flammersheim H.-J. *Differential scanning calorimetry*, (New York, Springer- Verlag, 2003).

[93] Rao M.B., Rao C.R. *Handbook of statistics: Computational statistics* (Netherland, Elsevier Science, 2014).

[94] Liebert T., Hussain M.A., Heinze T. *Structure Determination of Cellulose Ester via Subsequent Functionalization and NMR Spectroscopy*. Macromolecular Symposia; 223, 79-91 (2005).

[95] Barton A.F.M. *Handbook of solubility parameters and other cohesion parameters* (Boca Raton, Florida: CRC Press Inc.; 1983).

[96] Baturalp Y., Fatma Y., Oldrich J., Funda C.-C. *On the nature of electric current in the electrospinning process.* Journal of Nanomaterials; 7, 4672-9 (2013).

[97] Wunderlich B. *Crystal melting*. Macromolecular Physics; 3, 54 (1980).

[98] Cui W.G., Li X.H., Zhu X.L., Yu G., Zhou S.B., Weng J. *Investigation of drug release and matrix degradation of electrospun poly(D,L-lactide) fibers with paracetanol inoculation*. Biomacromolecules; 7, 1623–1629 (2006).

[99] Zong X.H., Kim K., Fang D.F., Ran S.F., Hsiao B.S., Chu B. *Structure and process relationship of electrospun bioabsorbable nanofiber membranes*. Polymer; 43, 4403–4412 (2002).

[100] Yoshiyuki N., Kensuke M., Yoshiharu M., Noritaka K., Hidematsu S. *Blends of poly (∈-caprolactone) with cellulose alkyl esters: effect of the alkyl side-chain length and degree of substitu tion on miscibility.* Cellulose; 4, 131-145 (1997).

Appendix A. Hansen fractional parameters for pure solvents

Table A1: The fractional parameters, f_d, f_p and f_h for pure solvents.

Solvent	f_d	f_p	f_h	$100f_d$	$100f_p$	$100f_h$
Acetone	0.47	0.32	0.21	47	32	21
$CHCl_3$	0.67	0.12	0.21	67	12	21
CH_2Cl_2	0.59	0.21	0.20	59	21	20
DMF	0.41	0.32	0.27	41	32	27
MeOH	0.30	0.25	0.45	30	25	45
THF	0.55	0.19	0.26	55	19	26
Ethyl Acetate	0.56	0.19	0.25	56	19	25
1,4-Dioxane	0.67	0.06	0.26	67	7	26

Appendix B. Hansen fractional parameters for binary solvents

Table B1: Example of fractional parameter calculation for a blend:

Solvents	Ratio	$100f_d$	$100f_p$	$100f_h$
MeOH	1	30*1/4=7.5	25*1/4=6.25	45*1/4=11.25
$CHCl_3$	1	67*3/4=50.25	12*3/4=9	21*3/4=15.75
$CHCl_3$:MeOH	3:1	7.5+50.25=57.8	6.25+9=15.12	11.25+15.75=27

Table B2: The fractional parameters, f_d , f_p and f_h for mixed solvents.

Solvents	Ratio	$100f_d$	$100f_p$	$100f_h$
$CHCl_3$:MeOH	3:1	57.8	15.2	27
CH_2Cl_2:MeOH	3:1	51.8	22	26.2
$CHCl_3$:DMF	3:1	60.5	17	22.5
CH_2Cl_2:DMF	3:1	54.5	23.75	21.75
THF:MeOH	3:1	48.75	20.5	30.75
THF:DMF	3:1	51.5	22.25	26.25
EA:MeOH	3:1	49.5	20.5	30
EA:DMF	3:1	52.25	22.25	25.5
DIOX:MeOH	3:1	57.75	11.5	30.75
DIOX:DMF	3:1	60.5	13.25	26.25
THF:MeOH	1:1	42.5	22	35.5
THF:MeOH	2:1	46.7	21	32.3
THF:MeOH	4:1	50	20.2	29.8
THF:MeOH	5:1	50.8	20	29.2

Appendix C. Electrospinning results for the optimization of the solvent ratio

Table C1: Electrospinning results for the optimization of the solvent ratio.

Solvent System	ε	Surface Tension Dyne/cm	Fiber average Diameter (nm)	STD	Observation	P-Value for samples in same conditions	P-Value For different solvent
THF:MeOH (1:1)	22.1	28.2	****	****	PCL did not dissolve completely	*****	< 0.0001
THF:MeOH (2:1)	17.9	29.2	745	333	Fiber (Dissolution of PCL is temp dependent)	0.242	
THF:MeOH (3:1)	15.8	29.6	774	387	Fiber	0.495	
THF:MeOH (4:1)	14.5	29.9	937	413	Fiber	0.748	
THF:MeOH (5:1)	13.7	30.2	1237	486	Fiber	0.179	

Appendix D. Tukey test results for the optimization of electrospinning parameters

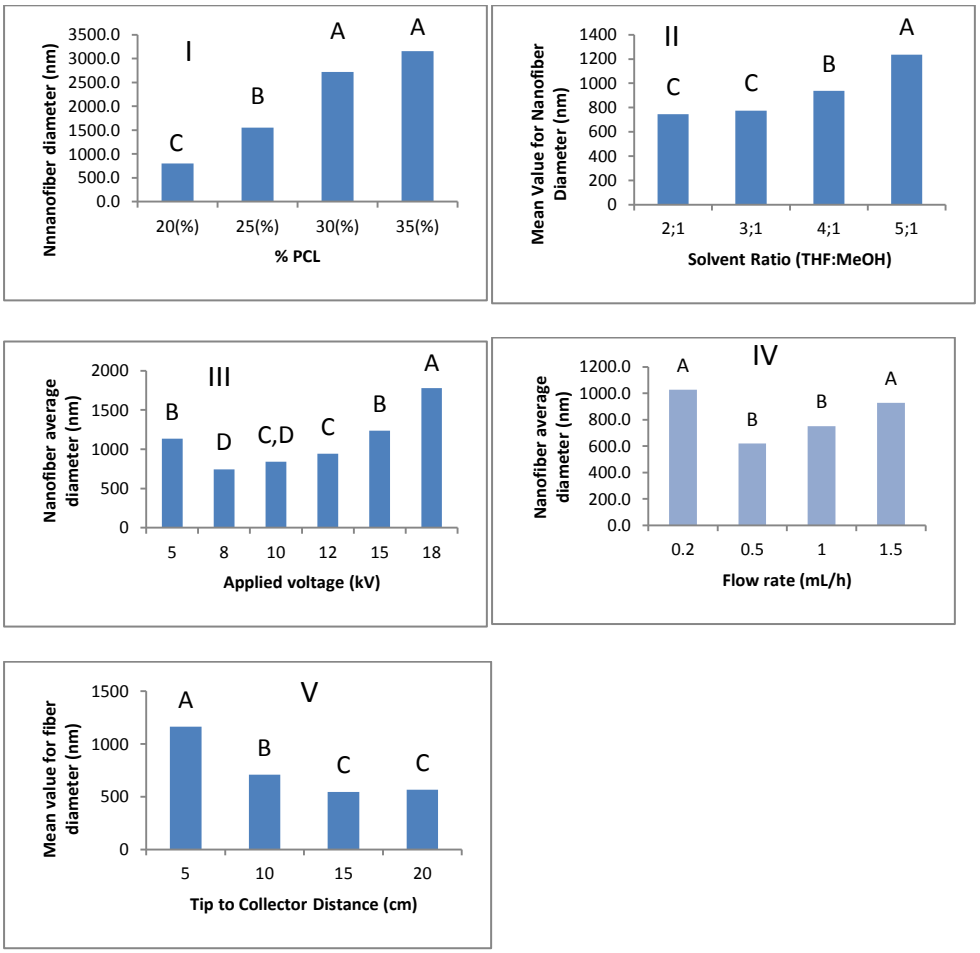

Figure D1: The result of the Tukey test for different concentrations (PCL concentration, solvent system, electric field strength, flow rates, and TCD)

Appendix E. Electrospinning results for the optimization of PCL concentration

Table E1: Results for PCL concentration optimization.

% PCL	Viscosity of PCL Solution (CP)	Average Fiber Diameter (nm)	Standard Deviation	Observation	P-Value for samples in sames conditions	P-Value For different % PCL
5	9	*****	*****	Bead with small amount of Fiber	*****	*****
8	22	*****	*****	Bead with small amount of Fiber	*****	
12	73	*****	*****	Bead and Fiber	*****	
15	165	*****	*****	Bead and Fiber	*****	
18	310	*****	*****	Fiber with small amount of bead	*****	
20	428	800	399	Fiber	0.964	< 0.0001
25	1118	1550	659	Fiber	0.270	
30	3327	2720	971	Fiber	0.371	
35	4607	3155	1240	Un uniform Fiber	2.21E-06	

Appendix F. Electrical connection scheme for electrospinning setup

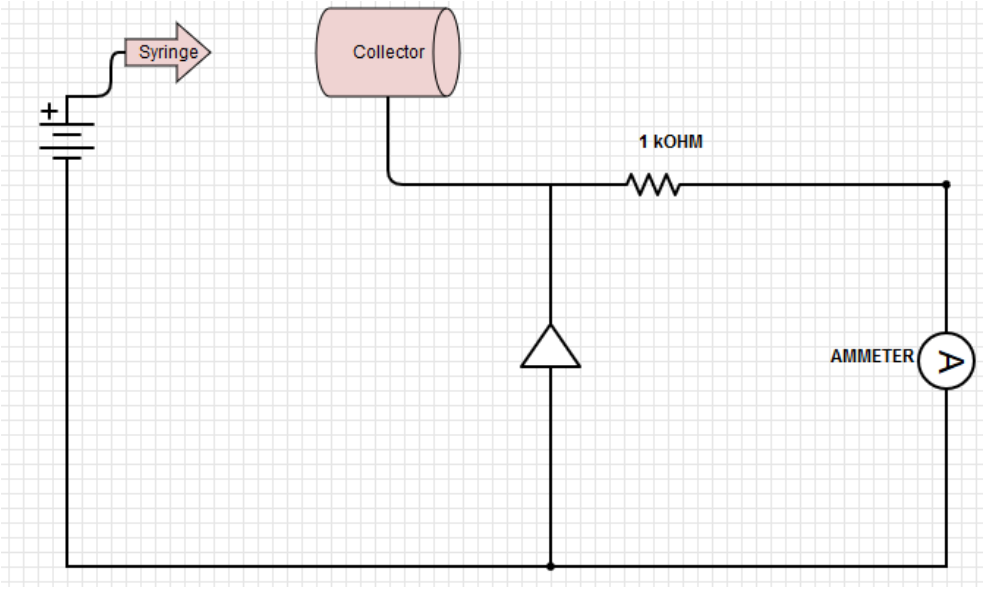

Figure F1: Schematic illustration of electrospinning and carried electric current measurement.

Appendix G. Results for whipping current and calculated χ of PCL concentration

Table G1: Measured collecting spot diameter in different polymer concentration.

% PCL	Collecting spot diameter (μm)			D-Ave	STD
20	83000	80000	78000	80333	2517
22	59000	55000	56000	56667	2082
25	38000	44000	43000	41667	3215

Table G2: Measured electric current for whipping motion during electrospinning for different polymer concentrations.

PCL Concentration (%)	I_1 (nA)	I_2 (nA)	I_3 (nA)	AVE-I (nA)	STD
20	44	36	37	39	4
22	62	62	60	61	1
25	64	62	66	64	2

Table G3: Experimental results of χ for different polymer concentrations resulting from jet length and diameter.

% PCL	**h (μm)**			**h-Ave (μm)**	**L (μm)**			**L-Ave (μm)**	**χ (Ave)**	**χ-STD**
	1	**2**	**3**		**1**	**2**	**3**			
20	77	102	67	82	13317	14376	15414	14369	160	35
22	121	100	113	111	18625	15387	12790	15601		
25	97	125	105	109	18245	15881	16737	16954		

Appendix H. Results for the modeling of PCL concentration optimization

Table H1: Experimental and theoretical fiber diameter depending on polymer concentration.

v kV	Q_c cm^3/s	γ g/s^2	I (SI) nA	I cgs $cm^{3/2}\cdot g^{1/2}\cdot s^{-2}$	χ	2Lnχ-3	Theoretical Fiber diameter (nm)	Experimental Fiber diameter (nm)
20	0.000056	29.6	39	118	160	7	844	800
22	0.000061	29.6	61	184	160	7	667	1550
25	0.000069	29.6	64	192	160	7	706	2720

Appendix I. Electrospinning results for the optimization of applied voltage

Table I1: Electrospinning results for optimization of applied voltage.

Applied Voltage (kV)	AVE Fiber Diameter	STD	Observation	α-Value	P-Value for samples in same conditions	P-Value For different voltage
5	1135	454	Fiber	0.05	0.218	< 0.0001
8	743	408	Fiber	0.05	0.947	
10	841	420	Fiber	0.05	0.917	
12	945	355	Fiber	0.05	0.387	
15	1236	432	Fiber	0.05	0.853	
18	1778	839	Fiber	0.05	0.118	

Appendix J. Electric current graphs for different applied voltage

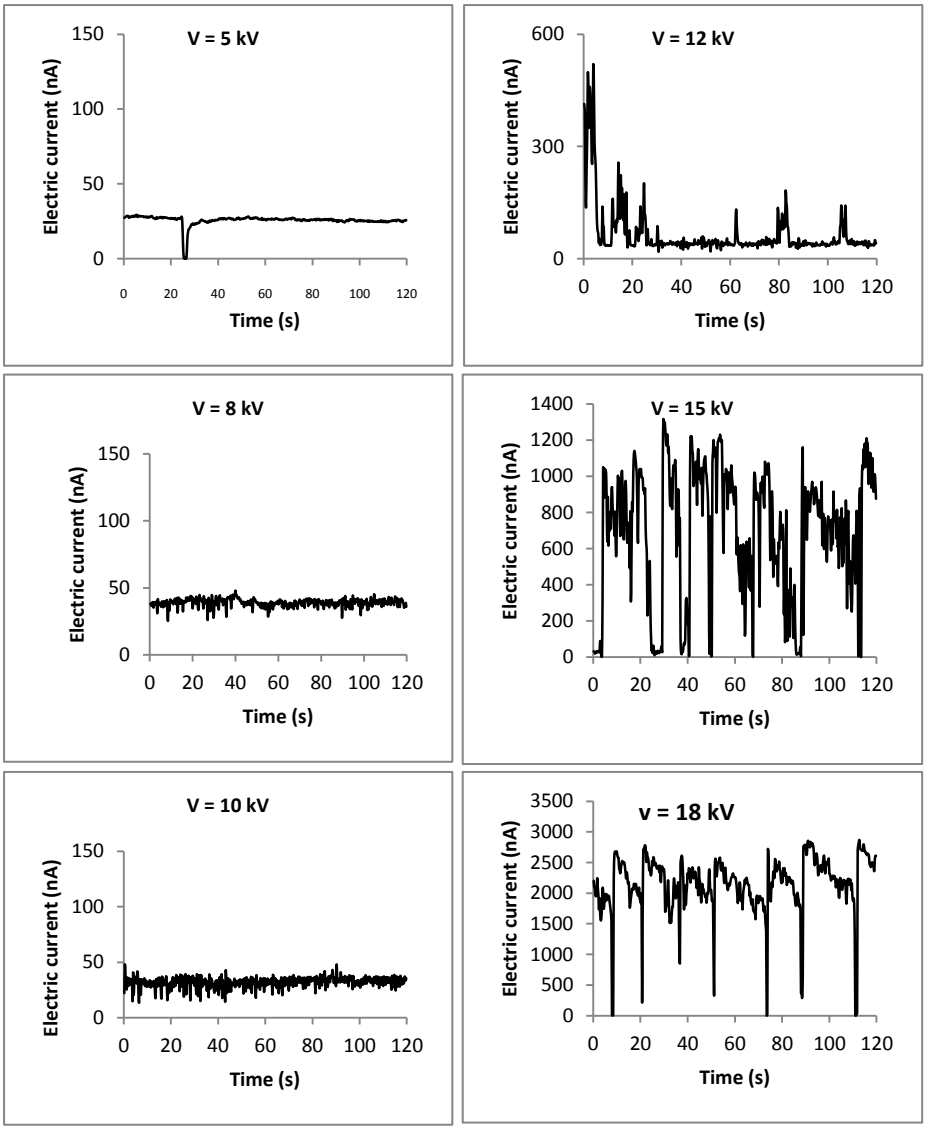

Figure J1: Electric current vs time graph for different applied voltage.

Appendix K. Results for whipping current and calculated χ for applied voltage

Table K1: Experimental data for whipping current during electrospinning at different voltages.

Voltage (kV)	I_1 (nA)	I_2 (nA)	I_3 (nA)	AVE Current(nA)	STD
5	21	26	26	24	3
8	32	34	39	35	4
10	44	36	37	39	4
12	33	48	38	40	8
15	43	38	33	38	5
18	22	32	51	35	15

Table K2: Experimental results of χ for different applied voltage resulting from jet length and diameter

Applied voltage (kV)	h (μm)			Ave-h	L (μm)			Ave-L	Ave-χ	χ Std
	1	**2**	**3**		**1**	**2**	**3**			
5	45	43	37	42	5053	5671	4989	5238	150	35
8	76	59	63	66	9562	9112	11485	10053		
10	77	102	67	82	13317	14376	15414	14369		
12	131	122	99	117	19523	19181	20128	19611		
15	126	97	144	122	23349	21226	26810	23795		
18	219	157	109	162	22700	24517	18455	21891		

Appendix L. Results for modeling of applied voltage optimization

Table L1: Experimental and theoretical fiber diameter depending on applied voltage.

v kV	Q_c cm^3/s	ɤ g/s^2	I(SI) nA	I (cgs) $cm^{3/2}\cdot g^{1/2}\cdot s^{-2}$	χ	2Lnχ-3	Theoretical Fiber diameter (nm)	Experimental Fiber diameter (nm)
5	0.000056	29.6	24	73	150	7.02	1164	1135
8	0.000056	29.6	35	105	150	7.02	911	743
10	0.000056	29.6	39	118	150	7.02	844	841
12	0.000056	29.6	40	120	150	7.02	833	945
15	0.000056	29.6	38	114	150	7.02	862	1236
18	0.000056	29.6	35	105	150	7.02	911	1778

Appendix M. Electrospinning results and electric current graphs for different flow rates

Table M1: Electrospinning results for flow rate optimization.

Flow Rate mL/h	AVE Fiber Diameter	STD	Observation	α-Value	P-Value for samples in same conditions	P-Value for different Flow rate
0.2	1028	599	Fiber	0.05	0.933	< 0.0001
0.5	621	342	Fiber	0.05	0.532	
1	751	388	Fiber	0.05	0.989	
1.5	927	471	Fiber	0.05	0.351	

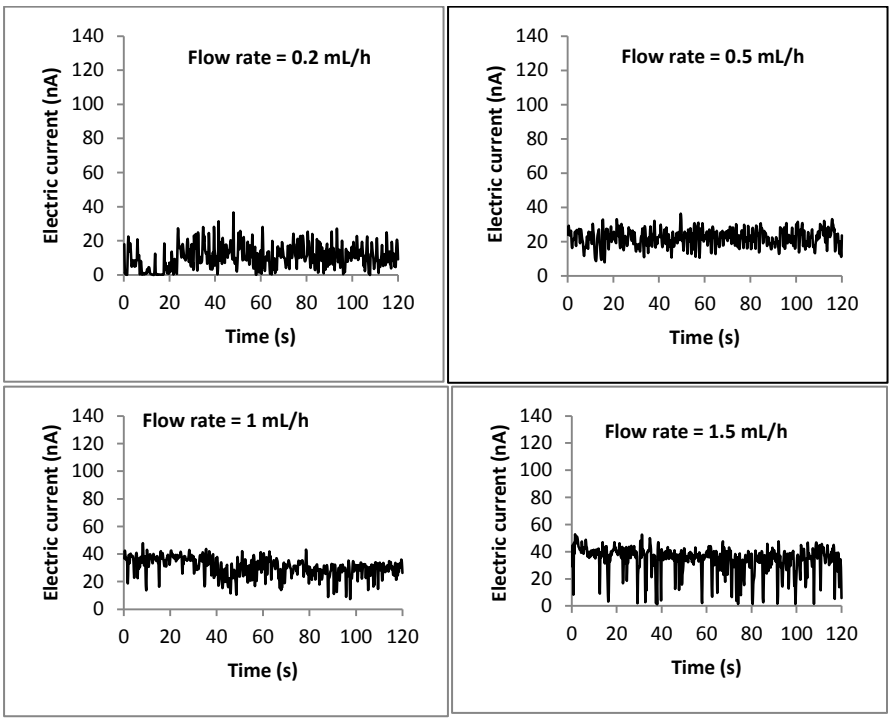

Figure M1: Electric current vs time graph for different flow rate.

Appendix N. Results for whipping current and calculated χ for flow rate

Table N1: Measured electric current during electrospinning for different flow rates.

Flow rate (mL/h)	I_1 (nA)	I_2 (nA)	I_3 (nA)	AVE Current(nA)	STD
0.2	12	12	11	12	1
0.5	22	24	22	23	1
1	27	34	32	31	3
1.5	36	35	34	35	1

Table N2: Experimental results of χ for different flow rates resulting from jet length and diameter.

Flow Rate mL/h	h (μm)			h-Ave (μm)	L (μm)			L-Ave (μm)	χ-Ave	χ-STD
	1	2	3		1	2	3			
0.2	94	97	84	92	13699	10297	11669	11888	125	29
0.5	50	58	71	60	7438	7075	7094	7202		
1	76	59	63	66	9562	9112	11485	10053		
1.5	79	83	93	85	7328	7596	8964	7963		

Table N3: Experimental and theoretical fiber diameter depending on flow rate.

Flow rate mL/h	Q_C cm^3/s	ɤ g/s^2	I (SI) nA	I (cgs) $cm^{3/2}\cdot g^{1/2}\cdot s^{-2}$	χ	2Lnχ-3	Theoretical Fiber diameter (nm)	Experimental Fiber diameter (nm)
0.2	$1.11*10^{-5}$	29.6	12	35	125	6.65	657	1028
0.5	$2.77*10^{-5}$	29.6	23	68	125	6.65	783	621
1	$5.55*10^{-5}$	29.6	31	93	125	6.65	1006	751
1.5	$8.33*10^{-5}$	29.6	35	105	125	6.65	1217	927

Appendix O. Electrospinning results and electric current graphs for different TCD.

Table O1: Electrospinning results for the optimization of tip to collector distance.

Tip to Collector Distance (cm)	AVE Fiber Diameter	STD	Observation	α-Value	P-Value for samples in same conditions	P-Value for different TCD
5	1162	535	Fiber	0.05	0.225	< 0.0001
10	707	299	Fiber	0.05	0.305	
15	546	173	Fiber	0.05	0.423	
20	567	285	Fiber	0.05	0.908	

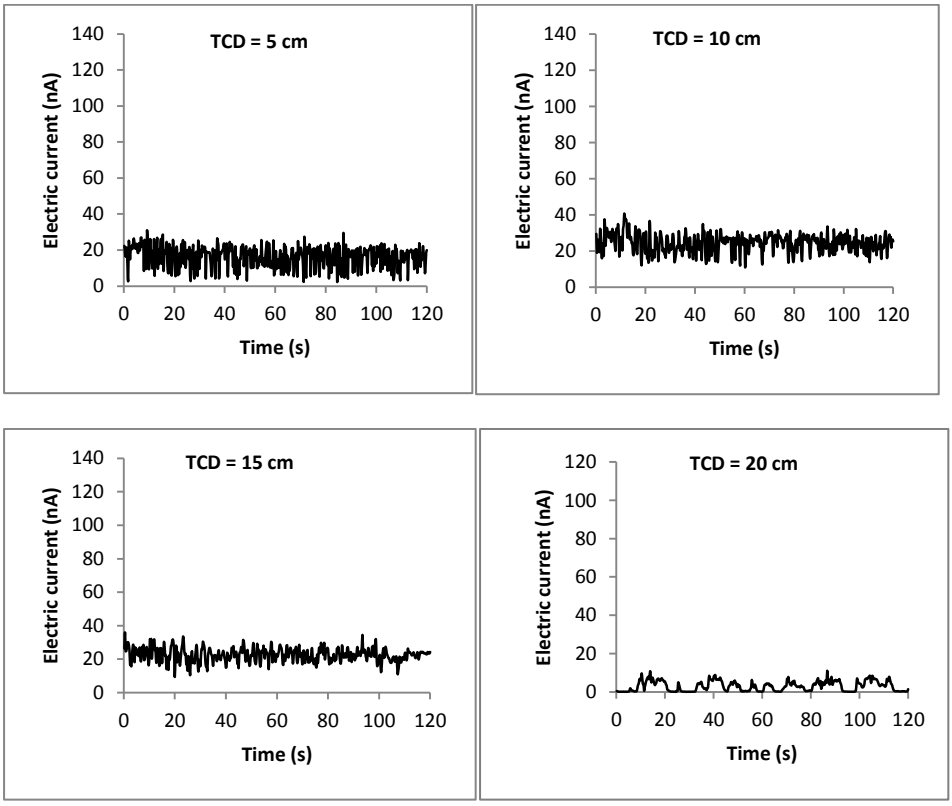

Figure O1: Electric current vs time graph for different TCDs.

Appendix P. Results for whipping current and calculated χ for different TCD

Table P1: Measured electric current during electrospinning for different TCDs

TCD cm	I_1 (nA)	I_2 (nA)	I_3 (nA)	AVE-I (nA)	STD
5	16	17	14	16	2
10	22	24	22	23	1
15	23	19	21	21	2
20	6	12	6	8	3

Table P2: Experimental results of χ for different TCD resulting from jet length and diameter.

TCD cm	h (µm)			h-Ave (µm)	L (µm)			L-Ave	χ-Ave	χ-STD
	h_1 (µm)	h_2 (µm)	h_3 (µm)		L_1 (µm)	L_2 (µm)	L_3 (µm)			
5	114	100	73	96	17429	16288	14839	16185	130	40
10	50	58	71	60	7438	7075	7094	7202		
15	63	57	85	68	6015	5835	5610	5820		

Table P3: Experimental and theoretical fiber diameter depending on TCD.

TCD cm	Q_c cm^3/s	ɤ g/s^2	I (SI) nA	I (cgs) $cm^{3/2}\cdot g^{1/2}\cdot s^{-2}$	χ	2Lnχ-3	Theoretical Fiber diameter (nm)	Experimental Fiber diameter (nm)
5	$2.8*10^{-05}$	29.6	16	47	130	6.7	993	1162
10	$2.8*10^{-05}$	29.6	23	68	130	6.7	777	707
15	$2.8*10^{-05}$	29.6	21	63	130	6.7	817	546
20	$2.8*10^{-05}$	29.6	12	36	130	6.7	1187	567

Appendix Q. Electrospinning results for the optimization of applied voltage for CP-PCL (50/50) blend

Table Q1: Results for diameter for different voltage of CP-PCL (50/50) blend.

Applied Voltage (kV)	AVE Fiber Diameter	STD	Observation	α-Value	P-Value for samples in same conditions
5	1510	485	Fiber	0.05	0.37
8	589	181	Fiber	0.05	0.89
10	820	310	Fiber	0.05	0.61
12	940	328	Fiber	0.05	0.092
15	1667	568	Fiber	0.05	0.49

Appendix R. Electrospinning results for the optimization of flow rate for CP-PCL (50/50) blend

Table R1: Fiber diameter for different flow rates of CP-PCL (50/50) blends solution.

Flow Rate mL/h	AVE Fiber Diameter	STD	Observation	α-Value	P-Value for samples in same conditions
0.2	652	170	Fiber	0.05	0.71
0.5	586	182	Fiber	0.05	0.97
1	794	302	Fiber	0.05	0.73
1.5	868	487	Fiber	0.05	0.89

Appendix S. Electrospinning results for the optimization of TCD for CP-PCL (50/50) blend

Table S1: Fiber diameter for different TCDs of CP-PCL (50/50) blends.

Tip to Collector Distance (cm)	AVE Fiber Diameter	STD	Observation	α-Value	P-Value for samples in same conditions
5	915	354	Fiber	0.05	0.58
10	665	215	Fiber	0.05	0.84
12	589	219	Fiber	0.05	0.94
15	551	197	Fiber	0.05	0.09
20	620	227	Fiber	0.05	0.01

Appendix T. Thermal properties of resultant nanofibers

Table T1: Thermal properties of resulting nanofibers of PCL and CP-PCL blends.

Sample	Repitation	Tm(° C)(PCL)	Tm(° C)(CP)	Tc(°C)(PCL)	Tc(°C) (CP)	ΔHm(PCL) J/g	ΔHm(CP) J/g	ΔHc(PCL) J/g	ΔHc(CP) J/g	C%(PCL)	C%(PCL)ave
	1	58.21	-	24.84	-	54.53	-	61.51	-	0.384014	
PCL(bulk)	2	57.94	-	26.73	-	60.49	-	52.22	-	0.425986	0.41
	1	59	-	29.97	-	75.04	-	56.69	-	0.528451	
	2	60.93	-	29.93	-	70.57	-	56.75	-	0.496972	
PCL(fiber)	3	60.05	-	29.9	-	74.58	-	57.49	-	0.525211	0.52
	1	59.85	-	16.37	-	57.77	-	42.73	-	0.51	
	2	60.38	-	17.74	-	57.59	-	41.46	-	0.51	
CP-PCL(20/80)	3	60.3	-	14.87	-	59.57		40.06	-	0.52	0.51
	1	58.14	177.43	-	-	45.73	1.433	-	-	0.54	
	2	57.95	176.84	-	-	41.58	1.796	-		0.49	
CP-PCL(40/60)	3	58.21	177.15	-	-	41.08	1.801	-	-	0.48	0.50
	1	55.75	178	-	-	28.85	4.17	-	-	0.41	
	2	55.56	177.87	-	-	28.82	4.64	-	-	0.41	
CP-PCL(50/50)	3	55.64	178.51	-	-	28.05	4.55	-	-	0.40	0.40
	1	56.25	179.35	-	121.58	7.949	5.42	-	0.8988	0.14	
	2	56.11	180.21	-	121.73	7.632	5.32	-	0.9578	0.13	
CP-PCL(60/40)	3	55.77	180.22	-	123.39	8.228	5.79		1.084	0.14	0.14
	1	55.09	181.83	-	125.1	5.88	6.54	-	1.04	0.14	
	2	54.81	181.3	-	129.3	5.70	5.69	-	1.897	0.13	
CP-PCL(70/30)	3	55.66	181.4	-	128.87	5.96	5.56	-	1.798	0.14	0.14

Appendix U. DMA results

Table U1: Summary of DMA test results.

CP%	Strain	SD	Stress	SD	V_f	SD	porosity	thickness
0	33.00474	9.306055	6.58276	1.34009	0.209091	0.006971	0.790909	0.022
20	26.31127	9.202394	7.713853	0.986619	0.224083	0.040792	0.775917	0.032
40	5.574149	1.986146	11.20233	2.056082	0.238164	0.00232	0.761836	0.033
50	8.841167	1.146261	19.32907	4.637897	0.197547	0.004712	0.802453	0.025
60	11.86216	4.206995	19.74288	2.548979	0.212552	0.009348	0.787448	0.027
70	9.564982	1.037946	16.9844	1.197088	0.256993	0.028351	0.743007	0.021